CONCURRENTLY COUPLED PERIDYNAMICS/FINITE ELEMENT SIMULATION BASED ON NONLOCAL MATCHING BOUNDARY CONDITIONS

by

Clint Nicely

APPROVED BY SUPERVISORY COMMITTEE:

Dong Qian, Chair

Hongbing Lu

Majid Minary-Jolandan

Ill Ryu

Zachary Zutavern

Copyright 2018
Clint Nicely
All Rights Reserved

CONCURRENTLY COUPLED PERIDYNAMICS/FINITE ELEMENT SIMULATION BASED ON NONLOCAL MATCHING BOUNDARY CONDITIONS

by

CLINT NICELY, BA, MS

DISSERTATION

Presented to the Faculty of

The University of Texas at Dallas

In Partial Fulfillment

of the Requirements

for the Degree of

DOCTOR OF PHILOSOPHY IN

MECHANICAL ENGINEERING

THE UNIVERSITY OF TEXAS AT DALLAS

August 2018

ACKNOWLEDGEMENTS

I would like to acknowledge the generous support of this research from Raytheon Space and Airborne Systems under their Advanced Study Program as well as The University of Texas at Dallas.

I also would like to thank my colleagues in research, Shogo Wada, Tingge Xu, Mohammad Karim Rezaul, Rui Zhang, Yang Wang, and Xuemin Wang, and my advisor Dr. Dong Qian, all of whose experience and knowledge helped steer my research—thank you for your thoughtful guidance and assistance. A special thank belongs to Dr. Terry Baughn for inviting me onto this journey of learning at UTD. A final editing of this manuscript was performed by Michael Gould which has allowed for my research to be presented with greater clarity and is appreciated greatly.

Also, I would like to extend an exceptional appreciation for my wife and family for supporting and encouraging my continued education.

April 2018

CONCURRENTLY COUPLED PERIDYNAMICS/FINITE ELEMENT SIMULATION BASED ON NONLOCAL MATCHING BOUNDARY CONDITIONS

Clint Nicely, PhD
The University of Texas at Dallas, 2018

Supervising Professor: Dong Qian

A concurrent multiscale approach that integrates non-ordinary peridynamics (NOPD) with finite element method (FEM) has been established. The proposed approach features two main technical ingredients: Firstly, a Non-Local Matching Boundary Condition (NMBC) is developed for treating the numerical interface of NOPD/FEM. The NMBC is cast in the form of a parameterized expression that involves the displacements and their higher-order time derivatives of peridynamic (PD) nodes at the numerical interface. The corresponding parameters are solved by enforcing the dispersion relation from three versions of PD initially, i.e., bond-based (BBPD), ordinary peridynamics (OPD) and non-ordinary peridynamics (NOPD). The latter part of the research focuses primarily on NOPD for higher dimension simulations. The effectiveness of the NMBC is given for BBPD, OPD and NOPD for 1D simulations, NOPD for 2D simulations with unidirectional and multidirectional waves. A bridging scale decomposition employing a projection approach is then introduced in the concurrent multiscale discretization scheme to further facilitate the information passage between the PD and FEM simulations. To demonstrate the effectiveness of the coupling method, multiple benchmark examples in both 1D and 2D are presented.

TABLE OF CONTENTS

ACKNOWLEDGEMENTS v
ABSTRACT vi
LIST OF TABLES ix
LIST OF FIGURES x
CHAPTER 1 INTRODUCTION 1
CHAPTER 2 GENERAL PERIDYNAMIC FORMULATION 5
2.1 Bond-Based Peridynamics 6
2.2 Ordinary Peridynamics 7
2.3 Non-Ordinary Peridynamics with Correspondence Material 9
2.4 Non-Ordinary Peridynamics with Stabilized Correspondence Material 10
CHAPTER 3 DISPERSION RELATIONS 12
3.1 1D Dispersion Relation 12
3.1.1 Dispersion Relation for Bond Based Peridynamics 12
3.1.2 Dispersion Relation for Ordinary State-Based Peridynamics 14
3.1.3 Non-Ordinary Peridynamic Correspondence Material Dispersion 16
3.1.4 Dispersion Relation for Non-Ordinary Peridynamic Stabilized Correspondence Material 20
3.2 Dispersion Relation of Two Dimensional Non-Ordinary Peridynamic Correspondence Material 25
CHAPTER 4 MATCHING BOUNDARY CONDITIONS FOR PERIDYNAMICS 31
4.1 Matching Boundary Conditions 31
4.2 NMBC for Bond-Based and Ordinary Peridynamics 39
4.2.1 Edge Effects and NMBC 41
4.3 NMBC for Non-Ordinary Peridynamics with Correspondence Material Model 45
4.4 NMBC for NOPD with Stabilized Correspondence Model 49
4.5 Two Dimensional Unidirectional NMBC for Non-Ordinary Peridynamics 54
4.6 Two Dimensional Multidirectional NMBC for Non-Ordinary Peridynamics 59
4.7 Effectiveness of Peridynamic NMBC 64
CHAPTER 5 COUPLING OF FINITE ELEMENT AND PERIDYNAMIC SIMULATIONS . 71

5.1 General Multiscale Discretization Scheme 71
5.2 Governing Equations 72
5.3 Information passage between Finite Element and Peridynamics 73
5.3.1 From Finite Element to Peridynamics 73
5.3.2 From Peridynamics to Finite Element 73
5.4 One-Way Non-Local Matching Boundary Conditions 74
5.5 2D Examples 76
5.6 Two-Way Non-Local Matching Boundary Conditions 81
5.7 Peridynamic Fracture Initiation within a Coupled PD/FEM Simulation 86
CHAPTER 6 CONCLUSION 89
REFERENCES 91
BIOGRAPHICAL SKETCH 95
CURRICULUM VITAE

LIST OF TABLES

Table 1: 1st order MBC coefficients for BBPD, OPD, and NOPD for horizon radius 1-3..... 35

Table 2: Coefficients for arbitrary MBC coefficients for order 1-4 36

Table 3: System energy remaining at Time=54.88 for NOPD with MBC1 from Figure 11 47

Table 4: Effectivity of NMBC for $\delta = \Delta X$ with $\Delta X = 1$ at $t = 54.88$. 52

Table 5: Effectivity of NMBC for $\delta = 2\Delta X$ with $\Delta X = 1$ at $t = 54.88$. 52

Table 6: Effectivity of NMBC for $\delta = 3\Delta X$ with $\Delta X = 1$ at $t = 54.88$. 52

Table 7: Normalized energy at $t = 15$ based on the 2D unidirectional NMBC in Figure 18..... 59

Table 8: NMBC1 effectivity remaining for various neighborhoods with $G = 0$ at $t = 40$ 62

Table 9: Final effectivity of 2D NMBC1 for various neighborhoods at t=40 63

LIST OF FIGURES

Figure 1: Illustration of PD force densities in a) BBPD, b) OPD, and c) NOPD 5

Figure 2: A 1D PD configuration with evenly distributed nodes. 12

Figure 3: Dispersion relations for both standard $(G=0)$ and stabilized NOPD $(G>0)$ with correspondence material with a) $\delta=\Delta X$, b) $\delta=2\Delta X$, c) and $\delta=3\Delta X$ 25

Figure 4: 2D SNOPD correspondence material wave dispersion relations for various selection of G for a) $\delta=\Delta X$, b) $\delta=2\Delta X$, and c) $\delta=3\Delta X$ respectively. 30

Figure 5: Node numbering of the 1D boundary and internal domains where the open node indicates a boundary node and the filled nodes are internal nodes. 31

Figure 6: Wave profile of the BBPD, OPD, and NOPD 1D simulations 40

Figure 7: Comparative results of the BBPD, OPD, NOPD, and MD simulations with a first order matching boundary condition normalizing energy while the wave is in equilibrium .. 41

Figure 8: The revised NMBC for PD: An extra node, labeled as -1, is added to the left boundary domain for a local neighbor interaction 43

Figure 9: Comparative results of the BB, OPD+, and MD simulations with a first order MBC .. 44

Figure 10: System energy remaining for NOPD with standard MBC with minimally required PD boundary regions..... 45

Figure 11: Energy absorption of NMBC for NOPD of different horizon radii 47

Figure 12: PSDs for NOPD horizon radii of 1 through 3 and MD for the displacement prescribed in *(101)*. 48

Figure 13: Convergence of the effectivity of the first order NMBC as the number of nodes within the boundary domain increase 49

Figure 14: PSD for a SNOPD neighborhood of a) $\delta=\Delta X$, b) $\delta=2\Delta X$, and c) $\delta=3\Delta X$ 51

Figure 15: NMBC Effectivity for various $\boldsymbol{G}$ values for NMBC1 of horizon radii a) $\delta=\Delta X$, b) $\delta=2\Delta X$, and c) $\delta=3\Delta X$. The same is demonstrated for NMBC2 with d) $\delta=\Delta X$, e) $\delta=2\Delta X$, and f) $\delta=3\Delta X$ 53

Figure 16: The boundary domain for a unidirectional 2D PD NMBC 55

Figure 17: Contour plots of the y displacement at a) $t = -5$ and b) $t = 7.5$ and c) $t = 15$ for $\delta = \Delta X$ with $G = 1$ for the unidirectional NMBC simulation. 58

Figure 18: Normalized energy history of the 2D unidirectional wave for the cases of a) $\delta = \Delta X$, b) $\delta = 2\Delta X$, and c) $\delta = 3\Delta X$ 58

Figure 19: Contour plots of the y displacement at a) $t = 0$, b) $t = 10$, and c) $t = 40$ for $\delta = \Delta X$, $G = 0$ and NMBC1. 61

Figure 20: Effectivity of the 2D NMBC1 with $G = 0$ for various horizon sizes. 62

Figure 21: 2D NMBC1 multidirectional wave effectivity for various G values for a) $\delta = \Delta X$, b) $\delta = 2\Delta X$, and c) $\delta = 3\Delta X$ 63

Figure 22: Comparison of local reflection coefficients for BBPD, OPD, NOPD, and MD for MBC1 65

Figure 23: Plots for the reflection coefficients for 1D BBPD, OPD, and NOPD 67

Figure 24: Reflection coefficient for higher order NMBC with NOPD for a horizon radius of a) $\delta = 1\Delta X$ and b) $\delta = 2\Delta X$ 68

Figure 25: Reflection coefficients for SNOPD for NMBC1 for neighborhoods a) $\delta = 1\Delta X$, b) $\delta = 2\Delta X$, and c) $\delta = 3\Delta X$ and NMBC2 for neighborhoods d) $\delta = 1\Delta X$, e) $\delta = 2\Delta X$, and d) $\delta = 3\Delta X$ with selected G values 69

Figure 26: Reflection coefficient for 2D MBC of selected G values for a) $\delta = 1\Delta X$, b) $\delta = 2\Delta X$, and c) $\delta = 3\Delta X$ 70

Figure 27: Discretized FEM domain with overlapping PD domain 71

Figure 28: Coupled NOPD/FEM model without interfacial treatment between PD and FEM 76

Figure 29: Allocation of PD nodes within the finite elements for the unidirectional simulation. 77

Figure 30: Total system energy of FEM and PD domains within the coupled unidirectional simulations for a) $\delta = 1\Delta X$, b) $\delta = 2\Delta X$, and c) $\delta = 3\Delta X$ 78

Figure 31: Allocation of PD nodes within the finite elements for the multidirectional wave simulation 80

Figure 32: Total system energy of FEM and PD domains within the coupled multidirectional simulations for a) $\delta = 1\Delta X$, b) $\delta = 2\Delta X$,c) $\delta = 3\Delta X$ 80

Figure 33: Depiction of the 2-Way NMBC coupling 83

Figure 34: Total system energy for 2-Way NMBC of PD domains within the coupled unidirectional simulations for a) $\delta = 1\Delta X$, b) $\delta = 2\Delta X$,c) $\delta = 3\Delta X$ 85

Figure 35: Dual simulations showing the initial setup between a full PD domain and a coupled PD/FEM domain with a pre-crack. 87

Figure 36: The number of bonds broken in the full PD simulation and the coupled PD/FEM simulation compared against normalized simulation time..... 88

CHAPTER 1

INTRODUCTION

With a growing focus on simulation based engineering it is desirable to establish computational tools that are capable of incorporating key mechanisms at a wide range of spatial and temporal scales. This has largely motivated the development of a broad class of multiscale computational methods. One example is the coupled atomistic/continuum simulation approach that seeks to integrate atomistic with continuum representations [1]. More recently, these efforts have been extended to integrating peridynamics (PD) with conventional continuum representations of solids [2]. Peridynamics is a reformulation of the continuum theory based on an integro-differential formulation and allows for the modeling of conditions which would cause mathematical singularities in approaches such as the Finite Element Method (FEM) [3]–[5]. In what began as a simple spring like connection between neighboring nodes, peridynamics has expanded in capability to model nearly any material with the introduction of the state-based Peridynamics [5], [6]. Peridynamics utilizes a non-local node interaction in that the forces between nodes are not limited to the nearest neighbor but interact up to a radial distance called the horizon. All nodes within this horizon, identified as the family, interact with the node at the center.

A critical step in developing the multiscale method is the treatment of the PD/continuum interface. Improper treatments can lead to artificial wave reflections that pollute the numerical solution. As such, developing the proper interfacial boundary condition becomes a key component in establishing robust multiscale simulation models. This class of interfacial boundary conditions are generally referred to as non-reflective boundary conditions as they are aimed at either

eliminating or minimizing the wave reflection at the interface. A force based coupling was used in [7], [8] to couple PD with classical elastic models. Energy based coupling methods such as the Arlequin and Morphing methods are implemented in [9] which were adapted from atomistic methods of the same type in [10]–[13]. Peridynamics is also coupled to finite element models in [14], [15]. Wang et al. have implemented a MBC approach for a state-based peridynamic bond-based material [2]. Another type of absorbing boundary layer for PD was implemented in a Perfectly Matched Layer (PML) in [16], [17]. It should be noted that all the coupling approaches demonstrated so far have been applied only to a particular version of PD, i.e., BBPD or NOPD. No absorbing boundary condition has been demonstrated to date for OPD to the author's knowledge.

Motivated by the current developments, this Ph.D. work seeks to establish non-reflective boundaries in PD based on the matching boundary condition (MBC) approach. MBC was originally developed by Wang and Tang [11, 12] in the context of coupling molecular dynamics (MD) with FEM. Unlike the conventional absorbing boundary condition, this approach accounts for the boundary condition at the atomistic/continuum interface through a finite difference form. The implementation is relatively simple as the interfacial condition is parameterized. Stability of MBC was shown in [13]. More recently, Wang proposed a framework of MBC for state-based PD formulation and demonstrated its effectiveness in one-dimensional PD simulations [2].

The main objective of this PhD research is to study the general application of MBC, and its adaptation to PD named Non-Local Matching Boundary Conditions (NMBC), for the three major categories of PD that have been proposed so far, i.e., bond-based (BBPD), ordinary peridynamics (OPD), and non-ordinary peridynamics (NOPD) with a correspondence material. An

additional extension of NOPD is also analyzed which is identified as an NOPD stabilized correspondence material (SNOPD). SNOPD mitigates the zero energy modes that are present within the NOPD correspondence material. The numerical wave dispersion formulas for PD are not generally known and can vary depending on the implementation of PD and mesh discretization that is being used. As such, numerical dispersion relations are derived for the three PD formulations in 1D and for NOPD/SNOPD in 2D. These relations are important for the computational implementations of MBC and compliment the dispersion relations that have been derived in [2], [3], [18], and [19]. Based on these, MBCs are developed for the aforementioned three major PD formulations. The robustness of the MBCs is further demonstrated through both 1D and 2D examples. Comparisons are made among BBPD, OPD, NOPD, and classical Molecular Dynamics (MD). In particular, we show that MBC implementations for OPD and NOPD are fundamentally different from the corresponding implementations in BBPD that has been derived in [2]. More specifically, nonlocal versions of the MBC, NMBC, have been derived for OPD and NOPD, and the effectiveness of the NMBC in achieving non-reflective boundaries are quantified. The NMBC is further extended into a 2-way interfacial boundary condition based on [2] and implemented for 2D NOPD simulations. The effectiveness of this 2-way NMBC is evaluated for unidirectional waves.

The rest of the dissertation is organized as follows: an outline of the general peridynamics formulation is provided in Chapter 2, followed by the numerical dispersion relations that are derived for the three versions of PD in 1D and NOPD in 2D in Chapter 3. The MBCs are discussed in Chapter 4, followed by extensive numerical studies in 1D and 2D. A methodology for coupling

the finite element method and PD is given in Chapter 5 with numerical studies in 2D. Conclusions are provided in Chapter 6 based on the numerical implementations.

CHAPTER 2

GENERAL PERIDYNAMIC FORMULATION

To begin, the general peridynamic equation of motion, as given in [5], is

$$\rho\ddot{\mathbf{u}}_I\left(\mathbf{X}_I,t\right)=\int_{H_{\mathbf{X}}}\left\{\mathbf{T}\left[\mathbf{X}_I,t\right]\left\langle\mathbf{X}_J-\mathbf{X}_I\right\rangle-\mathbf{T}\left[\mathbf{X}_J,t\right]\left\langle\mathbf{X}_I-\mathbf{X}_J\right\rangle\right\}dV_J+\mathbf{b}\left(\mathbf{X}_I,t\right) \tag{1}$$

in which ρ is mass density, $\mathbf{u}$ is displacement where super-imposed dots indicate temporal derivatives, $\mathbf{X}_I$ is the material coordinate of a mass point indexed by I and t is time. The integration on the right hand side of Eq. (1) is performed over domain $H_{\mathbf{X}}$ that is referred to as the horizon and is typically defined as a radius δ centered at $\mathbf{X}_I$. $\underline{\mathbf{T}}\left[\mathbf{X}_I,t\right]\left\langle\mathbf{X}_J-\mathbf{X}_I\right\rangle$ is called the force density vector state that is evaluated at $\mathbf{X}_I$. The angular bracket indicates that the force density operates on the Lagrangian bond vector $\mathbf{X}_J-\mathbf{X}_I$. The three prominent PD formulation approaches, as stated before, are BBPD, OPD, and NOPD. Each has unique characteristics that are imposed on the general PD framework shown in (1). Representative differences between these PD methods can be seen in Figure 1.

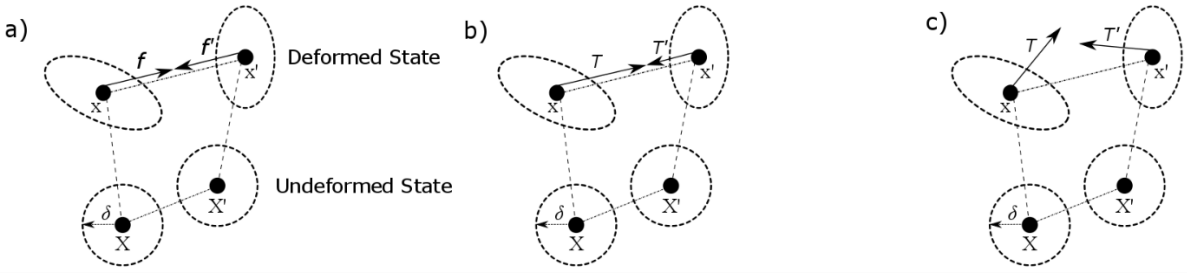

Figure 1: Illustration of PD force densities in a) BBPD, b) OPD, and c) NOPD

2.1 Bond-Based Peridynamics

Bond-Based PD is based on the assumption that the interactions between nodes are equal and opposite and interactions are defined with one constitutive parameter. Within BBPD the force density expression between nodes in a family can be equated to each other as $\underline{\mathrm{T}}\left[\mathbf{X}_I, t\right]\left\langle \mathbf{X}_J - \mathbf{X}_I \right\rangle = -\underline{\mathrm{T}}\left[\mathbf{X}_J, t\right]\left\langle \mathbf{X}_I - \mathbf{X}_J \right\rangle$. It can then be shown that (1) is further simplified as

$$\rho \ddot{\mathbf{u}}_I \left(\mathbf{X}_I, t\right) = \int_{H_X} f\left(\mathbf{u}_J - \mathbf{u}_I, \mathbf{X}_J - \mathbf{X}_I\right) dV_J + b\left(\mathbf{X}_I, t\right) \tag{2}$$

in which the internal force density function $f\left(\mathbf{u}_J - \mathbf{u}_I, \mathbf{X}_J - \mathbf{X}_I\right)$ is defined as

$$f\left(\mathbf{u}_J - \mathbf{u}_I, \mathbf{X}_J - \mathbf{X}_I\right) = \left[C_1 s\left(\mathbf{u}_J - \mathbf{u}_I, \mathbf{X}_J - \mathbf{X}_I\right) - C_2 T\right] \frac{\mathbf{x}_J - \mathbf{x}_I}{\left|\mathbf{x}_J - \mathbf{x}_I\right|} \ . \tag{3}$$

Equation (3) is derived through the use of strain energy density and is described in [3], [9], [20], and [21]. The value of $\mathbf{x}_I$ is to represent the deformed location of the nodes and constants C_1 and C_2 pertain to material and thermal expansion properties. In this work thermal effects are not considered, leaving only C_1 to be defined in 1D as

$$C_1 = \frac{2E}{A\delta^2} \tag{4}$$

for a linear elastic solid where E is Young's Modulus, A is the cross sectional area, and δ is the radius of the horizon, H_X. Also, this particular constitutive constant, C_1, is identified as the prototype microelastic material in PD literature. The component of the BBPD internal force density that is subject to displacement effects is called the stretch and is defined as

$$s\left(\mathbf{u}_J-\mathbf{u}_I,\mathbf{X}_J-\mathbf{X}_I\right)=\frac{\left|\mathbf{x}_J-\mathbf{x}_I\right|-\left|\mathbf{X}_J-\mathbf{X}_I\right|}{\left|\mathbf{X}_J-\mathbf{X}_I\right|} \tag{5}$$

with $\mathbf{x}_J-\mathbf{x}_I=\mathbf{X}_J-\mathbf{X}_I+\mathbf{u}_J-\mathbf{u}_I$.

2.2 Ordinary Peridynamics

Ordinary Peridynamics steps beyond BBPD in that the force density state evaluation involves contribution from the bonds and forces between pairs of material points are not necessarily equal, though still assumed to be in opposing directions as depicted in Figure 1. OPD expands on BBPD in that it uses two constitutive parameters such that isotropic linear elastic materials can be equivalently defined.

The force density state for OPD is constructed of terms that are related to the dilatation of the volume ascribed to a node. This dilatation is defined as

$$\theta\left(\underline{\mathbf{e}}\right)=\frac{3}{m}\left(w\underline{\mathbf{R}}\right)\bullet\underline{\mathbf{e}} \tag{6}$$

where m is the weighted volume, w is identified as the influence function which can be a variety of different values but is chosen here to be 1. The underbar represents a state and "$\bullet$" represents a dot product between states defined in [5]. In addition, $\underline{e}$ is the extension scalar state, $\underline{\mathbf{R}}$ is the initial state representing the initial bond length between nodes, and $\underline{\mathbf{r}}$ is the deformed state representing the length between nodes through time. In the discretized version, the definitions of the terms in Eq.(6) are given as

$$\begin{aligned} m_I&=\left(\underline{w}_{IJ}\underline{\mathbf{R}}_{IJ}\right)\bullet\underline{\mathbf{R}}_{IJ}, \quad \underline{\mathbf{r}}_{IJ}=\left|\mathbf{x}_J-\mathbf{x}_I\right| \\ \underline{\mathbf{e}}_{IJ}&=\underline{\mathbf{r}}_{IJ}-\underline{\mathbf{R}}_{IJ}, \qquad \underline{\mathbf{R}}_{IJ}=\left|\mathbf{X}_J-\mathbf{X}_I\right| \end{aligned}. \tag{7}$$

Based on the above definitions, the dilation and weighted volume are discretized in 1D as

$$\theta_I(\underline{e}_{IJ}) = \sum_J \frac{3}{m_I}(\underline{w}_{IJ}\underline{R}_{IJ})\underline{e}_{IJ}V_J \qquad\qquad m_I = \sum_J \underline{w}_{IJ}\underline{R}_{IJ}^2 V_J \tag{8}$$

in which V_J is the volume represented by node J. The force density magnitude for each node is given as

$$\underline{t}_{IJ} = \frac{3k\theta}{m}\underline{w}_{IJ}\underline{R}_{IJ} + \frac{15\mu}{m}\underline{w}_{IJ}\underline{e}_{IJ}{}^d \tag{9}$$

where k and μ are the bulk and shear moduli respectively and

$$\underline{e}_{IJ}^i = \frac{\theta_I \underline{R}_{IJ}}{3} \qquad\qquad \underline{e}_{IJ}^d = \underline{e}_{IJ} - \underline{e}_{IJ}^i \tag{10}$$

are the isotropic and deviatoric extension scalar states respectively. One can further simplify (9) by plugging in (10) to get

$$\underline{t}_{IJ} = c_1\underline{R}_{IJ} + \frac{15\mu}{m_I}\underline{w}_{IJ}\underline{e}_{IJ} \qquad \text{with} \qquad q_1 = \underline{w}_{IJ}\theta_{IJ}\left(\frac{3k}{m_I} - \frac{15\mu}{3m_I}\right). \tag{11}.$$

This force density magnitude, $\underline{t}_{IJ}$, can be used within the peridynamic equation of motion as

$$T\left\langle \mathbf{X}_J - \mathbf{X}_I \right\rangle = \underline{t}_{IJ}\underline{\mathbf{M}}_{IJ} \tag{12}$$

in which $\underline{\mathbf{M}}_{IJ} = \dfrac{\mathbf{x}_J - \mathbf{x}_I}{\left|\mathbf{x}_J - \mathbf{x}_I\right|}$.

2.3 Non-Ordinary Peridynamics with Correspondence Material

In NOPD, the force state in (1) can be related to the concept of stress defined in continuum mechanics based on energy density equivalence [5], [6] which is identified as a NOPD correspondence material model, and this leads to

$$\mathbf{T}\left[\mathbf{X}_I, t\right]\left\langle \mathbf{X}_J - \mathbf{X}_I \right\rangle = w_{IJ}\mathbf{P}^T\left[\mathbf{X}_I, t\right]\bullet\left(\mathbf{K}_I\left[\mathbf{X}_I\right]\right)^{-1}\bullet\left(\mathbf{X}_J - \mathbf{X}_I\right) \tag{13}$$

where w_{IJ} is a scalar weight function, $\mathbf{P}\left[\mathbf{X}_I, t\right]$ is the 1st Piola-Kirchhoff stress evaluated at $\mathbf{X}_I$ and $\mathbf{K}_I\left[\mathbf{X}_I\right]$ is referred to as the shape tensor, also evaluated at $\mathbf{X}_I$. In NOPD theory, the shape tensor is defined as the tensor product of the reference position vector state, expressed as

$$\mathbf{K}_I\left[\mathbf{X}_I\right] = \int_{H_X} w_{IJ}\left(\mathbf{R}_{IJ} \otimes \mathbf{R}_{IJ}\right) dV_J \,. \tag{14}$$

Similar to the definition of the shape tensor, one may also define a deformed shape tensor [5], given as

$$\mathbf{k}_I\left[\mathbf{X}_I\right] = \int_{H_X} w_{IJ}\left(\mathbf{r}_{IJ} \otimes \mathbf{R}_{IJ}\right) dV_J \tag{15}$$

in which $\mathbf{r}_{IJ} = \mathbf{x}_J - \mathbf{x}_I$ with $\mathbf{x}$ defined as the spatial coordinate and $\mathbf{x}_I = \mathbf{X}_I + \mathbf{u}_I$, $\mathbf{x}_J = \mathbf{X}_J + \mathbf{u}_J$ where $\mathbf{u}_I$, $\mathbf{u}_J$ are the displacement vector corresponding to mass point *I* and *J*.

With (14) and (15) above, the non-local deformation gradient is given as

$$\mathbf{F}\left[\mathbf{X}_I\right] = \mathbf{k}\left[\mathbf{X}_I\right]\bullet\left(\mathbf{K}\left[\mathbf{X}_I\right]\right)^{-1}. \tag{16}$$

For the constitutive model, we assume a small strain, linear isotropic elasticity theory. The strain $\boldsymbol{\varepsilon}$ and stress $\boldsymbol{\sigma}$ are given as:

$$\boldsymbol{\varepsilon} = \frac{1}{2}\left(\mathbf{F} + \mathbf{F}^T\right) - \mathbf{I} \tag{17}$$

$$\boldsymbol{\sigma} = \mathbf{P} = \mathbf{C} : \boldsymbol{\varepsilon} \tag{18}$$

in which $\mathbf{C}$ is the elasticity tensor.

2.4 Non-Ordinary Peridynamics with Stabilized Correspondence Material

Recently Silling introduced a stabilized version of non-ordinary peridynamics for the purpose of mitigating the zero energy modes [22]. Compared with Eq.(1), an additional stabilization term is added to the internal force density:

$$\mathbf{T}\left[\mathbf{X}_I, t\right]\left\langle \mathbf{X}_J - \mathbf{X}_I \right\rangle = w_{IJ}\left(\mathbf{P}^T\left[\mathbf{X}_I, t\right] \bullet \left(\mathbf{K}_I\left[\mathbf{X}_I\right]\right)^{-1} \bullet \left(\mathbf{X}_J - \mathbf{X}_I\right) + \frac{GC_{BB}}{w_0}\boldsymbol{z}\left[\boldsymbol{X}_I\right] \right) \tag{19}$$

in which G is a stabilization parameter and C_{BB} is the nominal micromodulus, given as

$$C_{BB} = \begin{cases} \dfrac{18k}{\pi\delta^5} & \text{D=3} \\ \dfrac{12k'}{\pi h_2 \delta^4} & \text{D=2} \\ \dfrac{2E}{h_1\delta^3} & \text{D=1} \end{cases} \tag{20}$$

in which D is the dimension, k is the bulk modulus, $k' = \dfrac{E}{2\left(1-\nu\right)}$ for plane stress with E the Young's modulus and ν the Poisson's ratio. For plane strain $k' = \dfrac{E}{2\left(1-\nu-2\nu^2\right)}$. For the case of

two dimension h_2 is the plate thickness, and for one dimension h_1 is the cross-sectional area. The remaining terms are defined as

$$w_0 = \int_{H_x} w_{IJ}\ dV_J \tag{21}$$

$$\boldsymbol{z}\left[\mathbf{X}_I\right] = \mathbf{r}_{IJ} - \mathbf{F}\bullet\mathbf{R}_{IJ} \tag{22}$$

It should be noted that parameter G is to be defined by the user and should be a constant positive number on the order of 1.

CHAPTER 3

DISPERSION RELATIONS

3.1 1D Dispersion Relation

In the 1D case, we consider the configuration as shown in Figure 2. The PD nodes are assumed to have a uniform spacing of ΔX with an arbitrary neighborhood size. The dispersion relation is then derived based on those initial assumptions for all three PD models. Some further assumptions are stated for each individual model.

3.1.1 Dispersion Relation for Bond Based Peridynamics

We consider a 1D case to demonstrate the BBPD application for the purpose of deriving the dispersion relation. As shown in Figure 2, nodes are assumed to be equally spaced with distance of ΔX between the nearest nodes. Further, we assume the that any node will interact with its neighboring nodes up to a radius of $n\Delta X$. This assumption is an equivalent statement of employing a Lagrangian kernel in this particle method.

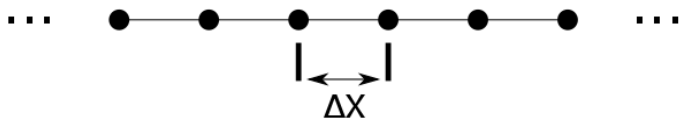

Figure 2: A 1D PD configuration with evenly distributed nodes.

Under these assumptions the BBPD equation of motion for an arbitrary horizon can be discretized and simplified as

$$\rho(x)\ddot{u}_I(X_I,t)=\sum_{\substack{k=-n\\k\neq 0}}^{n}\left[\frac{2EW_i}{\delta^2}\frac{u_{I+k}-u_I}{|k\Delta X|}\right]\Delta X \tag{23}$$

where we have assumed small deformation such that $|X_{I+k}-X_I|=|k\Delta X|\geq|u_{I+k}-u_I|$. In addition W_k is a volume correction factor defined as

$$W_k=\begin{cases}\frac{1}{2} & |k|=n\\ 1 & |k|<n\end{cases}. \tag{24}$$

Testing the case above in (23) we let $n=1$ which represents a family of only the local neighbors,

$$\begin{aligned}\rho(x)\ddot{u}_I(X_I,t)&=\sum_{\substack{k=-1\\k\neq 0}}^{1}\left[\frac{2EW_k}{(\Delta X)^2}\frac{u_{I+k}-u_I}{|k|}\right]\\&=\frac{E(u_{I-1}-2u_I+u_{I+1})}{\Delta X^2}\end{aligned}. \tag{25}$$

As can be seen from Eq.(25), doing so recovers the well-known formula for approximating a second derivative using a center difference scheme. To perform dispersion analysis, the solution is assumed to be in the form of

$$u_I=\bar{u}\,e^{\bar{i}(\omega t+\xi I\Delta X)} \tag{26}$$

in which $\bar{i}=\sqrt{-1}$ is the imaginary number, ω is the angular frequency and ξ is the wave vector in one dimension. Based on (26) the following can be obtained.

$$u_{I+k}=\bar{u}\,e^{\bar{i}(\omega t+\xi(I+k)\Delta X)}=u_I\,e^{\bar{i}\xi k\Delta X}\quad\text{and}\quad\ddot{u}_I=-\omega^2u_I \tag{27}$$

By plugging (27) into (23) and evaluating at $I = 0$ we get

$$-\rho\omega^2 = \frac{2E}{\delta^2(\Delta X)^2}\sum_{\substack{k=-n\\k\neq 0}}^{n}\left[\frac{W_i\left(e^{\bar{i}\xi k\Delta X}-1\right)}{|k|}\right] \tag{28}$$

The summation can be broken into two parts, and further simplified with Euler's formula, which leads to the dispersion relation for an arbitrary horizon radius for BBPD.

$$\omega = \frac{2c}{n\Delta X}\sqrt{\sum_{k=1}^{n}\frac{2W_k}{k}\sin\left(\frac{\xi k\Delta X}{2}\right)^2} \tag{29}$$

Note that c is the elastic wave speed of the material. In the local case where $n=1$ the BBPD dispersion relation reduces to

$$\omega_{\delta=1} = \frac{2c\left|\sin\left[\frac{\Delta X\zeta}{2}\right]\right|}{\Delta X}\ . \tag{30}$$

3.1.2 **Dispersion Relation for Ordinary State-Based Peridynamics**

In order to ascertain the dispersion relation for OPD we need to begin with the extension scalar state which is given as

$$\underline{e}_{IJ} = \sqrt{(x_J - x_I)^2} + \sqrt{(X_J - X_I)^2}\ . \tag{31}$$

An arbitrary weighting function can be expressed as

$$m_I = A_n V_J \Delta X^2 \underline{w}_{IJ} \quad \text{with} \quad A_n = \frac{n(n+1)(2n+1)}{3}\ . \tag{32}$$

The formulation for the OPD linear elastic model uses the constitutive pair of bulk and shear moduli. A standard conversion can be made if we compare OPD to the other PD models that use

Poisson's ratio and Young's Modulus instead. In the case where Poisson's ratio is given as 0.25, q_1, given in (11), is now zero. This simplifies (11) to be

$$\underline{t}_{IJ} = \frac{6E}{m}\,\underline{w}_{IJ}\,\underline{e}_{IJ} \quad . \tag{33}$$

From here the OPD equation of motion can be substituted into (1) to get

$$\rho\ddot{u}_I\left(X_I,t\right) = \int_{H_X}\left(t_{IJ}+t_{JI}\right)\frac{x_J - x_I}{\left|x_J - x_I\right|}dV_J \quad . \tag{34}$$

Eq. (34) can be simplified by substituting (33) and (31). Then discretization leads to

$$\rho\ddot{u}_I = \sum_{\substack{k=-n\\k\neq 0}}^{n}\left(-\frac{2E_k\left(\left|k\Delta X\right|-\left|x_I - x_{I+k}\right|\right)}{\Delta X^2 A_n}\right)\underline{M}_{I(I+k)} \tag{35}$$

If we assume again that $\left|X_{I+k}-X_I\right| = \left|k\Delta X\right| \geq \left|u_{I+k}-u_I\right|$ and further simplify then the discretized OPD equation of motion can be expressed as

$$\rho\ddot{u}_I = \sum_{\substack{k=-n\\k\neq 0}}^{n}\left(\frac{2E\left(u_{I+k}-u_I\right)}{\Delta X^2 A_n}\right) . \tag{36}$$

As a check let $n=1$ and $A_n=2$, Eq. (36) becomes

$$\rho\ddot{u}_I = \frac{E\left(u_{I-1}-2u_I+u_{I+1}\right)}{\left(\Delta X\right)^2} \tag{37}$$

which is, again, the center difference scheme.

By substituting (27) into (36), as done for BBPD, the dispersion relation can be obtained for an arbitrary horizon radius.

$$\omega = \frac{2c\sqrt{2}}{\Delta X\sqrt{A_n}}\sqrt{\sum_{k=1}^{n}\sin\left[\frac{k\Delta X\zeta}{2}\right]^2} \tag{38}$$

Letting $n=1$ and $A_n=2$ gives the local dispersion relation for OPD.

$$\omega_{\delta=1} = \frac{2c\left|\sin\left[\frac{\Delta X\zeta}{2}\right]\right|}{\Delta X} \tag{39}$$

We note that the OPD dispersion relation obtained here is the same as that given for the local BBPD in 1D case for a local neighborhood.

3.1.3 **Non-Ordinary Peridynamic Correspondence Material Dispersion**

To begin the dispersion relation derivation for NOPD we first evaluate the shape tensor K according to (14). In the 1D case,

$$K\left[X_I\right] = \sum_{\substack{i=-n\\ i\neq 0}}^{n} w_{I,I+i}\left(i\Delta X\right)^2\Delta X \tag{40}$$

Note that here n denotes the number of neighbors in the horizon radius, i.e., $\delta = n\Delta X$ where $n=1$ represents the case of the local neighbor.

Similarly for the deformed shape tensor k,

$$k\left[X_I\right] = \sum_{\substack{i=-n\\ i\neq 0}}^{n} w_{I,I+i}\left(i\Delta X + u_{I,I+i}\right)\left(i\Delta X\right)\Delta X \tag{41}$$

where $u_{I,I+i} = u_{I+i} - u_I$ and $r_{IJ} = R_{IJ} + u_{IJ} = R_{IJ} + u_{I,I+i}$. Assuming a constant weight function, the nonlocal deformation gradient is simplified as

$$F\left[X_I\right] = k\left[X_I\right] \bullet \left(K\left[X_I\right]\right)^{-1} = \frac{\sum_{\substack{i=-n \\ i\neq 0}}^{n} \left[i^2 \Delta X + i u_{I,I+i} \right]}{\sum_{\substack{i=-n \\ i\neq 0}}^{n} i^2 \Delta X} \tag{42}$$

from which we can obtain the non-local small strain,

$$\varepsilon_I = \frac{\sum_{\substack{i=-n \\ i\neq 0}}^{n} i u_{I,I+i}}{\Delta X A_n} \ . \tag{43}$$

Following the assumption of linear elasticity, the non-local stress is then given as

$$P_I = \sigma_I = E\varepsilon_I = E \frac{\sum_{\substack{i=-n \\ i\neq 0}}^{n} i u_{I,I+i}}{\Delta X A_n} \ . \tag{44}$$

Based on Eq. (44) the force state in (13) can then be simplified to

$$T\left[X_I, t\right]\left\langle X_J - X_I \right\rangle = \frac{E}{\Delta X^3} \frac{i' \sum_{\substack{i=-n \\ i\neq 0}}^{n} i u_{I,I+i}}{A_n^2} \tag{45}$$

in which $i'\Delta X = X_J - X_I$. In a similar way, it can be shown that

$$T\left[X_J,t\right]\left\langle X_I - X_J\right\rangle = \frac{E}{\Delta X^3}\frac{j'\sum_{\substack{j=-n\\ j\neq 0}}^{n} ju_{J,J+j}}{A_n^2} \tag{46}$$

in which j' and j are indices introduced to denote the neighboring nodes of $\boldsymbol{J}$, i.e., $j'\Delta X = X_I - X_J$ and one can see that $\boldsymbol{i'} = -\boldsymbol{j'}$ based on the definitions.

With the 1D force state expressions derived above, the simplified 1D NOPD equation of motion can be shown to be

$$\rho\ddot{u}_I = \frac{1}{A_n^{\,2}}\frac{E}{\Delta X^2}\sum_{\substack{i=-n\\ i\neq 0}}^{n}\sum_{\substack{j=-n\\ j\neq 0}}^{n} iju_{I+i,I+i+j} \tag{47}$$

To demonstrate the application of (47), we assume the specific case of nearest neighbor interaction so that $n=1$. The last term in Eq. (47) can be further written into four terms based on the combinations of indices, i.e.,

$$\begin{aligned} &k'=-1,\ j=-1,1:\ (-1)(-1)\left(u_{I-2}-u_{I-1}\right)+(-1)(1)\left(u_I-u_{I-1}\right)\\ &k'=\ \ 1,\ j=-1,1:\ (\ \ 1)(-1)\left(u_I-u_{I+1}\right)+(1)(1)\left(u_{I+2}-u_{I+1}\right) \end{aligned}. \tag{48}$$

Thus Eq. (47) yields

$$\rho\ddot{u}_I = E\frac{\left(u_{I-2}-2u_I+u_{I+2}\right)}{4\Delta X^2}. \tag{49}$$

This result essentially provides the center difference scheme for approximating the second spatial derivative, but is utilizing information that is two nodes away from the center node rather than the nearest neighbors. This nodal skipping scheme can produce non-physical effects in that it

neglects the nearest interactions. In the general case, it has been shown that the approximation of the derivatives can be equivalently obtained using the moving least squares reproducing kernel particle method (RKPM) [23].

Substituting (26) and (27) into (47) and evaluating at $I = 0$ leads to

$$-\rho\omega^2 u_0 = \frac{1}{A_n^{\,2}} \frac{E u_0}{\Delta X^2} \left(\sum_{\substack{i=-n \\ i\neq 0}}^{n} i e^{\bar{i}\,\xi i \Delta X} \right)^2 \tag{50}$$

The 1D discrete NOPD wave dispersion formula for an arbitrary horizon radius is then given as

$$\omega = \frac{6c \left| \sum_{m=1}^{n} m \sin\left(\xi m \Delta X\right) \right|}{\Delta X \cdot n(n+1)(2n+1)} \tag{51}$$

with *c* the wave speed of the material.

Remarks: Eq.(51) is equivalent to Eq.(57) obtained in [19] by noting that the two summations under the square root in Eq.(57) of Ref. [19] are independent of each other and therefore can be expressed as the product of two sums. Further simplification can be made by observing that the two sums only differ by a common factor.

The analytical dispersion relation can be obtained from Eq.(51) by enforcing $\Delta X = \frac{\delta}{n}$ then let $n \to \infty$ to have

$$\lim_{n\to\infty} \omega = \lim_{n\to\infty} \frac{6c \left| \sum_{m=1}^{n} m \sin\left(\xi m \frac{\delta}{n}\right) \right|}{\delta(n+1)(2n+1)} = \frac{3c \left| \sin\left(\delta\xi\right) - \delta\xi \cos\left(\delta\xi\right) \right|}{\delta^3 \xi^2} \tag{52}$$

which gives the NOPD analytical solution as demonstrated in [19]. This corresponds to the *m*-convergence as defined in [24]. The next convergence to be examined here is the δ-convergence, which is obtained by letting δ go to zero while keeping n fixed. Again substitute $\Delta X = \frac{\delta}{n}$ into (51) and take the limit:

$$\lim_{\delta \to 0} \omega = \lim_{n \to \infty} \frac{6c \left| \sum_{m=1}^{n} m \sin\left(\xi m \frac{\delta}{n} \right) \right|}{\delta (n+1)(2n+1)} = c\xi \tag{53}$$

which shows that NOPD converges to the exact classical solution.

The last convergence shown here is the δm-convergence, defined by taking the limit of $\delta \to 0$ and $n \to \infty$:

$$\lim_{n \to \infty, \delta \to 0} \frac{6c \left| \sum_{m=1}^{n} m \sin\left(\xi m \frac{\delta}{n} \right) \right|}{\delta (n+1)(2n+1)} = \lim_{\delta \to 0} \frac{3c \left| \sin(n\xi) - \delta \xi \cos(n\xi) \right|}{n^3 \xi^2} = c\xi \tag{54}$$

which demonstrates that the discrete wave dispersion converges to the analytical PD solution which then uniformly converges to the classical solution.

Letting $n = 1$ in (51) we get the local dispersion relation for NOPD

$$\omega_{\delta=1} = \frac{c \left| \sin\left[\Delta X \xi \right] \right|}{\Delta X} \tag{55}$$

3.1.4 Dispersion Relation for Non-Ordinary Peridynamic Stabilized Correspondence Material

Eq. (19) can be equivalently expressed as

$$\mathbf{T}\left[\mathbf{X}_I, t\right]\left\langle \mathbf{X}_J - \mathbf{X}_I \right\rangle = \mathbf{T}_I^C + \mathbf{T}_I^S \tag{56}$$

in which $\mathbf{T}_I^C$ stands for the correspondence force density and $\mathbf{T}_I^S$ is the stabilized force density. The equation of motion corresponding to the decomposition of Eq.(56) is given as

$$\rho \ddot{\mathbf{u}}_I\left(\mathbf{X}_I, t\right) = \int_{H_\mathbf{x}} \left(\mathbf{T}_I^C - \mathbf{T}_J^C\right) dV_J + \int_{H_\mathbf{x}} \left(\mathbf{T}_I^S - \mathbf{T}_J^S\right) dV_J \tag{57}$$

The first integrand is solved to be the same as the corresponding one in (51). The second integrand can be expressed as

$$\int_{H_\mathbf{x}} \left(\mathbf{T}_I^S - \mathbf{T}_J^S\right) dV_J = w_{IJ} \frac{GC_{BB}}{w_0} \sum_{J \in H_{\mathbf{x}_I}} \left(\boldsymbol{z}\left[\mathbf{X}_I\right] - \boldsymbol{z}\left[\mathbf{X}_J\right]\right) \Delta V_J \tag{58}$$

According to the definition of $\boldsymbol{z}\left[\mathbf{X}_I\right]$, the 1D version is

$$z\left[X_I\right] = u_{IJ} - \left(\frac{\sum_{\substack{i=-n \\ i \neq 0}}^{n} i u_{I,I+i}}{A_n} \right) i' \tag{59}$$

Note that $r_{IJ} = -r_{JI}$ as well as $R_{IJ} = -R_{JI}$ then from (59) we can substitute back into Eq. (58) to get

$$\sum_{J \in H_\mathbf{x}} \left(\mathbf{T}_I^S - \mathbf{T}_J^S\right) \Delta V_J = w_{IJ} \frac{GC_{BB}}{w_0} \sum_{\substack{i=-n \\ i \neq 0}}^{n} \left(2u_{I,I+i} - i \frac{\sum_{j=-n}^{n} \left[j u_{I+i,I+i+j} \right]}{A_n} \right) \Delta V_J \tag{60}$$

We can then combine (60) with the result from (47) to arrive at the stabilized NOPD equation of motion:

$$\rho\ddot{u}_I = \frac{1}{A_n^{\,2}}\frac{E}{\Delta X^2}\sum_{\substack{i=-n\\ i\neq 0}}^{n}\sum_{\substack{j=-n\\ j\neq 0}}^{n} iju_{I+i,I+i+j} + w_{IJ}\frac{GC_{BB}}{w_0}\sum_{\substack{i=-n\\ i\neq 0}}^{n}\left(2u_{I,I+i} - i\frac{\sum_{j=-n}^{n}\left[ju_{I+i,I+i+j}\right]}{A_n}\right)\Delta V_J \tag{61}$$

If the influence function is assumed to be a constant for all bonds, then

$$w_0 = \sum_{\substack{i=-n\\ i\neq 0}}^{n} w_{IJ}\Delta V_J = 2w_{IJ}n\Delta V_J \tag{62}$$

The stabilized NOPD equation of motion is then further written as

$$\rho\ddot{u}_I = \frac{1}{A_n^{\,2}}\frac{E}{\Delta X^2}\sum_{\substack{i=-n\\ i\neq 0}}^{n}\sum_{\substack{j=-n\\ j\neq 0}}^{n} iju_{I+i,I+i+j} + \frac{GC_{BB}}{2n}\sum_{\substack{i=-n\\ i\neq 0}}^{n}\left(2u_{I,I+i} - i\frac{\sum_{j=-n}^{n}\left[ju_{I+i,I+i+j}\right]}{A_n}\right) \tag{63}$$

If we let $n=1$ we can get the local equation of motion for the stabilized NOPD correspondence material which is

$$\rho\ddot{u}_I = \frac{E}{2}\left(\frac{\left(u_{I-2} - 2u_I + u_{I+2}\right)}{2\Delta X^2} + \frac{G\left(-u_{I-2} + 4u_{I-1} - 6u_I + 4u_{I+1} - u_{I+2}\right)}{\Delta X^3}\right) \tag{64}$$

Here, in comparison to (49), it is easy to see that the nearest interactions are added through the stabilization forces. We also note that the second term in Eq.(64) has a similar form to the one that is derived from the method of matching differential operator (MDO) in coarsening the molecular dynamics equation of motion for harmonic lattice [25].

Substituting in Eqs. (26) and (27) into (63) we obtain the following dispersion relation:

$$\omega=\sqrt{\frac{4}{A_n^{\,2}}\frac{E}{\rho\Delta X^2}\left(\sum_{m=1}^{n}m\sin\left(\xi m\Delta X\right)\right)^2-\frac{4GC_{BB}}{2\rho n}\left(\sum_{m=1}^{n}\left(\cos\left(\xi m\Delta X\right)-1\right)+\frac{\left(\sum_{m=1}^{n}m\sin\left(\xi m\Delta X\right)\right)^2}{A_n}\right)} \tag{65}$$

Substituting the nominal micromodulus (20) into (65) we can get the final wave dispersion for 1D stabilized NOPD:

$$\omega=2c\sqrt{\left(\frac{\sum_{m=1}^{n}m\sin\left(\xi m\Delta X\right)}{A_n\Delta X}\right)^2-\frac{G}{n^4\Delta X^3}\left(\sum_{m=1}^{n}\left(\cos\left(\xi m\Delta X\right)-1\right)+\frac{\left(\sum_{m=1}^{n}m\sin\left(\xi m\Delta X\right)\right)^2}{A_n}\right)} \tag{66}$$

To see if this dispersion relation conforms to the convergence criteria of peridynamics we can again submit it to the three convergence criteria: $_m$-convergence, δ-convergence, and δm-convergence. The first is the $_m$-convergence which gives the analytical dispersion relation for the stabilized NOPD given below:

$$\begin{aligned}&\lim_{n\to\infty}2c\sqrt{\left(\frac{\sum_{m=1}^{n}m\sin\left(\xi m\frac{\delta}{n}\right)}{A_n\frac{\delta}{n}}\right)^2-\frac{G}{n^4\left(\frac{\delta}{n}\right)^3}\left(\sum_{m=1}^{n}\left(\cos\left(\xi m\frac{\delta}{n}\right)-1\right)+\frac{\left(\sum_{m=1}^{n}m\sin\left(\xi m\frac{\delta}{n}\right)\right)^2}{A_n}\right)}\\&=\frac{c}{\xi^2}\sqrt{\frac{9\left(\sin\left(\delta\xi\right)-\delta\xi\cos^2\left(\delta\xi\right)\right)}{\delta^6}+\frac{2GF\left(\delta,\xi\right)}{\delta^7}}\end{aligned} \tag{67}$$

with $F\left(\delta,\xi\right)=-2\delta^4\xi^4+3\delta^2\xi^2\cos^2\left(\delta\xi\right)+2\delta^3\xi^3\sin\left(\delta\xi\right)+3\sin^2\left(\delta\xi\right)-3\delta\xi\sin\left(2\delta\xi\right)$.

For the δ-convergence check, we have

$$\lim_{\delta\to0}2c\sqrt{\left(\frac{\sum_{m=1}^{n}m\sin\left(\xi m\frac{\delta}{n}\right)}{A_n\frac{\delta}{n}}\right)^2-\frac{G}{n^4\left(\frac{\delta}{n}\right)^3}\left(\sum_{m=1}^{n}\left(\cos\left(\xi m\frac{\delta}{n}\right)-1\right)+\frac{\left(\sum_{m=1}^{n}m\sin\left(\xi m\frac{\delta}{n}\right)\right)^2}{A_n}\right)}=c\xi \tag{68}$$

which shows that as the neighborhood radius goes to zero the classical solution is found.

Finally, the δm-convergence can be seen by letting $\delta \to 0$ in (67) :

$$\begin{aligned}
&\lim_{n\to\infty,\delta\to 0} 2c\sqrt{\left(\frac{\sum_{m=1}^{n} m\sin\left(\xi m\frac{\delta}{n}\right)}{A_n\frac{\delta}{n}}\right)^2 - \frac{G}{n^4\left(\frac{\delta}{n}\right)^3}\left(\sum_{m=1}^{n}\left(\cos\left(\xi m\frac{\delta}{n}\right)-1\right)+\frac{\left(\sum_{m=1}^{n} m\sin\left(\xi m\frac{\delta}{n}\right)\right)^2}{A_n}\right)} \\
&= \lim_{\delta\to 0}\frac{c}{\xi^2}\sqrt{\frac{9\left(\sin(\delta\xi)-\delta\xi\cos^2(\delta\xi)\right)}{\delta^6}+\frac{2GF(\delta,\xi)}{\delta^7}} \\
&= c\xi
\end{aligned}$$

(69)

which shows that the analytical dispersion converges to the classical limit as well.

To assess the effect of the stabilization, dispersion relations for both standard and stabilized NOPD are plotted in Figure 3 for $\delta = \Delta X,\ 2\Delta X,\ 3\Delta X$. It can be seen that higher G values raise the wave dispersion above the χ axis and, in doing so, mitigate zero energy mode effects. For values of G that are too large, the stabilization effect overwhelms the rest of the original wave dispersion. These large G values can have adverse effects on the model and on the MBC. These will be discussed later.

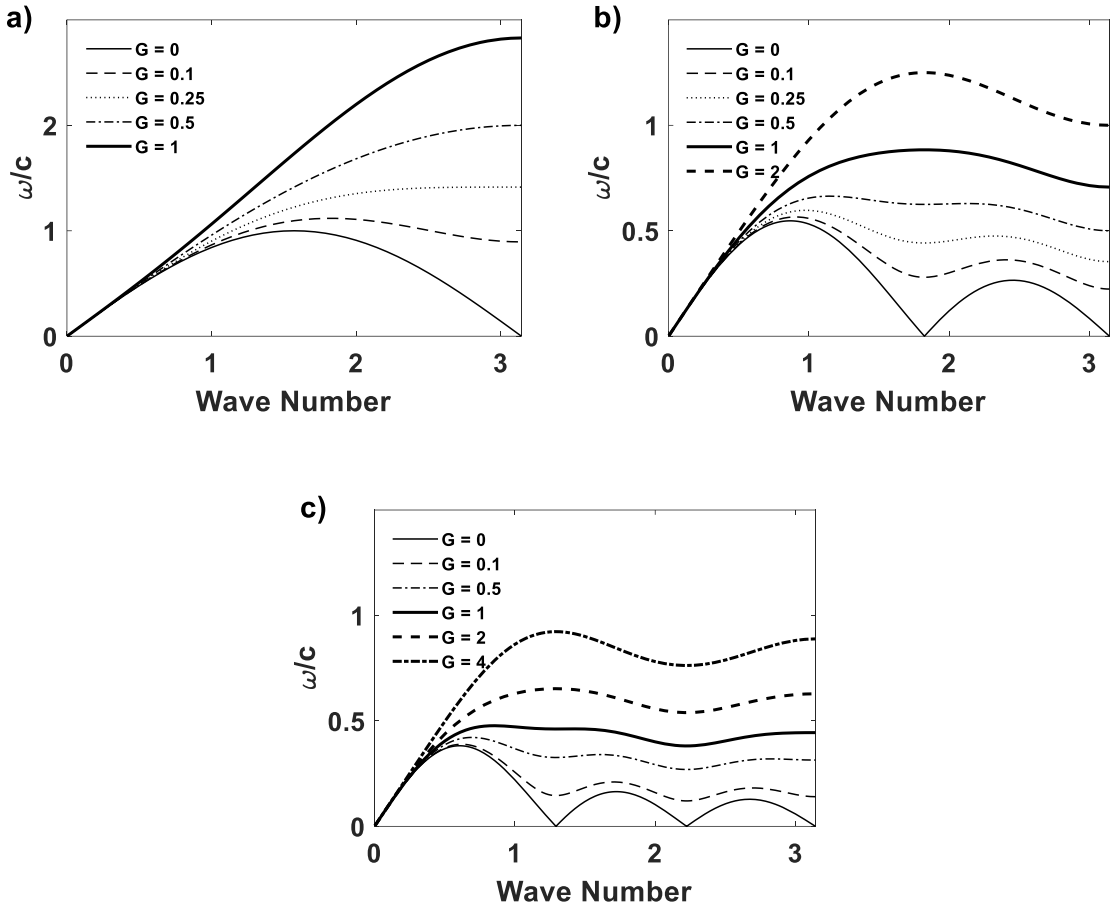

Figure 3: Dispersion relations for both standard $(G=0)$ and stabilized NOPD $(G>0)$ with correspondence material with a) $\delta=\Delta X$, b) $\delta=2\Delta X$, c) and $\delta=3\Delta X$.

3.2 Dispersion Relation of Two Dimensional Non-Ordinary Peridynamic Correspondence Material

The approach outlined in deriving the 1D dispersion relation can be further extended to the 2D case for the three versions of PD. Here we illustrate the application to NOPD. We assume a 2D configuration of a square lattice with uniform spacing of ΔX in both X and Y directions. The shape tensor is shown to be

$$\mathbf{K} = \sum_{\substack{i \\ \sqrt{i^2+j^2}\Delta X \le \delta}} \sum_{j} \begin{pmatrix} i^2 Vw\Delta X^2 & ijVw\Delta X^2 \\ ijVw\Delta X^2 & j^2 Vw\Delta X^2 \end{pmatrix} \tag{70}$$

The deformation gradient given in (16) is represented for an arbitrary neighborhood as

$$\begin{aligned} \mathbf{F} &= \mathbf{k} \bullet \mathbf{K}^{-1} \\ &= \sum_{\substack{i \\ \sqrt{i^2+j^2}\Delta X \le \delta}} \sum_{j} \begin{bmatrix} iVw\Delta X\left(i\Delta X - u_{I,J} + u_{i+I,j+J}\right) & jVw\Delta X\left(i\Delta X - u_{I,J} + u_{i+I,j+J}\right) \\ iVw\Delta X\left(j\Delta X - v_{I,J} + v_{i+I,j+J}\right) & jVw\Delta X\left(j\Delta X - v_{I,J} + v_{i+I,j+J}\right) \end{bmatrix} \bullet \mathbf{K}^{-1} . \end{aligned} \tag{71}$$

For a neighborhood of 1, Eq.(71) is simplified as

$$\mathbf{F} = \begin{bmatrix} \dfrac{2\Delta X - u_{I-1,J} + u_{I+1,J}}{2\Delta X} & \dfrac{-u_{I,J-1} + u_{I,J+1}}{2\Delta X} \\ \dfrac{-v_{I-1,J} + v_{I+1,J}}{2\Delta X} & \dfrac{2\Delta X - v_{I,J-1} + v_{I,J+1}}{2\Delta X} \end{bmatrix} . \tag{72}$$

The small strain can now be obtained as

$$\boldsymbol{\varepsilon} = \begin{bmatrix} \dfrac{-u_{I-1,J} + u_{I+1,J}}{2\Delta X} & \dfrac{-u_{I,J-1} + u_{I,J+1} - v_{I-1,J} + v_{I+1,J}}{4\Delta X} \\ \dfrac{-u_{I,J-1} + u_{I,J+1} - v_{I-1,J} + v_{I+1,J}}{4\Delta X} & \dfrac{-v_{I,J-1} + v_{I,J+1}}{2\Delta X} \end{bmatrix} . \tag{73}$$

At this point the constitutive model can be evaluated. Assuming a plane stress condition, the NOPD stress for a neighborhood of 1 is

$$\boldsymbol{\sigma} = \begin{bmatrix} \dfrac{E\left(u_{I-1,J} - u_{I+1,J} + \upsilon\left(v_{I,J-1} - v_{I,J+1}\right)\right)}{2\Delta X\left(-1+\upsilon\right)\left(1+\upsilon\right)} & -\dfrac{E\left(u_{I,J-1} - u_{I,J+1} + v_{I-1,J} - v_{I+1,J}\right)}{8\Delta X\left(1+\upsilon\right)} \\ -\dfrac{E\left(u_{I,J-1} - u_{I,J+1} + v_{I-1,J} - v_{I+1,J}\right)}{8\Delta X\left(1+\upsilon\right)} & \dfrac{E\left(\upsilon\left(u_{I-1,J} - u_{I+1,J}\right) + v_{I,J-1} - v_{I,J+1}\right)}{2\Delta X\left(-1+\upsilon\right)\left(1+\upsilon\right)} \end{bmatrix} \tag{74}$$

where υ is the Poisson's ratio. From here this stress can be used in the NOPD force density equation given in (13) and then in (1) which leads to the discretized PD equation of motion for the case of standard NOPD:

$$\rho\ddot{\mathbf{u}}_{I,J} = \int_{H_{\mathbf{X}}} \left\{ \underline{w}\boldsymbol{\sigma}\bullet\mathbf{K}^{-1}\bullet\left(\mathbf{X}'-\mathbf{X}\right) - \underline{w}'\boldsymbol{\sigma}'\bullet\mathbf{K}'^{-1}\bullet\left(\mathbf{X}-\mathbf{X}'\right) \right\} dV'$$
$$\approx \begin{bmatrix} \dfrac{E\left(u_{I-2,J} + (1-\upsilon)u_{I,J-2} + 2(\upsilon-2)u_{I,J} + (1-\upsilon)u_{I,J+2} + u_{I+2,J} + v_{I-1,J-1} - v_{I-1,J+1} - v_{I+1,J-1} + v_{I+1,J+1}\right)}{4\Delta X^3\left(\upsilon^2-1\right)} \\ \dfrac{E\left(u_{I-1,J-1} - u_{I-1,J+1} - u_{I+1,J-1} + u_{I+1,J+1} + (1-\upsilon)v_{I-2,J} + v_{I,J-2} + 2(\upsilon-2)v_{I,J} + v_{I,J+2} + (1-\upsilon)v_{I+2,J}\right)}{4\Delta X^3\left(\upsilon^2-1\right)} \end{bmatrix} \quad (75)$$

A substitution for the displacement can be made similar to that performed in (26) but now is modified for 2D:

$$\begin{bmatrix} u_{(i+I),(j+J)} \\ v_{(i+I),(j+J)} \end{bmatrix} = \begin{bmatrix} Ue^{\bar{i}\left(t\omega + (i+I)\Delta X\xi_x + (j+J)\Delta X\xi_y\right)} \\ Ve^{\bar{i}\left(t\omega + (i+I)\Delta X\xi_x + (j+J)\Delta X\xi_y\right)} \end{bmatrix} \quad (76)$$

Substitution of Eq.(76) into (75) leads to the following for 2D NOPD of a neighborhood of 1

$$\begin{bmatrix} 0 \\ 0 \end{bmatrix} = \begin{bmatrix} \dfrac{-c^2\left(\sin\left(\Delta X\xi_x\right)^2 + \sin\left(\Delta X\xi_y\right)^2 - \upsilon\sin\left(\Delta X\xi_y\right)^2\right)}{\Delta X^3\left(\upsilon^2-1\right)} + \omega^2, & -c^2\dfrac{\sin\left(\Delta X\xi_x\right)\sin\left(\Delta X\xi_y\right)}{\Delta X^3\left(\upsilon^2-1\right)} \\ -c^2\dfrac{\sin\left(\Delta X\xi_x\right)\sin\left(\Delta X\xi_y\right)}{\Delta X^3\left(\upsilon^2-1\right)}, & \dfrac{-c^2\left(\sin\left(\Delta X\xi_x\right)^2 + \sin\left(\Delta X\xi_y\right)^2 - \upsilon\sin\left(\Delta X\xi_x\right)^2\right)}{\Delta X^3\left(\upsilon^2-1\right)} + \omega^2 \end{bmatrix} \begin{bmatrix} U \\ V \end{bmatrix} \quad (77)$$

in which the dispersion relation is to be solved by enforcing the determinant of the coefficient matrix to be zero. To relate the dispersion to the 2D wave, we introduce α as the angle of incidence such that

$$\begin{bmatrix} \xi_x \\ \xi_y \end{bmatrix} = \begin{bmatrix} \xi\cos\alpha \\ \xi\sin\alpha \end{bmatrix} \tag{78}$$

This gives us the following general 2D dispersion relation for an arbitrary wave number and incident angle for $\Delta X = 1$ and $G = 0$.

$$\omega = c\sqrt{\frac{2}{15}}\sqrt{\begin{matrix} 7\sin\left[\zeta\cos\left[\alpha\right]\right]^2 + 7\sin\left[\zeta\sin\left[\alpha\right]\right]^2 \\ \pm\sqrt{\sin\left[\zeta\cos\left[\alpha\right]\right]^4 + 62\sin\left[\zeta\cos\left[\alpha\right]\right]^2\sin\left[\zeta\sin\left[\alpha\right]\right]^2 + \sin\left[\zeta\sin\left[\alpha\right]\right]^4} \end{matrix}} \tag{79}$$

If $\alpha = 0$ we obtain the following dispersion relation for a unidirectional wave for local neighbors in 2D NOPD:

$$\omega = \left[\frac{c\sqrt{16\sin^2\xi}}{\sqrt{15}}, \frac{c\sqrt{2\sin^2\xi}}{\sqrt{5}}\right]. \tag{80}$$

Following the same process, the wave dispersions can be derived for larger neighborhoods. For a 2D domain, the neighborhood can be defined as $\delta = \Delta X\sqrt{i^2 + j^2}$ where i and j are the number of nodes in the x and y direction respectively. For stabilized NOPD, the dispersion relation can be derived using the same approach. Eqs.(81), (82), and (83) provide the wave dispersion solutions for $\Delta X = 1$ for neighborhood sizes of $\delta = \Delta X$, $2\Delta X$, $3\Delta X$ and $\alpha = 0$ and are plotted in Figure 12. Note that the corresponding dispersion relations for the standard NOPD can be obtained by letting $G = 0$.

$$\omega_{\delta=1} = 2\sqrt{\frac{2}{15\pi}}\sqrt{\left(15G + 4\pi - 15G\cos\xi + 4\pi\cos\xi\right)\sin^2\left(\frac{\xi}{2}\right)} \tag{81}$$

$$\omega_{\delta=2}=\frac{1}{7\sqrt{30\pi}}\sqrt{\left(\begin{array}{l}29\left(35G+64\pi\right)+5\left(-77G+576\pi\right)\cos\xi+\\40\left(-7G+32\pi\right)\cos\left(2\xi\right)+2\left(-175G+128\pi\right)\cos\left(3\xi\right)\end{array}\right)\sin^2\left(\frac{\xi}{2}\right)} \tag{82}$$

$$\omega_{\delta=3}=\frac{1}{153\sqrt{35\pi}}\left(\sqrt{\left(\begin{array}{l}502\left(340G+567\pi\right)+10\left(4148G+49329\pi\right)\cos\xi+\\192\left(-425G+1701\pi\right)\cos\left(2\xi\right)+3\left(-30260G+52353\pi\right)\cos\left(3\xi\right)+\\2\left(-9860G+22113\pi\right)\cos\left(4\xi\right)+\left(-20060G+5103\pi\right)\cos\left(5\xi\right)\end{array}\right)\sin^2\left(\frac{\xi}{2}\right)}\right) \tag{83}$$

For the selected wave dispersions shown in Figure 4 it can be seen that the stabilization constant G has a similar effect in 2D as it does in 1D in that the zero energy modes are dissipated with higher values of *G*. Variances occur in the form of the wave dispersion between 1D and 2D in that the neighborhood of $\delta=3\Delta X$ does not bring an additional zero energy mode as in 1D. This can be attributed to the more interconnected nature of the 2D constitutive model.

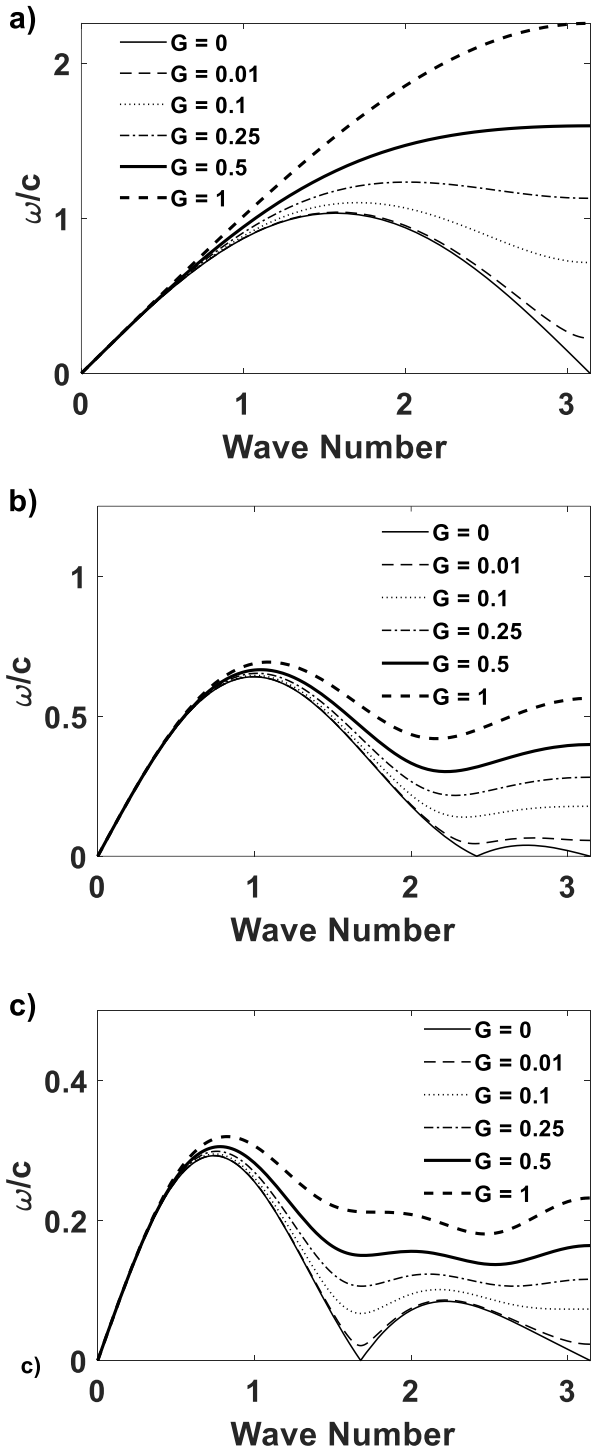

Figure 4: 2D SNOPD correspondence material wave dispersion relations for various selection of *G* for a) $\delta = \Delta X$ **, b)** $\delta = 2\Delta X$ **, and c)** $\delta = 3\Delta X$ **respectively.**

CHAPTER 4

MATCHING BOUNDARY CONDITIONS FOR PERIDYNAMICS

4.1 Matching Boundary Conditions

The matching boundary condition [26] for 1D has been expressed as

$$\sum_{j=0}^{N} c_j \dot{u}_j - \sum_{j=0}^{N} b_j u_j = 0 \tag{84}$$

in which u_j is the displacement of the j-th particle, the index j is prescribed in such a way that $j=0$ corresponds to the first particle within the boundary domain (Figure 5). The basic idea of (84) is then to use the information of the interior nodes and suitable coefficients of c_j and b_j to prescribe the degree of freedoms of the boundary node(s) and their time derivatives to accomplish a non-reflective boundary.

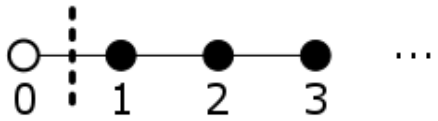

Figure 5: Node numbering of the 1D boundary and internal domains where the open node indicates a boundary node and the filled nodes are internal nodes.

Equation (26) can be substituted into (84) to get

$$\bar{i}\,\omega(\xi)\sum_{j=0}^{N} c_j e^{\bar{i}j\xi\Delta X} - \sum_{j=0}^{N} b_j e^{\bar{i}j\xi\Delta X} = \Delta(\xi) \tag{85}$$

in which $\Delta(\xi)$ is a residual. Ideally, $\Delta(\xi)=0$ implies a perfectly non-reflective interface since it indicates that Eq. (84) automatically satisfies the dispersion relation for a given PD formulation. However, $\Delta(\xi)$ is generally nonzero. This condition can be relaxed by enforcing $\Delta(\xi)$ and its derivatives to be zero at selected wave numbers of interest. In this work, we expand (85) around $\xi=0$ to focus on long wave limit to obtain

$$\bar{i}\,\omega(\xi)=\sum_{n=0}^{\infty}a_n\left(\bar{i}\,\xi\right)^n \qquad\qquad e^{\bar{i}j\xi\Delta X}=\sum_{n=0}^{\infty}\frac{\left(j\Delta X\right)^n}{n!}\left(\bar{i}\,\xi\right)^n=\sum_{n=0}^{\infty}h_{nj}\left(\bar{i}\,\xi\right)^n \tag{86}$$

The unknown coefficients can be solved by enforcing

$$\left.\frac{d^n\Delta(\xi)}{d\xi^n}\right|_{\xi=0}=0,\ \forall\ n=0,1,2,3,...,2N \tag{87}$$

We term the corresponding matching boundary condition, MBC*N*. Eq. (87) yields a system of equations for the c_j and b_j coefficients to be solved, given in matrix form as

$$\begin{bmatrix} e_1^T & z^T \\ AH & -H \end{bmatrix}\begin{bmatrix} C \\ B \end{bmatrix}=\begin{bmatrix} e_1^T \\ z^T \end{bmatrix} \tag{88}$$

in which

$$e_1=\begin{bmatrix}1\\0\\\vdots\\0\end{bmatrix},\quad z=\begin{bmatrix}0\\0\\\vdots\\0\end{bmatrix},\quad \mathbf{C}=\begin{bmatrix}c_0\\c_1\\\vdots\\c_N\end{bmatrix},\quad \mathbf{B}=\begin{bmatrix}b_0\\b_1\\\vdots\\b_N\end{bmatrix} \tag{89}$$

$$A=\begin{bmatrix} a_0 & 0 & \cdots & 0 \\ a_1 & a_0 & \ddots & \vdots \\ \vdots & \vdots & \ddots & 0 \\ a_{2N} & a_{2N-1} & \cdots & a_0 \end{bmatrix},\ H=\begin{bmatrix} h_{00} & h_{01} & \cdots & h_{0N} \\ h_{10} & h_{11} & \ddots & h_{1N} \\ \vdots & \vdots & \ddots & \vdots \\ h_{2N0} & h_{2N1} & \cdots & h_{2NN} \end{bmatrix} \tag{90}$$

As an example we let $N = 1$ and use (30), (39), and (51) with a horizon radius of 1. It can be shown that

$$A=\begin{bmatrix} 0 & 0 & 0 \\ a_1 & 0 & 0 \\ 0 & a_1 & 0 \end{bmatrix},\ H=\begin{bmatrix} 1 & 1 \\ 0 & \Delta X \\ 0 & \dfrac{\Delta X^2}{2} \end{bmatrix} \tag{91}$$

for the BBPD, OPD, and NOPD dispersion relations that only include the nearest neighbor. This gives us the matrix equation of

$$\begin{bmatrix} 1 & 0 & 0 & 0 \\ 0 & 0 & -1 & -1 \\ a_1 & a_1 & 0 & -\Delta X \\ 0 & a_1\Delta X & 0 & \dfrac{-\Delta X^2}{2} \end{bmatrix}\begin{bmatrix} c_0 \\ c_1 \\ b_0 \\ b_1 \end{bmatrix}=\begin{bmatrix} 1 \\ 0 \\ 0 \\ 0 \end{bmatrix} \tag{92}$$

which gives the solution for the coefficients as $c_0 = c_1 = 1,\ b_0 = -b_1 = \dfrac{-2a_1}{\Delta X}$. These coefficients also describe the first order solution for other dispersion relations [27] and give another example of peridynamics' "equivalence" to other computational models when the horizon is limited to local neighbors. For an arbitrary neighborhood we can use the dispersion relation for an arbitrary radius for BBPD (29), OPD (38), and NOPD (51) in conjunction with (85). Utilizing the arbitrary horizon residual functions with (87) to solve for a first order solution for the arbitrary neighborhood gives

the following results in (94) with the expressions for the derivatives of the residual function to show the solution process for the first order solution with $\Delta X = 1$.

$$\left.\frac{d^n \Delta(\xi)}{d\xi^n}\right|_{\xi=0} = 0, \text{ n} = 0,1,2$$
$$\text{n} = 0 \;\rightarrow\; -b_0 - b_1 = 0 \tag{93}$$
$$\text{n} = 1 \;\rightarrow\; b_1 = c(1 + c_1)$$
$$\text{n} = 2 \;\rightarrow\; b_1 = c(2c_1)$$

$$\left.\begin{array}{l} \text{BBPD: } c_0 = c_1 = 1,\ b_0 = -b_1 = -2 \\ \text{OPD: } c_0 = c_1 = 1,\ b_0 = -b_1 = -2 \\ \text{NOPD: } c_0 = c_1 = 1,\ b_0 = -b_1 = -2 \end{array}\right\} \forall \delta \tag{94}$$

From (94) it can be seen that the three PD version have the same MBC, coefficients for a first order MBC. Looking to understand larger neighborhoods and higher order MBC the a_n coefficients can be represented symbolically. BBPD is difficult to represent arbitrarily due to the discrete nature of the W_k terms, though it is possible to represent OPD and NOPD a_n coefficients for an arbitrary horizon radius.

It can be seen that Table 1 details the a_n coefficients for BBPD up to a horizon radius of 3 with (95) and (96) representing the arbitrary a_n values for OPD and NOPD respectively. Table 2 contains the MBC coefficients of higher orders of MBC with arbitrary a_n values.

Table 1: 1st order MBC coefficients for BBPD, OPD, and NOPD for horizon radius 1-3

BBPD

δ	a_1	a_3	a_5	a_7
$1\,\Delta X$	c	$\frac{c\Delta X^2}{24}$	$\frac{c\Delta X^4}{1920}$	$\frac{c\Delta X^6}{322560}$
$2\,\Delta X$	c	$\frac{5c\Delta X^2}{48}$	$\frac{49c\Delta X^4}{7680}$	$\frac{73c\Delta X^6}{516096}$
$3\,\Delta X$	c	$\frac{5c\Delta X^2}{24}$	$\frac{449c\Delta X^4}{17280}$	$\frac{796c\Delta X^6}{580608}$

The a_n values for OPD can be expressed for an arbitrary neighborhood radius *n* as

$$\begin{aligned} a_1 &= c \\ a_3 &= \frac{c}{120}(\Delta X)^2\left(-1+3n+3n^2\right) \\ a_5 &= \frac{c}{560\cdot 5!}(\Delta X)^4\left(11-26n-7n^2+38n^3+19n^4\right) \\ a_7 &= \frac{c}{4800\cdot 7!}(\Delta X)^6\left(-87+183n+74n^2-189n^3-22n^4+87n^5+29n^6\right) \end{aligned} \tag{95}$$

The a_n values for NOPD can be expressed for an arbitrary neighborhood radius *n* as

$$\begin{aligned} a_1 &= c \\ a_3 &= \frac{c}{30}(\Delta X)^2\left(-1+3n+3n^2\right) \\ a_5 &= \frac{c}{840}(\Delta X)^4\left(1-3n+6n^3+3n^4\right) \\ a_7 &= \frac{c}{15\cdot 7!}(\Delta X)^6\left(-3+9n-n^2-15n^3+5n^4+15n^5+5n^6\right) \end{aligned} \tag{96}$$

For stabilized NOPD, we have

$$
\begin{aligned}
a_1 &= c \\
a_3 &= \frac{c\left(-1+3n\left(1+n\right)\right)\Delta X\left(G\left(1+n\right)\left(1+2n\right)+4n^3\Delta X\right)}{120n^3} \\
a_5 &= \frac{c\Delta X^2\begin{pmatrix} -7G^2\left(-1+10n^2+15n^3+6n^4\right)^2 \\ +8G\left(-1+n\right)n^3\left(1+n\right)\left(2+n\right)\left(-1+2n\right)\left(1+2n\right)\left(3+2n\right)\Delta X \\ +240n^6\left(1+3n\left(1+n\right)\left(-1+n+n^2\right)\right)\Delta X^2 \end{pmatrix}}{201600n^6} \\
a_7 &= \frac{c\Delta X^3\begin{pmatrix} 60G^2n^3\left(1+n\right)^2\left(1+2n\right)^2\left(1+n\left(1+n\right)\left(1+n\left(1+n\right)\left(-23+33n\left(1+n\right)\right)\right)\right)\Delta X \\ -56Gn^6\left(1+n\right)\left(1+2n\right)\left(-9+n\left(1+n\right)\left(21+n\left(1+n\right)\left(-38+43n\left(1+n\right)\right)\right)\right)\Delta X^2 \\ +960n^9\left(-3+n\left(1+n\right)\left(9+5\left(-1+n\right)n\left(1+n\right)\left(2+n\right)\right)\right)\Delta X^3 \\ -21G^3\left(-1+10n^2+15n^3+6n^4\right)^3 \end{pmatrix}}{72576000n^9}
\end{aligned}
\tag{97}
$$

Table 2: Coefficients for arbitrary MBC coefficients for order 1-4

Order	c_0	c_1	c_2	c_3	c_4	b_0	b_1	b_2	b_3	b_4
1	1	1				$\frac{-2a_1}{\Delta X}$	$\frac{2a_1}{\Delta X}$			
2	1	I_1	1			I_2	0	$-I_2$		
3	1	I_3	I_3	1		I_4	I_5	$-I_5$	$-I_4$	
4	1	I_6	I_7	I_6	1	I_8	I_9	0	$-I_9$	$-I_8$

Note:

$$I_1=\frac{4\left(a_1\Delta X^2+3a_3\right)}{a_1\Delta X^2-6a_3}\ ,\ I_2=-\frac{3a_1^2\Delta X}{a_1\Delta X^2-6a_3}\ ,\ I_3=\frac{3\left(3a_1\Delta X^4+40\left(a_3\Delta X^2+a_5\right)\right)}{a_1\Delta X^4-120a_5},$$

$$I_4=\frac{720\left(a_3{}^2-a_1a_5\right)+120a_1a_3\Delta X^2+11a_1^2\Delta X^4}{360a_5\Delta X-3a_1\Delta X^5},$$

$$I_5=\frac{3\left(-240a_3^2+240a_1a_5+40a_1a_3\Delta X^2+3a_1{}^2\Delta X^4\right)}{\Delta X\left(120a_5-a_1\Delta X^4\right)},$$

$$I_6=\frac{8\begin{pmatrix}12600\left(-a_5^2+a_3a_7\right)+1050\left(-a_3a_5+a_1a_7\right)\Delta X^2+\\35\left(21a_3^2-19a_1a_5\right)\Delta X^4-55a_1a_3\Delta X^6-4a_1^2\Delta X^8\end{pmatrix}}{\begin{pmatrix}25200\left(a_5^2-a_3a_7\right)+4200\left(-a_3a_5+a_1a_7\right)\Delta X^2+\\35\left(3a_3^2+8a_1a_5\right)\Delta X^4+5a_1a_3\Delta X^6-2a_1^2\Delta X^8\end{pmatrix}},$$

$$I_7=\frac{6\begin{pmatrix}25200\left(a_5^2-a_3a_7\right)+4200\left(a_3a_5-a_1a_7\right)\Delta X^2+\\315\left(7a_3^2-8a_1a_5\right)\Delta X^4-205a_1a_3\Delta X^6-12a_1^2\Delta X^8\end{pmatrix}}{\begin{pmatrix}25200\left(a_5^2-a_3a_7\right)+4200\left(-a_3a_5+a_1a_7\right)\Delta X^2+\\35\left(3a_3^2+8a_1a_5\right)\Delta X^4+5a_1a_3\Delta X^6-2a_1^2\Delta X^8\end{pmatrix}},$$

$$I_8=\frac{5\Delta X\left(-7560\left(a_3^3-2a_1a_3a_5+a_1^2a_7\right)+63a_1^2a_3\Delta X^4+5a_1^3\Delta X^6\right)}{3\begin{pmatrix}25200\left(a_5^2-a_3a_7\right)+4200\left(-a_3a_5+a_1a_7\right)\Delta X^2+\\35\left(3a_3^2+8a_1a_5\right)\Delta X^4+5a_1a_3\Delta X^6-2a_1^2\Delta X^8\end{pmatrix}},$$

$$I_9=\frac{40\Delta X\left(1890\left(a_3^3-2a_1a_3a_5+a_1^2a_7\right)+945a_1\left(-a_3^2+a_1a_5\right)\Delta X^2+63a_1^2a_3\Delta X^4+4a_1^2\Delta X^6\right)}{3\begin{pmatrix}25200\left(a_5^2-a_3a_7\right)+4200\left(-a_3a_5+a_1a_7\right)\Delta X^2+\\35\left(3a_3^2+8a_1a_5\right)\Delta X^4+5a_1a_3\Delta X^6-2a_1^2\Delta X^8\end{pmatrix}}$$

With the expressions above, it can be shown that the MBC coefficients are singular when $N\geq 2n$ where N is the MBC approximation order in the case of standard NOPD ($G=0$). This can be generally considered as an admissible condition for the neighbor size in standard NOPD for implementing MBC. For instance, it can be verified that that for a local neighborhood case ($n=1$), the coefficients for higher order MBC are all singular.

For larger neighborhoods ($n>1$ and $n<2N$) solutions do exist, but none of them are found to be stable solutions. A case of MBC2 with $\delta=2\Delta X$ and $\Delta X=1$ yields $c_0=c_2=1,\ c_1=-\frac{9}{2}c,\ b_0=-b_2=\frac{5}{4}c,\ b_1=0$. This boundary condition leads to unstable results due to the negative coefficient c_1. This issue is improved in the stabilized NOPD due to the stabilization parameter G. For an arbitrary horizon radius, the ranges over which G values lead to stable solutions for the stabilized NOPD can be obtained by enforcing the reflection coefficient [17] to be less than or equal to 1. It can then be shown that arbitrary values of G can be used in the case of MBC1 as long as $G\geq 0$ for any neighborhood size. For MBC2, the following conditions have to be satisfied:

$$\begin{aligned} &0<G<1 && \text{for } n=1\\ &0<G<\frac{208}{85} && \text{for } n=2\\ &0<G<\frac{405}{98} && \text{for } n=3 \end{aligned} \tag{98}$$

For MBC3, we have

$$\begin{aligned} &0<G<\frac{2}{3} && \text{for } n=1\\ &\frac{5584-80\sqrt{433}}{4335}<G<\frac{5584+80\sqrt{433}}{4335} && \text{for } n=2\\ &\frac{11583-27\sqrt{2937}}{4802}<G<\frac{11583+27\sqrt{2937}}{4802} && \text{for } n=3 \end{aligned} \tag{99}$$

It should be noted that two different types of stability for MBC are pertinent. The first type is reflected in the negative MBC c_i coefficients that cause the simulation to become unstable within a few time steps of MBC implementation regardless of the time step size. The second

instability is encountered when the G value selected is beyond the bounds of the acceptable range for a reflection coefficient that is less than one. This instability is not immediately catastrophic. It allows the successive amplification of the initial wave that will eventually overwhelm the simulation. In this case, as the bounds of acceptable G values are approached smaller time steps are required as the MBC coefficients are approaching singularities. Continued discussion and plots of the reflection coefficients are given in Section 4.7.

4.2 NMBC for Bond-Based and Ordinary Peridynamics

We consider wave propagation in a 1D elastic bar. For numerical discretization, the center region of length of 500 is discretized by 500 uniformly spaced nodes. Here we first employ the NOPD correspondence material model. For the implementation of MBC, a single node is prescribed at the left and right sides of the interfacial boundary (Figure 5). The initial nodal spacing is $\Delta X = 1$ and cross-sectional area $A = 1$. The material properties are given as mass density $\rho = 1$, Young's modulus $E = 57.1464$, and Poisson's ratio $\upsilon = 0.25$. In addition to the NOPD correspondence material model, we also compare with the MBC implementation for molecular dynamics. A 1D monoatomic chain system is constructed for this purpose. The governing equation and wave dispersion for the MD system is given as

$$m\ddot{u}_i = k\left(u_{i-1} - 2u_i + u_{i+1}\right) \qquad \omega = 2\left|\sin\left(\zeta/2\right)\right| \tag{100}$$

where $m = \rho A \Delta X$ is the mass of the atom, $k = EA/\Delta X$ is the spring constant between atoms.

The elastic bar is subjected to a wave profile (Figure 6) that is imposed for nodes located at $250 - 2\delta \le X \le 250 + 2\delta$ in the following form

$$u(X,t)=\frac{\varepsilon_0}{4}\left(1-\sin\left(\frac{t\pi}{t_{\max}}+\frac{\pi}{2}\right)\right) \quad . \tag{101}$$

with $\varepsilon_0=0.01$, $t_{\max}=12.56$.

The case of MBC1 with $\delta=\Delta X=1$ is tested and given as

$$\begin{array}{ll}\text{Left Interface} & \dot{u}_0=-\dot{u}_1+c\left(-2u_0+2u_1\right)\\ \text{Right Interface} & \dot{u}_{501}=-\dot{u}_{500}+c\left(-2u_{501}+2u_{500}\right)\end{array} \quad . \tag{102}$$

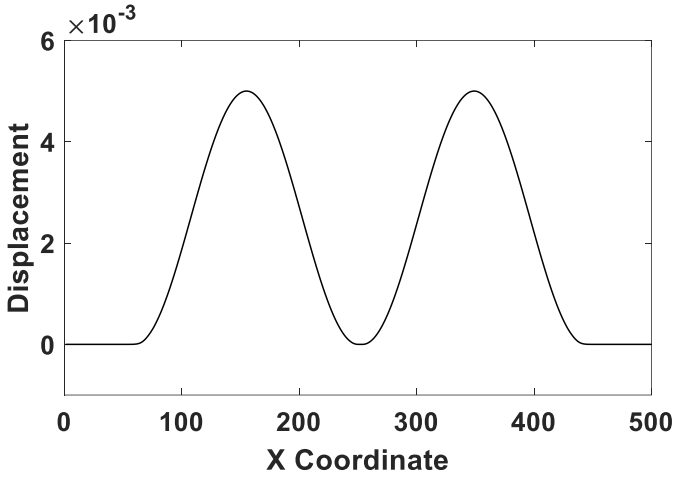

Figure 6: Wave profile of the BBPD, OPD, and NOPD 1D simulations

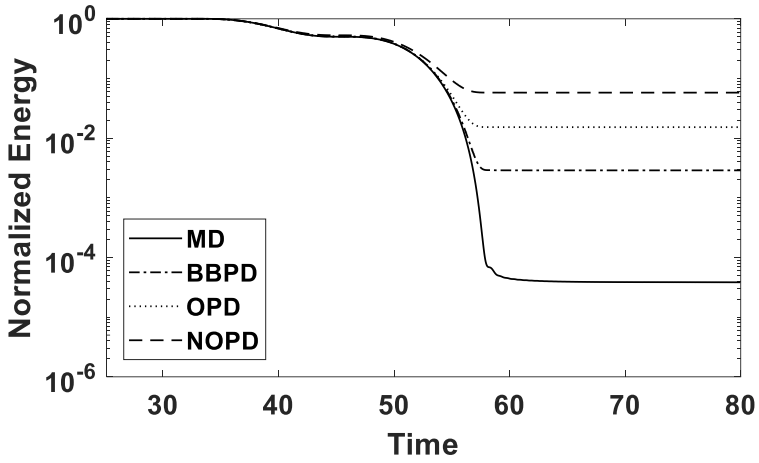

Figure 7: Comparative results of the BBPD, OPD, NOPD, and MD simulations with a first order matching boundary condition normalizing energy while the wave is in equilibrium

Figure 7 provides a comparison on the time history of normalized system energy obtained from the three PD formulations and MD. The efficiency of MBC can be quantified by the reduction in the total system energy. It can be seen that less than 0.3% of the total energy remained in the system for the cases of BBPD and much less for MD. Furthermore, MD results follow along closely with the BBPD results until the wave has passed. The discrepancy between BBPD and MD as shown in Figure 7 are due to the surface correction factor applied in BBPD, i.e., the volume for the edge node is adjusted in BBPD. This adjustment means that the edge node in BBPD is no longer equivalent to the corresponding node in MD.

4.2.1 Edge Effects and NMBC

The differences between BBPD and OPD, as shown in Figure 7, are attributed to the nonlocal nature of the PD formulation that is manifested by the numerical implementation on the edge node (indexed by "1" in Figure 5) in the case of OPD. Unlike the neighbors of the interior node that have full neighbors themselves, the edge node has the boundary node as its neighbor and

the boundary node only has a single neighbor on one side which is the edge node itself. For instance: the material and spatial coordinates for node 0 are given as $R_0 = \{-\Delta X\}$ and $r_0 = \{\Delta X - u_0 + u_1\}$. The edge effect is demonstrated for the local neighbors in OPD and then extended to an arbitrary neighborhood in NOPD. The non-local MBC are applicable and required for both OPD and NOPD.

It can be shown that the OPD parameters for the boundary node (indexed by "0" in Figure 5) are

$$\begin{aligned} m_0 &= V\Delta X^2 w & \underline{e}_0 &= -\Delta X + |\Delta X - u_0 + u_1| \\ \theta_0 &= \frac{-\Delta X + |\Delta X - u_0 + u_1|}{\Delta X} & \underline{t}_0 &= \frac{6C\left(-\Delta X + |\Delta X - u_0 + u_1|\right)}{V\Delta X^2} \end{aligned} \cdot \tag{103}$$

Based on Eq.(103), the governing equation for node 1 is given as

$$\rho(x)\ddot{u}_1(x) = \frac{E\left(3u_0 - 5u_1 + 2u_2\right)}{2\Delta X^2} \ . \tag{104}$$

The fact that Eq.(104) is different from the that of an interior node suggests that the MBC based on the wave dispersion derived in (39) will be less effective for the edge node. To provide solution to this issue, we recast Eq. (84) in the following form by adding one extra node at the interface as shown in Figure 8:

$$\sum_{j=0}^{N} c_j \dot{u}_{j-M} - \sum_{j=0}^{N} b_j u_{j-M} = 0 \quad \text{for} \quad M = 0,\ 1 \ . \tag{105}$$

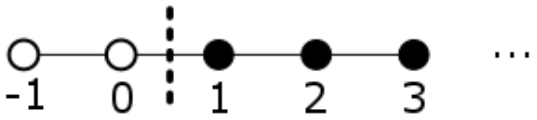

Figure 8: The revised NMBC for PD: An extra node, labeled as -1, is added to the left boundary domain for a local neighbor interaction

Equation (105) is termed a non-local matching boundary condition (NMBC) as it takes into consideration the non-local effect of peridynamics. This creates the two sets of equations that are employed to solve the coefficients but now the boundary conditions can be solved for all the boundary nodes. With (105), (85) can be recast as

$$\bar{i}\,\omega(\xi)\sum_{j=0}^{N} c_j e^{\bar{i}(j-M)\xi\Delta X} - \sum_{j=0}^{N} b_j e^{\bar{i}(j-M)\xi\Delta X} = \Delta_M(\xi)\ . \tag{106}$$

Note that the wave substitution used in (106) is

$$u_j = e^{\bar{i}(\omega t+(j-M)\xi\Delta X)}\ . \tag{107}$$

Eq. (106) can be used with (86) and (87) to construct a system of equations for each boundary node M:

$$\begin{bmatrix} e_1^T & z^T \\ AH & -H \end{bmatrix}\begin{bmatrix} C_{(M)} \\ B_{(M)} \end{bmatrix} = \begin{bmatrix} e_1^T \\ z^T \end{bmatrix}\ . \tag{108}$$

In (108) we see that the coefficient matrix remains the same for the different choices of *M*. Therefore:

$$\begin{aligned} c_0^{(0)} &= c_0^{(1)} = \ldots = c_0^{(M)} \quad & b_0^{(0)} &= b_0^{(1)} = \ldots = b_0^{(M)} \\ c_1^{(0)} &= c_1^{(1)} = \ldots = c_1^{(M)} \quad & b_1^{(0)} &= b_1^{(1)} = \ldots = b_1^{(M)} \\ &\vdots & &\vdots \\ c_N^{(0)} &= c_N^{(1)} = \ldots = c_N^{(M)} \quad & b_N^{(0)} &= b_N^{(1)} = \ldots = b_N^{(M)} \end{aligned} \quad . \tag{109}$$

With this, the OPD simulation is run again with the proposed NMBC based on Eq. (105) and $M = 0,\ 1$ for a NMBC at both ends of the internal domain. Figure 9 provides a comparison among MD, BB, and OPD with the NMBC now labeled as OPD+. It can be seen that, with the inclusion of an additional boundary node, the NMBC leads to a much more effective non-reflective boundary condition, evidenced by a remaining energy of ~0.024% in the local OPD results.

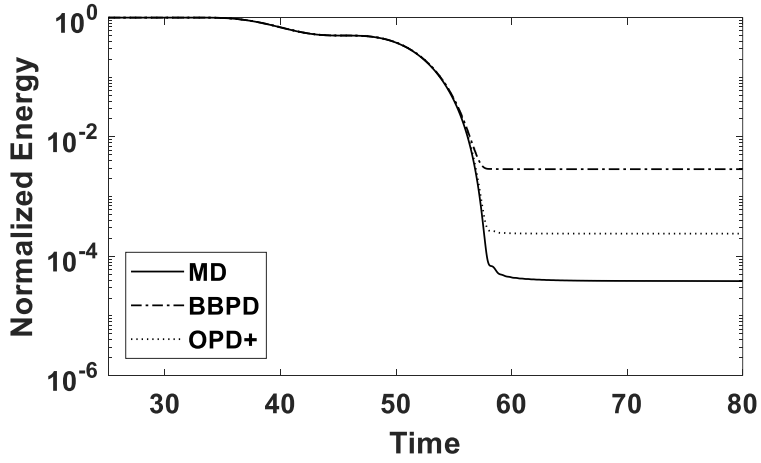

Figure 9: Comparative results of the BB, OPD+, and MD simulations with a first order MBC

4.3 NMBC for Non-Ordinary Peridynamics with Correspondence Material Model

The NMBC approach described in 4.2.1 can be extended to treat the edge effect in the case of NOPD. This edge effect can be demonstrated by first employing the original MBC as given in (84) through (88). The performance of the first order MBC is shown in Figure 7, in which it is seen that the implementation is not effective in that at least 5.7% energy still remains in the system. In Figure 10 the effects of larger horizon radii using an MBC boundary condition are shown. In this figure the size of the boundary domain is set equal to the horizon radius.

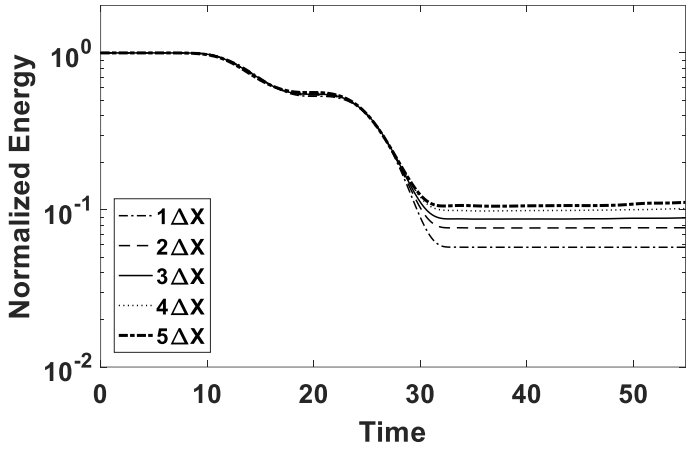

Figure 10: System energy remaining for NOPD with standard MBC with minimally required PD boundary regions

Similar to the case of OPD, the edge node in NOPD doesn't have a boundary node whose neighborhood is full which again gives us that $R_0 = \{-\Delta X\}$ and $r_0 = \{\Delta X - u_0 + u_1\}$ and can be used to determine the deformation gradient, shape tensor, strain, and stress as

$$\begin{aligned} F_0 &= \frac{\Delta X - u_0 + u_1}{\Delta X} & B_0 &= \frac{1}{Vw\Delta X^2} \\ \varepsilon_0 &= \frac{-u_0 + u_1}{\Delta X} & \sigma_0 &= \frac{E\left(-u_0 + u_1\right)}{\Delta X} \end{aligned} . \tag{110}$$

It can then be shown that the discrete equation of motion at the boundary node (node 1) is given as

$$\rho\ddot{u}_1(\mathrm{X}) = \frac{E(3u_0 - 4u_2 + u_3)}{4\Delta X^2} \tag{111}$$

which is different from the local equation of motion derived for use in MBC for NOPD in Eq. (49). This then produces a different condition in which the MBC is not properly defined thus creating inefficient wave absorption at the boundary. Thus we demonstrate the edge effect for NOPD.

Since it has been shown through Eqs. (106) to (109) that the MBC coefficients do not vary when adding nodes into the boundary domain the MBC for NOPD, and other forms of PD as well, can be written generally as

$$\sum_{j=0}^{N} c_j \dot{u}_{j-M} - \sum_{j=0}^{N} b_j u_{j-M} = 0 \quad \text{for} \quad M = 0,\ ...,\ 2n-2,\ 2n-1 \tag{112}$$

As can be seen, a new index set *M* is introduced to describe a boundary domain that is two times larger than the neighborhood horizon radii. Having this will allow the edge node to have a family of nodes whose families are also full. This revised MBC is called a nonlocal MBC (NMBC) and was also demonstrated in part in [2] for the case in which 1D bond based force density function was employed. Results from NMBC with different choices of horizon size are shown in Figure 11. The NMBC coefficients can be solved using the same approach as outlined before, and it can be shown that the NMBC coefficients are independent of *M*. It is seen that the energy remaining in NOPD is about 0.09% for the local case (horizon size of ΔX), which is

near the performance of the MD results and an 2 orders of magnitude better than the previously shown MBC in Figure 10.

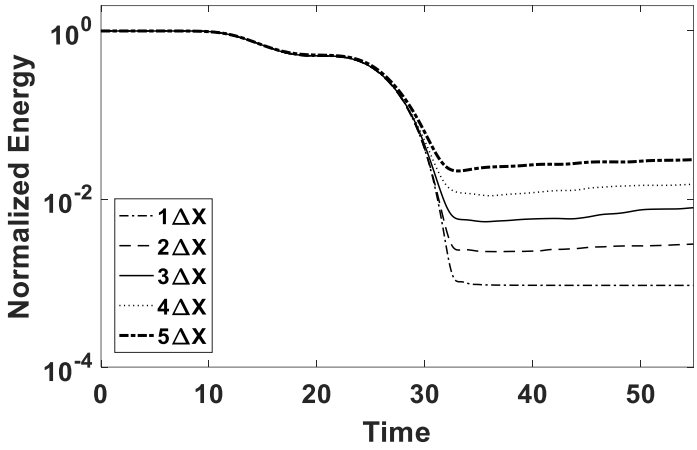

Figure 11: Energy absorption of NMBC for NOPD of different horizon radii

Table 3: System energy remaining at Time=54.88 for NOPD with MBC1 from Figure 11

Horizon	$1\,\Delta X$	$2\,\Delta X$	$3\,\Delta X$	$4\,\Delta X$	$5\,\Delta X$
Energy Remaining	9×10^{-4}	2.9×10^{-3}	7.9×10^{-3}	1.5×10^{-2}	2.92×10^{-2}
'Ideal' Energy	8.8×10^{-8}	8×10^{-6}	3.8×10^{-4}	1.3×10^{-3}	2.8×10^{-3}

Table 3 the total energy remaining for the NOPD system is given for different horizon radii. Each result is also accompanied by an 'ideal' solution that is obtained by doubling the internal domain from 500 nodes to 1000 nodes but only recording the energy between nodes 250 to 750. With this approach, we are able to capture a boundary transition that should be free of numerical boundary effects and sets a model baseline for assessing the effectivity of the NMBC. Effectivity is given as the normalized amount of total energy remaining against peak system energy in the system after absorption of the wave by the MBC.

For NOPD there is a difference of several order of magnitude in the energy remaining between the ideal and NMBC. To evaluate this discrepancy a power spectral density (PSD) plot is generated for the displacement profile at $t = 12.56$ and shown in Figure 12.

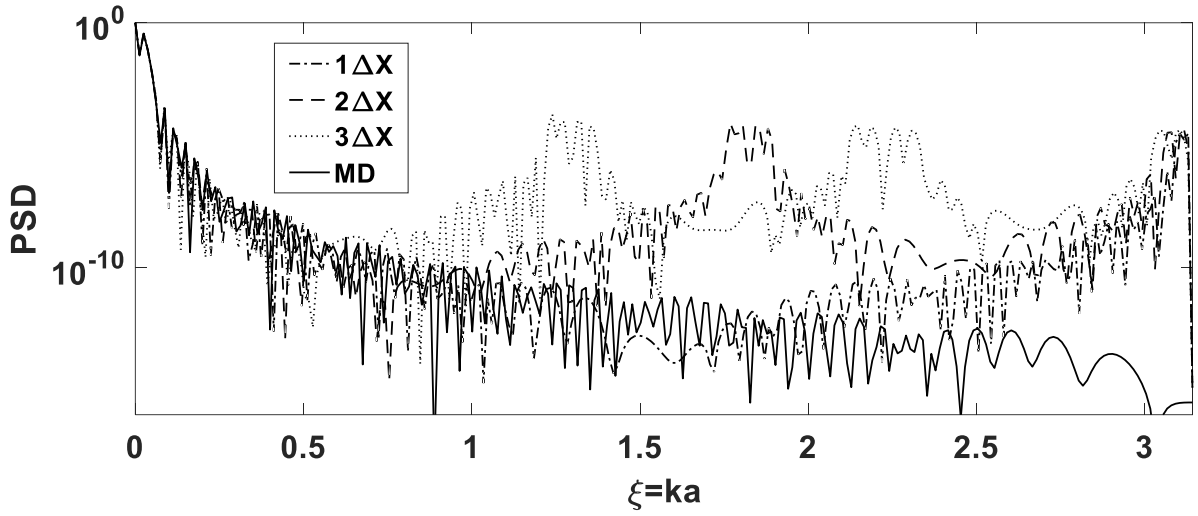

Figure 12: PSDs for NOPD horizon radii of 1 through 3 and MD for the displacement prescribed in (101).

Here, Figure 12 confirms that the solution is dominated by the long wave as majority of the energy is weighted towards a wave number of zero. However, in NOPD it is seen that as the neighborhood size increases particular wave numbers are excited within the PSD as a result of the zero energy modes that are inherent to the correspondence material model as discussed in [28]. A correspondence material model with radius of ΔX has a minor peak present at the wave number π with higher horizon radii gaining additional numbers of minor peaks equal to the integer size of the horizon radius. These additional wave numbers present within the system explain the discrepancy between the ideal and the MBC solutions. The MBC defined previously is specifically designed to only absorb wave numbers approaching 0. Higher wave numbers are absorbed with decreasing efficiency to a point where they are cannot be absorbed at all.

While adding nodes increased the NMBC effectiveness, adding more nodes to the boundary domain doesn't increase the NMBC effectivity without bounds. To depict this constraint a model is built such that there is an increasing number of nodes within the boundary domain. The model is run with multiple neighborhood sizes with an M in (105) being incrementally increased until the effectivity of the NMBC stabilizes. Using this approach, a plateau for NMBC effectivity occurs when the boundary domain is twice the size of the radius of the horizon and can be seen in Figure 13.

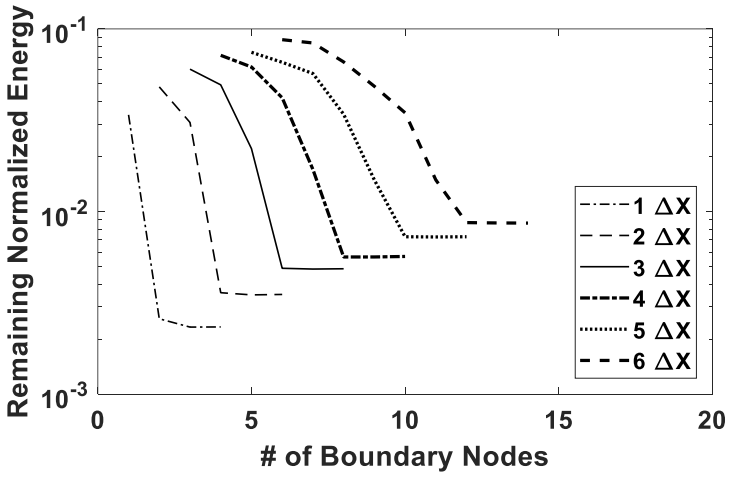

Figure 13: Convergence of the effectivity of the first order NMBC as the number of nodes within the boundary domain increase

4.4 NMBC for NOPD with Stabilized Correspondence Model

The addition of the stabilized term to NOPD allows for the zero energy modes to be managed effectively. In fact, the zero energy modes can be eliminated almost entirely with very small values of G added to the previous example. For local horizon, the G values only need to be as large as 0.03 in order to eliminate any zero energy mode within the simulation. From Figure 14 it can be seen that as G values increase, the minor peaks caused by the zero energy modes are

either reduced or eliminated. With fewer minor peaks of energy within the initial displacement of the wave, the NMBC can function more efficiently in absorbing the long wave $(\xi \to 0)$.

The same NMBC that is shown to function with NOPD can also be applied to the stabilized NOPD. With the same numerical example as before, the results on the effectivity of the NMBC can be evaluated and shown in Figure 15. As mentioned earlier, if the selected G values do not satisfy the stability condition associated with the reflection coefficient, it will cause the energy at some wave-lengths to be amplified which will eventually lead to instability. This can be seen clearly in Figure 15e and Figure 15f for NMBC2.

By the numerical examples in Figure 15 it is clear to see that the higher order NMBCs function for the stabilized NOPD. The constraints discussed earlier become visually apparent in Figure 15, specifically that, as the upper G boundary is surpassed, the simulations begin to exhibit large oscillations in total system energy. It should also be noted that as the G values approach the bounds defined in Eqs. (98) or (99) the computational time step is required to be reduced. Table 4, 5, and 6 callout the total normalized energy in the system at the end of the simulation.

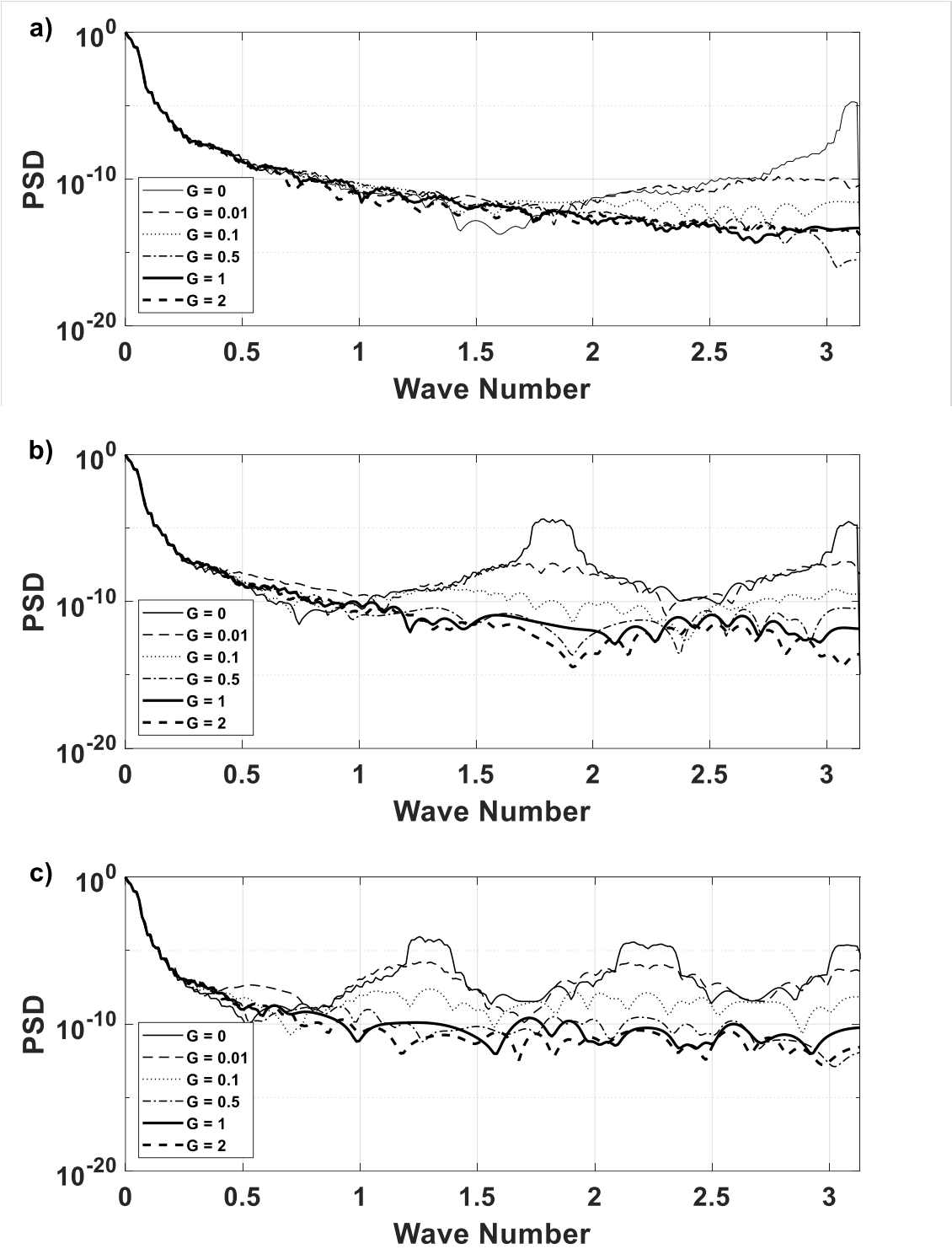

Figure 14: PSD for a SNOPD neighborhood of a) $\delta = \Delta X$ **, b)** $\delta = 2\Delta X$ **, and c)** $\delta = 3\Delta X$ **.**

Table 4: Effectivity of NMBC for $\delta = \Delta X$ with $\Delta X = 1$ at $t = 54.88$.

G	0	0.25	0.5	0.75	1	2	4
NMBC1	6.3×10^{-4}	2.5×10^{-5}	1.13×10^{-4}	2.19×10^{-4}	3.3×10^{-4}	7.69×10^{-4}	1.51×10^{-3}
G	0	0.25	0.5	0.75	1	1.15	1.3333
NMBC2	--	4.04×10^{-6}	3.24×10^{-6}	9.23×10^{-6}	2.5×10^{-5}	4.1×10^{-5}	8.1×10^{-5}

Table 5: Effectivity of NMBC for $\delta = 2\Delta X$ with $\Delta X = 1$ at $t = 54.88$.

G	0	0.25	0.5	0.75	1	2	4
NMBC1	3.1×10^{-3}	9.77×10^{-6}	6.3×10^{-6}	4.69×10^{-6}	3.02×10^{-6}	4.72×10^{-7}	3.34×10^{-7}
G	1.6	1.75	2	2.25	2.5	2.75	--
NMBC2	1.23×10^{-6}	5.44×10^{-7}	7.73×10^{-7}	5.23×10^{-7}	2.83×10^{-7}	2.49×10^{-7}	

Table 6: Effectivity of NMBC for $\delta = 3\Delta X$ with $\Delta X = 1$ at $t = 54.88$.

G	0	0.25	0.5	0.75	1	2	4
NMBC1	7.9×10^{-3}	4.7×10^{-5}	2.7×10^{-5}	2.4×10^{-5}	1.9×10^{-5}	7.92×10^{-6}	1.28×10^{-6}
G	3.75	4	4.25	4.4	--	--	--
NMBC2	1.5×10^{-5}	1.25×10^{-6}	1.09×10^{-6}	1.12×10^{-6}			

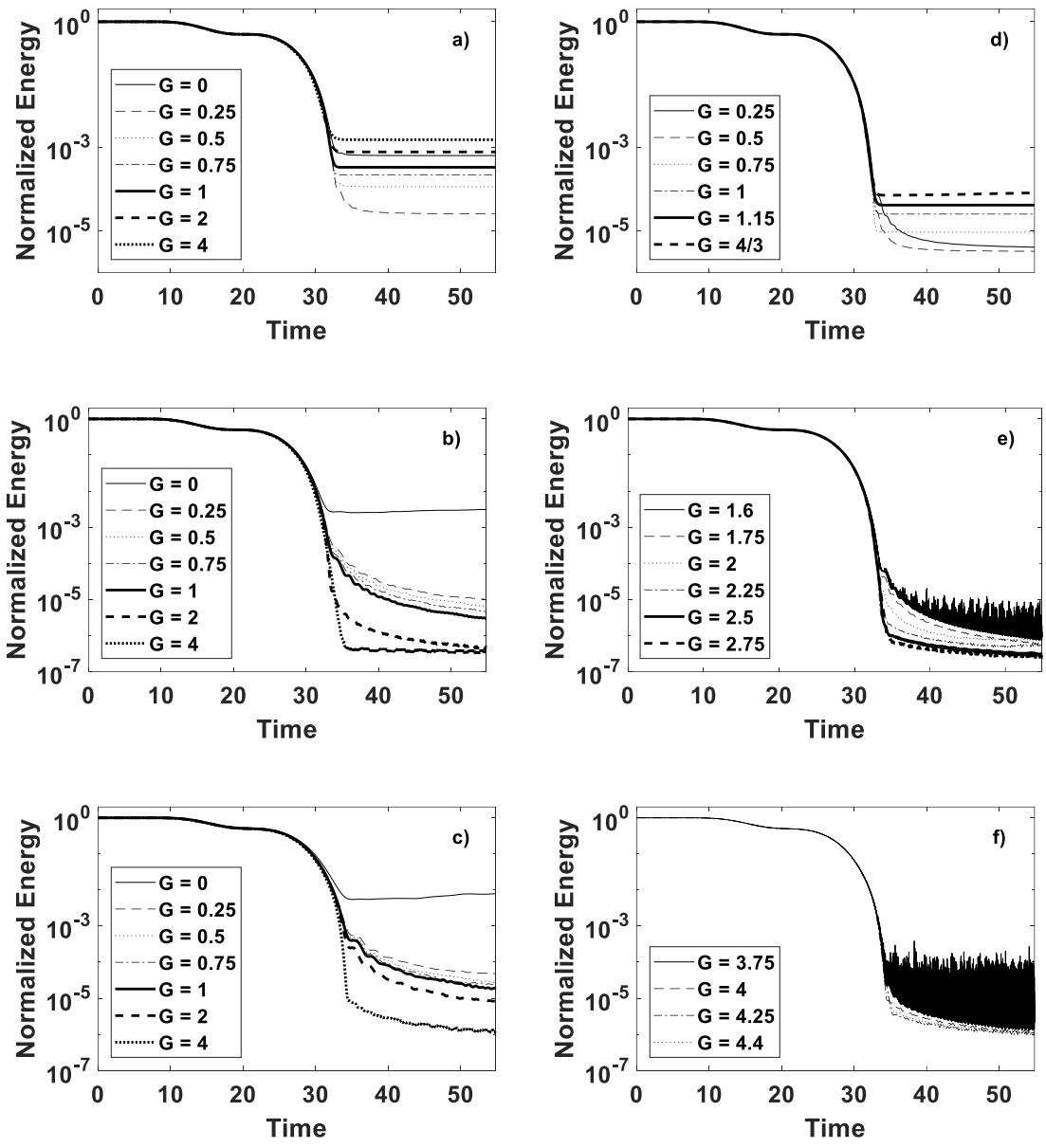

Figure 15: NMBC Effectivity for various G values for NMBC1 of horizon radii a) $\delta = \Delta X$, b) $\delta = 2\Delta X$, and c) $\delta = 3\Delta X$. The same is demonstrated for NMBC2 with d) $\delta = \Delta X$, e) $\delta = 2\Delta X$, and f) $\delta = 3\Delta X$.

Overall it can be seen that the stabilized version of NOPD with correspondence material model allows the use of higher order NMBC at the boundary and functions quite well. Particular values of G can change the overall effectivity of the NMBC: while initial values of G result in

increasing effectivity of the NMBC, continuing to increase the value of G results in an eventual decrease of effectivity as seen in Figure 15. This is most notable in the case of $\delta = \Delta X$ and NMBC1. It is also possible for NMBC1 to be as efficient as NMBC2 with particular selections of G. However, the corresponding G values are found to be large and lead to a domination of the stabilization force density over the original peridynamic force density which subsequently results in a non-representative physical response.

4.5 Two Dimensional Unidirectional NMBC for Non-Ordinary Peridynamics

The NMBCs derived earlier for the 1D case can be extended to the two-dimensional cases. Here we illustrate the application of NMBC for NOPD in 2D assuming a square lattice and unidirectional wave propagation, i.e., the direction of the wave poses an angle of 0 with respect to the x axis. Application to OPD under the same assumption follows a similar procedure.

The revised NMBC for a left boundary domain in 2D NOPD is given as

$$\sum_{i=0}^{N} C_i^{(M)} \dot{\mathbf{u}}_{i-M,j} - \sum_{i=0}^{N} B_i^{(M)} \mathbf{u}_{i-M,j} = 0 \quad \text{for} \quad M = 0,\ ...,\ 2n-2,\ 2n-1 \tag{113}$$

where subscript i and j are the nodal index in the *x* and *y* direction, respectively. In addition, M is the index that is introduced for the purpose of eliminating the edge effect. $C_i^{(M)} = \begin{bmatrix} c_{i,11} & c_{i,12} \\ c_{i,21} & c_{i,22} \end{bmatrix}^{(M)}$ and $B_i^{(M)} = \begin{bmatrix} b_{i,11} & b_{i,12} \\ b_{i,21} & b_{i,22} \end{bmatrix}^{(M)}$ are the MBC coefficient matrices to be determined and $C_0^{(M)} = \begin{bmatrix} 1 & 0 \\ 0 & 1 \end{bmatrix}^{(M)}$. Finally the 2D nodal displacement vector is $\mathbf{u}_{i,j} = \begin{bmatrix} u_{i,j} \\ v_{i,j} \end{bmatrix}$. The treatment shown

in Eq. (113) is similar at right, top, and bottom boundaries such that the indices are always summed towards the internal domain as shown in Figure 16.

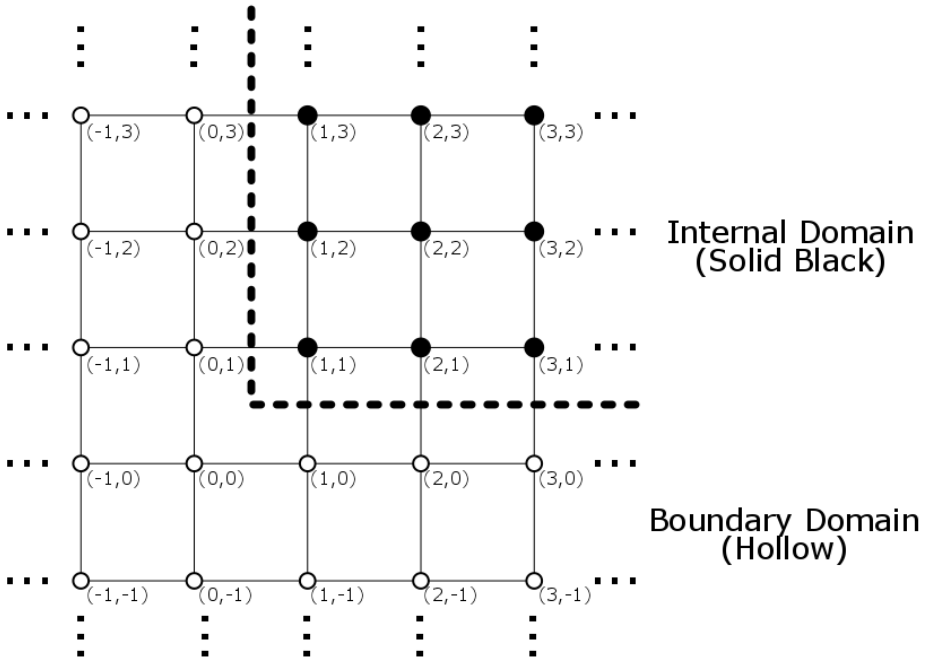

Figure 16: The boundary domain for a unidirectional 2D PD NMBC

Based on Eq.(113), the 2D NMBC residual function is defined using a modified wave given as

$$\mathbf{u}_{i-M,j} = \begin{bmatrix} u_{i-M,j} \\ v_{i-M,j} \end{bmatrix} = \begin{bmatrix} U \\ V \end{bmatrix} e^{\bar{i}(\omega t + (i-M)\xi_x \Delta X + j\xi_y \Delta X)} \tag{114}$$

$$\bar{i}\,\omega\left(\xi_x, \xi_y\right) \sum_{i=0}^{N} C_i^{(M)} \begin{bmatrix} U \\ V \end{bmatrix} e^{\bar{i}((i-M)\xi_x \Delta X + j\xi_y \Delta X)} - \sum_{j=0}^{N} B_i^{(M)} \begin{bmatrix} U \\ V \end{bmatrix} e^{\bar{i}((i-M)\xi_x \Delta X + j\xi_y \Delta X)} = \Delta_M\left(\xi_x, \xi_y\right) \tag{115}$$

in which ξ_x, ξ_y are the wave numbers in the *x* and *y* direction respectively.

With a unidirectional wave assumption $\xi_x = \xi$ and $\xi_y = 0$. Eq. (115) then becomes

$$\bar{i}\,\omega(\xi,0)\sum_{j=0}^{N}C_i^{(M)}\begin{bmatrix}U\\V\end{bmatrix}e^{\bar{I}((i-M)\xi\ \Delta X)}-\sum_{j=0}^{N}B_i^{(M)}\begin{bmatrix}U\\V\end{bmatrix}e^{\bar{I}((i-M)\xi\ \Delta X)}=\Delta_M(\xi,0) \tag{116}$$

Since the solutions are independent of each M in (116), the coefficients only need to be solved once. Recall that the dispersion relation for the unidirectional wave is given in (80). We can solve for the coefficient matrices through

$$\left.\frac{d^n\Delta\left(\omega_p^{\alpha=0}(\xi,0)\right)}{d\xi^n}\right|_{\xi=0}=0\ \Big|\forall\ n=0,1,2,3,...,2N,\ \text{and}\ \ p=1,\,2 \tag{117}$$

For a first order expansion, where $N=1$, we can get the following set of 6 equations to solve for the coefficient matrices for a local 2D NOPD NMBC assuming $\Delta X=1$ and using the first dispersion relation derived from Eq.(80):

$$\begin{bmatrix}-b_{0,11}-b_{1,11}\\-b_{0,12}-b_{1,12}\end{bmatrix}=\begin{bmatrix}0\\0\end{bmatrix},\quad\begin{bmatrix}\dfrac{4c\bar{i}\left(1+c_{1,11}\right)}{\sqrt{15}}-\bar{i}b_{1,11}\\[2ex]\dfrac{4c\bar{i}c_{1,12}}{\sqrt{15}}-\bar{i}b_{1,12}\end{bmatrix}=\begin{bmatrix}0\\0\end{bmatrix},\quad\begin{bmatrix}-\dfrac{8c\ c_{1,11}}{\sqrt{15}}+b_{1,11}\\[2ex]-\dfrac{8c\ c_{1,12}}{\sqrt{5}}+b_{1,12}\end{bmatrix}=\begin{bmatrix}0\\0\end{bmatrix},$$
$$\begin{bmatrix}-b_{0,21}-b_{1,21}\\-b_{0,22}-b_{1,22}\end{bmatrix}=\begin{bmatrix}0\\0\end{bmatrix},\quad\begin{bmatrix}\dfrac{4c\bar{i}c_{1,21}}{\sqrt{15}}-\bar{i}b_{1,21}\\[2ex]\dfrac{4c\bar{i}\left(1+c_{1,22}\right)}{\sqrt{15}}-\bar{i}b_{1,22}\end{bmatrix}=\begin{bmatrix}0\\0\end{bmatrix},\quad\begin{bmatrix}-\dfrac{8c\ c_{1,21}}{\sqrt{15}}+b_{1,21}\\[2ex]-\dfrac{8c\ c_{1,22}}{\sqrt{15}}+b_{1,22}\end{bmatrix}=\begin{bmatrix}0\\0\end{bmatrix} \tag{118}$$

Solving for the coefficients gives us the following coefficient matrices.

$$C_0^{(M)}=\begin{bmatrix}1&0\\0&1\end{bmatrix},\ C_1^{(M)}=\begin{bmatrix}1&0\\0&1\end{bmatrix}$$
$$B_0^{(M)}=\begin{bmatrix}\dfrac{-8c}{\sqrt{15}}&0\\[2ex]0&\dfrac{-8c}{\sqrt{15}}\end{bmatrix},\ B_1^{(M)}=\begin{bmatrix}\dfrac{8c}{\sqrt{15}}&0\\[2ex]0&\dfrac{8c}{\sqrt{15}}\end{bmatrix} \tag{119}$$

which creates the following NMBC when (119) is used in (113)

$$\dot{\mathbf{u}}_{i-M,j} = \begin{bmatrix} \dot{u}_{i-M,j} \\ \dot{v}_{i-M,j} \end{bmatrix} = \begin{bmatrix} -\dot{u}_{i-M+1,j} + c\left(\dfrac{-8}{\sqrt{15}} u_{i-M,j} + \dfrac{8}{\sqrt{15}} u_{i-M+1,j} \right) \\ -\dot{v}_{i-M+1,j} + c\left(\dfrac{-8}{\sqrt{15}} v_{i-M,j} + \dfrac{8}{\sqrt{15}} v_{i-M+1,j} \right) \end{bmatrix} \quad \text{for } M = 0,1 \qquad (120)$$

To test the 2D NMBC, we consider the case of a unidirectional wave propagating in 2D. The 2D domain is rectangular in shape with dimensions of 20 by 175. It is discretized by 20×175 nodes with uniform nodal spacing of $\Delta X = 1$. The material properties are given as mass density $\rho = 1$, Young's modulus $E = 100$, and Poisson's ratio $\upsilon = 0.25$. A wave is created in the center of the domain such that the wave is uniform across the 20 nodes that define the width of the internal domain. The wave profile is imposed at the PD nodes with coordinates satisfying $87.5 - 2\delta \le Y \le 87.5 + 2\delta$ for $-10 < t < 0$:

$$v(Y,t) = \frac{\varepsilon_0}{2}\left(\cos\left(\frac{2\left(|t_{\min}| + t\right)\pi}{|t_{\min}|} \right) + 1 \right) \quad \text{for } -10 \le t < 0 \qquad (121)$$

where $\varepsilon_0 = 0.01$ and $t_{\min} = -10$ and v is the displacement in the y direction. NMBC are defined on opposite sides at the boundary where the initial y coordinates are 0 and 175. The wave propagates to the boundary with NMBC imposed at the ends of the internal domain. Figure 17 shows the contours of the wave at time $t = -5$, 7.5 and 15 for the case of $\delta = \Delta X$ and $G = 1$. It can be seen that the initially imposed wave travels to both the top and bottom boundaries. No visible reflections were seen as the wave reaches the boundary at $t = 7.5$. Finally, most of the wave has been transmitted out of the boundary as evidenced by Figure 17c.

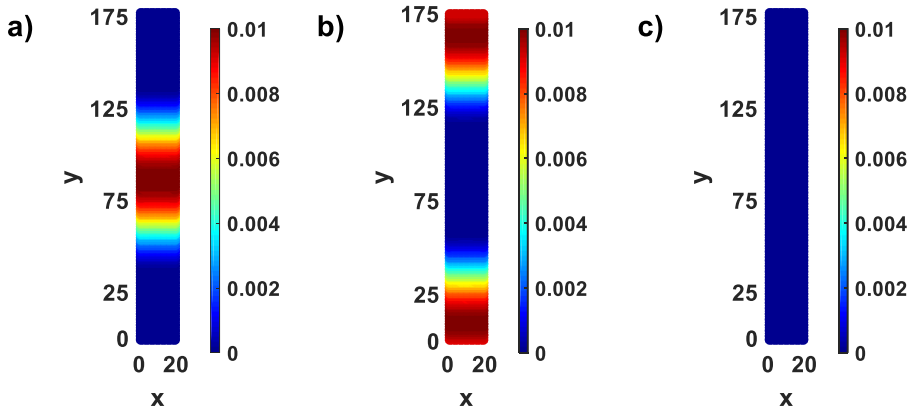

Figure 17: Contour plots of the *y* displacement at a) $t=-5$ **and b)** $t=7.5$ **and c)** $t=15$ **for** $\delta=\Delta X$ **with** $G=1$ **for the unidirectional NMBC simulation.**

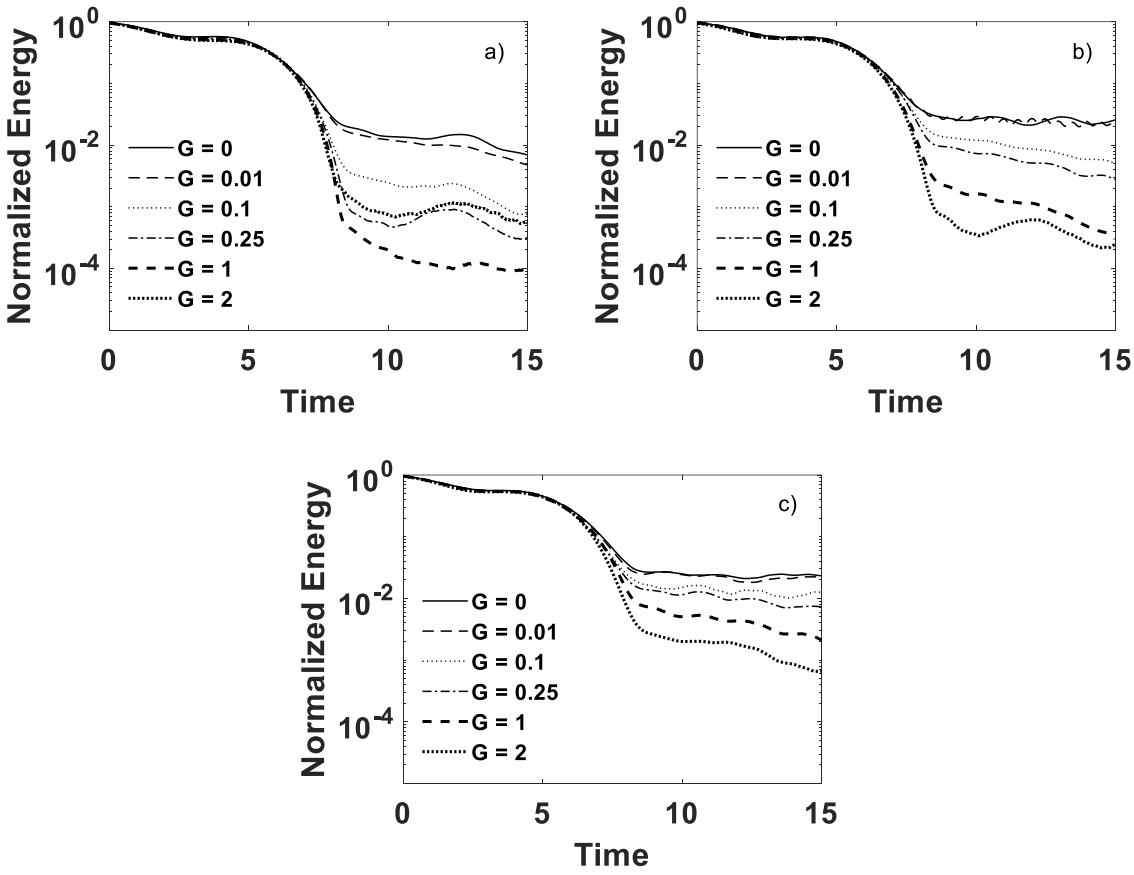

Figure 18: Normalized energy history of the 2D unidirectional wave for the cases of a) $\delta=\Delta X$ **, b)** $\delta=2\Delta X$ **, and c)** $\delta=3\Delta X$ **.**

Table 7: Normalized energy at $t=15$ based on the 2D unidirectional NMBC in Figure 18.

G	0	0.01	0.1	0.25	1	2
$\delta=\Delta X$	6.91×10^{-3}	4.77×10^{-3}	7.61×10^{-4}	6.9075×10^{-3}	9.09×10^{-5}	5.5×10^{-4}
$\delta=2\Delta X$	2.5×10^{-2}	2.2×10^{-2}	5.0×10^{-3}	2.8×10^{-3}	3.9×10^{-4}	2.4×10^{-4}
$\delta=3\Delta X$	2.3×10^{-2}	2.2×10^{-2}	1.25×10^{-2}	7.2×10^{-3}	2.1×10^{-3}	6.6×10^{-4}

To further quantify the effectiveness of the NMBC implementation for 2D, Figure 17 provides the normalized energy in the system as a function of time for the different choices of neighborhoods of $\delta=\Delta X$, $2\Delta X$, and $3\Delta X$ with $\Delta X=1$ and values of the stabilization parameter G. It can be seen that, in all cases, NMBC for 2D performs well and the effectiveness is similar to 1D. Table 7 lists the specific values of the normalized energy at $t=15$. The higher G values also reduce the effects of the zero energy modes in that we see reductions in the energy remaining in the system when the stabilization parameter is increased. A reversal in effectivity is seen as G is increased from 1 to 2 in $\delta=\Delta X$ due to the fact that there is no longer as much energy being removed from the system. This same attribute is seen in the 1D effectivity as well.

4.6 Two Dimensional Multidirectional NMBC for Non-Ordinary Peridynamics

The wave dispersion for the 2D rectangular lattice can also be derived with respect to a wave with an arbitrary incident angle. In the case of $\delta=\Delta X=1$ this is given as:

$$\omega_{\delta=1}=\sqrt{\frac{2}{15\pi}}\sqrt{\begin{pmatrix}90G+8\pi-60G\cos\left(\xi\cos\alpha\right)+\left(15G-4\pi\right)\cos\left(2\xi\cos\alpha\right)\\-60G\cos\left(\xi\sin\alpha\right)+\left(15G-4\pi\right)\cos\left(2\xi\sin\alpha\right)\end{pmatrix}} \tag{122}$$

which can be employed to obtain the following NMBC1 coefficients:

$$C_0^{(M)} = \begin{bmatrix} 1 & 0 \\ 0 & 1 \end{bmatrix},\ C_1^{(M)} = \begin{bmatrix} 1 & 0 \\ 0 & 1 \end{bmatrix}$$

$$B_0^{(M)} = \left(\sin^2\alpha + \cos^2\alpha\right)\begin{bmatrix} \frac{-8c}{\sqrt{15}} & 0 \\ 0 & \frac{-8c}{\sqrt{15}} \end{bmatrix},\ B_1^{(M)} = \left(\sin^2\alpha + \cos^2\alpha\right)\begin{bmatrix} \frac{8c}{\sqrt{15}} & 0 \\ 0 & \frac{8c}{\sqrt{15}} \end{bmatrix} \tag{123}$$

It is easily seen that this simplifies to the same coefficients given in (119). Similar conclusions can be drawn for the cases of larger neighborhoods, i.e., the NMBC1 coefficients are independent of the incident angle of the wave. This result greatly simplifies the numerical implementation.

In the last example, we show the functionality of the NMBC developed in (123) to a multidirectional wave. We consider a case of wave propagating in 2D rectangular shaped domain with dimensions of 150×275. In terms of numerical discretization 150 nodes are prescribed in the x direction and 275 nodes are prescribed in the y direction with uniform spacing of $\Delta X = 1$. Both standard and stabilized NOPD are considered and the material properties are given as mass density $\rho = 1$, Young's modulus $E = 100$, Poisson's ratio $\upsilon = 0.25$. For the case of stabilized NOPD, the values of the parameter G have been chosen to be 0.25, 0.5, and 1 to evaluate its effect. 'Ideal' 2D simulations are also run with an expanded domain of 750×1375 nodes with system energy being tracked only for the middle 150×275 block of nodes. The initial wave profile is given in terms of the prescribed displacement v in the y direction, given as

$$v(Y, t=0) = \begin{cases} \frac{\varepsilon_0}{2}\left[\sin\left(\frac{\pi r_i}{r_{\max}} + \frac{\pi}{2}\right) + 1\right] & r_i \le r_{\max} \\ 0 & r_i > r_{\max} \end{cases} \tag{124}$$

in which $\varepsilon_0 = 0.001$, $r_i = \sqrt{\left(X_i - \frac{150}{2}\right)^2 + \left(Y_i - \frac{275}{2}\right)^2}$, $r_{\max} = 60$.

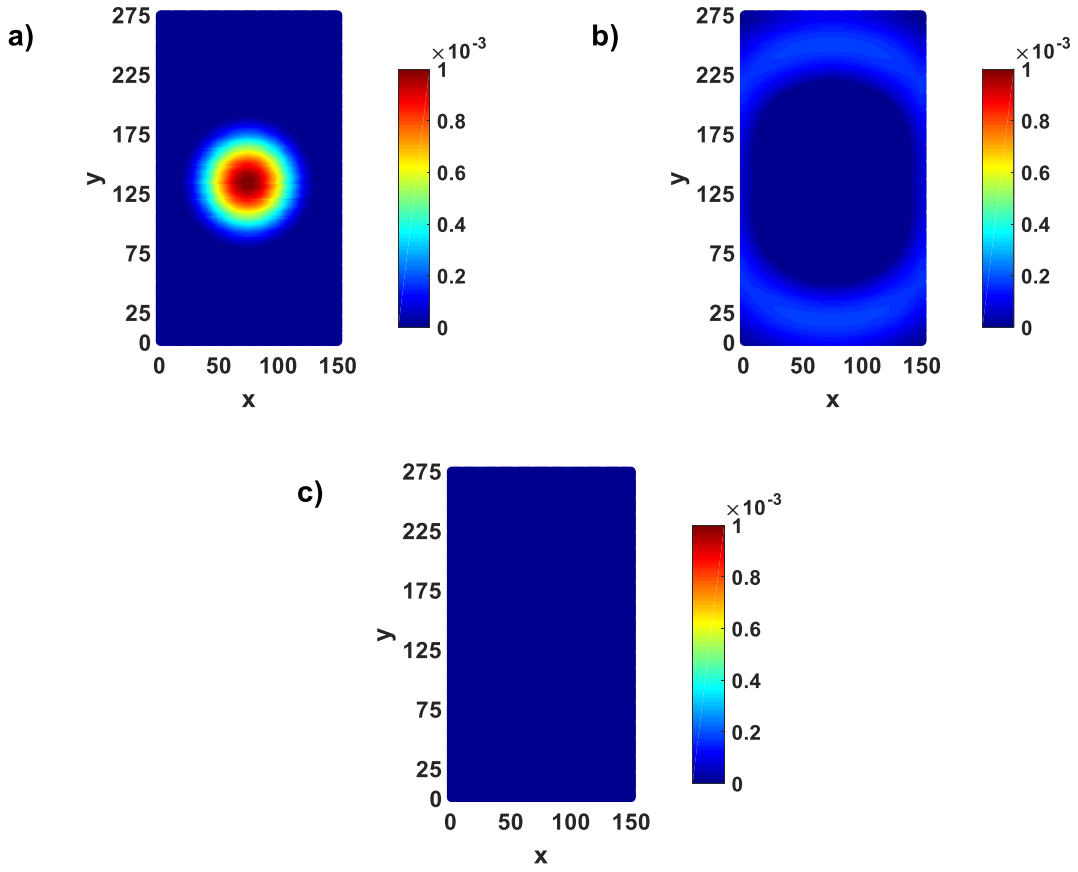

Figure 19: Contour plots of the *y* displacement at a) $t = 0$ **, b)** $t = 10$**, and c)** $t = 40$ **for** $\delta = \Delta X$ **,** $G = 0$ **and NMBC1.**

Figure 19 shows the contour of the displacements in the y direction at different times of the simulation using standard NOPD. The effectivity of the imposed NMBC1 is clearly demonstrated based on the contour plot at $t = 40$ (Figure 19c), in which no visible reflections are observed.

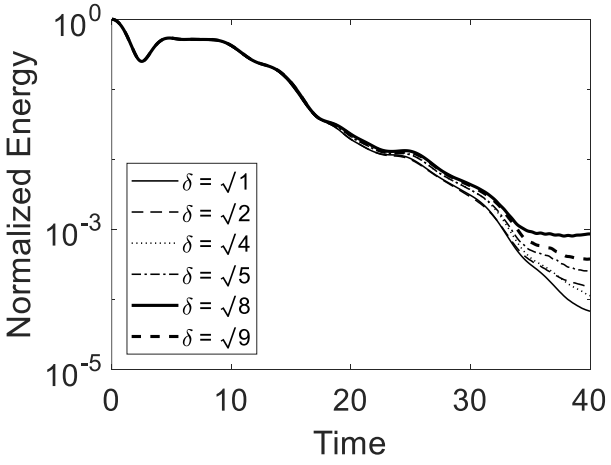

Figure 20: Effectivity of the 2D NMBC1 with $G = 0$ for various horizon sizes.

Figure 20 shows the system energy retained in the domain as a function of time and different neighborhood sizes for the case of standard NOPD. It can be seen within the 2D results that the differences in the energy remaining in the system for $\delta = 2\Delta X$ and $\delta = 3\Delta X$ are not significant when compared to the results for the same neighborhoods in the 1D cases. In addition, more energy within the system remains as the neighborhood radius becomes larger.

Table 8: NMBC1 effectivity remaining for various neighborhoods with $G = 0$ at $t = 40$.

δ	$\sqrt{1}$	$\sqrt{2}$	$\sqrt{4}$	$\sqrt{5}$	$\sqrt{8}$	$\sqrt{9}$
NMBC1	1.04×10^{-4}	2.34×10^{-4}	1.65×10^{-4}	4.06×10^{-4}	1.30×10^{-3}	6.06×10^{-4}

Figure 21 shows the time history of the normalized system energy as a function of the stabilization parameters G and horizon size δ . It is observed that the overall effectivity doesn't change much for the values of G presented. We attribute this to the displacement being predefined at $t = 0$ rather than generating the wave within the simulation. The ratios of the remaining energy

to the initial energy at $t = 40$ in the system are provided in Table 9 for the choices of different values of G and δ. It can be seen that the ratios are all on the order of 10^{-4}.

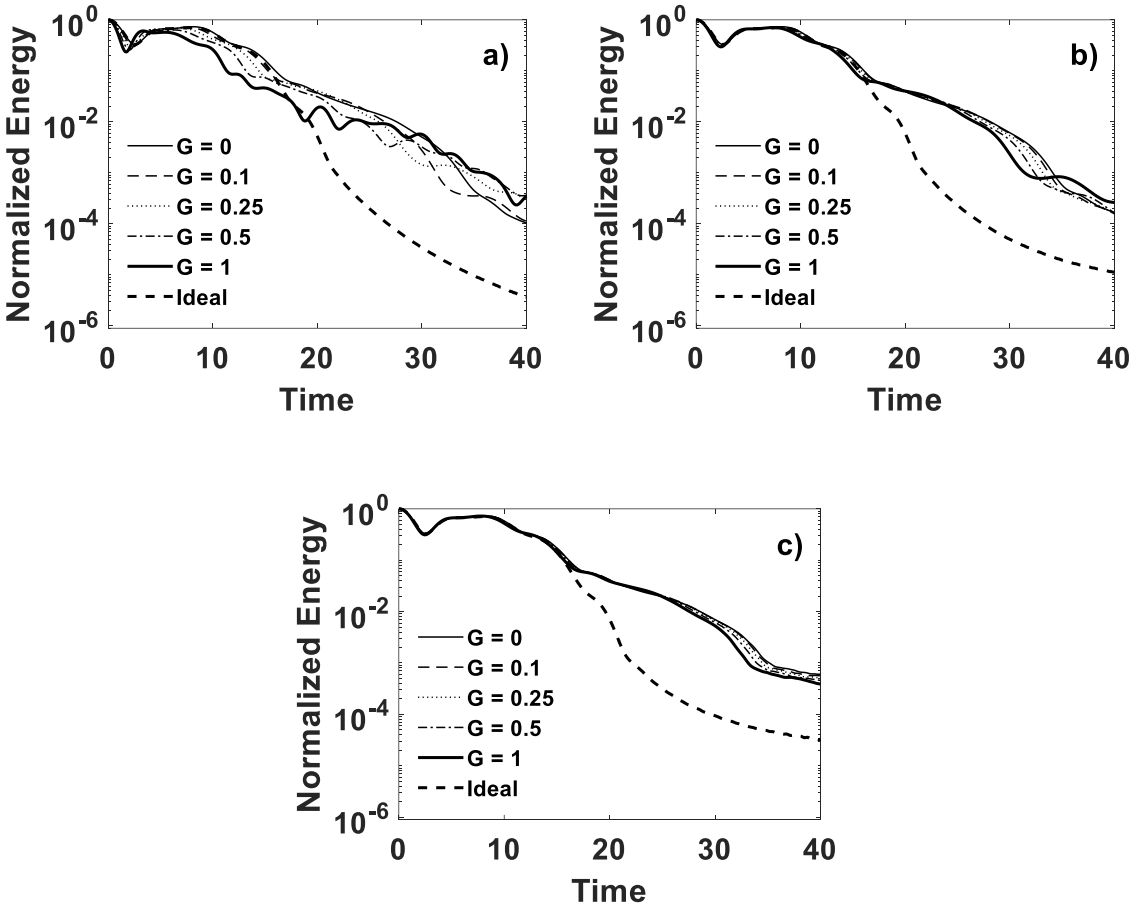

Figure 21: 2D NMBC1 multidirectional wave effectivity for various G values for a) $\delta = \Delta X$, b) $\delta = 2\Delta X$, and c) $\delta = 3\Delta X$.

Table 9: Final effectivity of 2D NMBC1 for various neighborhoods at t=40

G	0	0.1	0.25	0.5	1
$\delta = \Delta X$	1.04×10^{-4}	1.13×10^{-4}	2.71×10^{-4}	3.64×10^{-4}	3.48×10^{-4}
$\delta = 2\Delta X$	1.65×10^{-4}	1.58×10^{-4}	1.55×10^{-4}	1.65×10^{-4}	2.62×10^{-4}
$\delta = 3\Delta X$	6.06×10^{-4}	5.61×10^{-4}	5.20×10^{-4}	4.59×10^{-4}	3.88×10^{-4}

From the above results it can be seen that the NMBC functions well in its intended purpose. A large majority of the energy within the system is absorbed as the wave meets the boundary without reflection back into the domain. In fact, the NMBC1 boundary for the 2D setup can be more than 99.9% effective in dissipating energy with only the first order NMBC.

4.7 Effectiveness of Peridynamic NMBC

To evaluate the effectiveness of the proposed NMBC, we evaluate the reflection coefficient for each different cases. We consider the following definition:

$$u_I = e^{\bar{i}(\omega t+\xi I\Delta X)} + Re^{\bar{i}(\omega t-\xi I\Delta X)}. \tag{125}$$

where R measures the reflection of waves. This can be substituted back into (84) to get

$$R(\xi) = -\frac{\Delta(\xi)}{\Delta(-\xi)}\ . \tag{126}$$

Looking back to (85) this can be reorganized to get

$$\begin{aligned} &\Delta(\xi) = \bar{i}\left[\omega(\xi)-\omega_b(\xi)\right]\sum_{j=0}^{N} c_j \\ &\text{with}\quad \bar{i}\,\omega_b(\xi) = \frac{\sum_{j=0}^{N} b_j e^{\bar{i}j\xi\Delta X}}{\sum_{j=0}^{N} c_j e^{\bar{i}j\xi\Delta X}}. \end{aligned} \tag{127}$$

With this (126) can be restated as

$$\left|R(\xi)\right| = \left|\frac{\omega(\xi)-\omega_b(\xi)}{\omega(\xi)+\omega_b(\xi)}\right|\ . \tag{128}$$

In this way the reflection coefficient can be calculated for BBPD, OPD, and NOPD in comparison to the MD reflection coefficient. In fact, for BBPD and OPD, the comparison to MD is straightforward in that, for $\Delta X = 1$, the dispersion relations are the same with equivalent constitutive constants. With this the coefficients were calculated to be the same in Figure 22 and will therefore have the same reflection coefficient. NOPD will have a different reflection coefficient because the dispersion relation is different. This difference can be seen below in Figure 22.

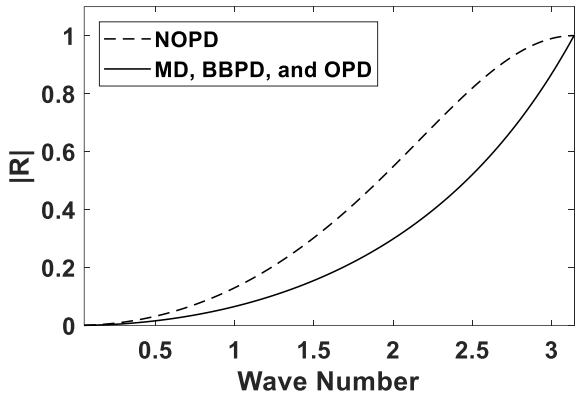

Figure 22: Comparison of local reflection coefficients for BBPD, OPD, NOPD, and MD for MBC1

While all of the methods operate well at low wave numbers, higher wave numbers are not well-handled. It is interesting to note that the NOPD exhibits a particularly non-linear reflection coefficient. Because of this non-linearity, NOPD is less efficient with increasing wave numbers when compared to MD, BBPD, and OPD as the wave numbers increase from 0 to π.

Peridynamic internal force calculations change as the horizon size changes which, in turn, modify the respective dispersion relations. These changes then propagate to the reflection coefficient. The results in Figure 23 below are for neighborhoods up to $5\Delta X$ for BBPD, OPD and

NOPD. Since the reflection coefficient is a function of the dispersion, it inherits any periodicity from the respective dispersion relations. For the cases of $\delta > 1$, we can see that BBPD and OPD monotonically increase as the wave numbers increase from 0 with OPD becoming slightly irregular as the horizon radius increases. For NOPD the reflection coefficient does not monotonically increase from 0 to 1 as wave number increases. Instead, it reaches 1 at discrete wave numbers showing some level of transmission in between. It should be noted that as the wave number increases the reflection coefficient reaches a value of 1 at wave number below π which coincides with the zero energy modes that are present in the PSD plots given in Figure 14. This property is the same for larger neighborhoods and indicates that the MBC has a reflection coefficient of 1 for all zero energy modes that are present within NOPD. Therefore the zero energy modes are fully reflected from the MBC boundary region without any absorption.

For higher order NOPD NMBC the local dispersion relation gives only singular values and therefore cannot have a reflection coefficient calculated. For the larger neighborhoods, even though the coefficients that are solved for give an unstable solution in the computational model, it is still possible to calculate the theoretical reflection coefficients. Given in Figure 24 are the reflection coefficient plots for neighborhood radii of 2 and 3 of NOPD. As seen in that figure the higher order MBC coefficients do have a theoretical capability to absorb long waves more effectively. The zero energy modes are still having an effect as the higher order NMBC still show a reflection coefficient of 1 where the zero energy modes are excited. The order of the NMBC is limited for standard NOPD though. Recall that the singularities found in 4.1 constrain NOPD such that it can only solve for NMBC coefficients of order $N \leq 2n$.

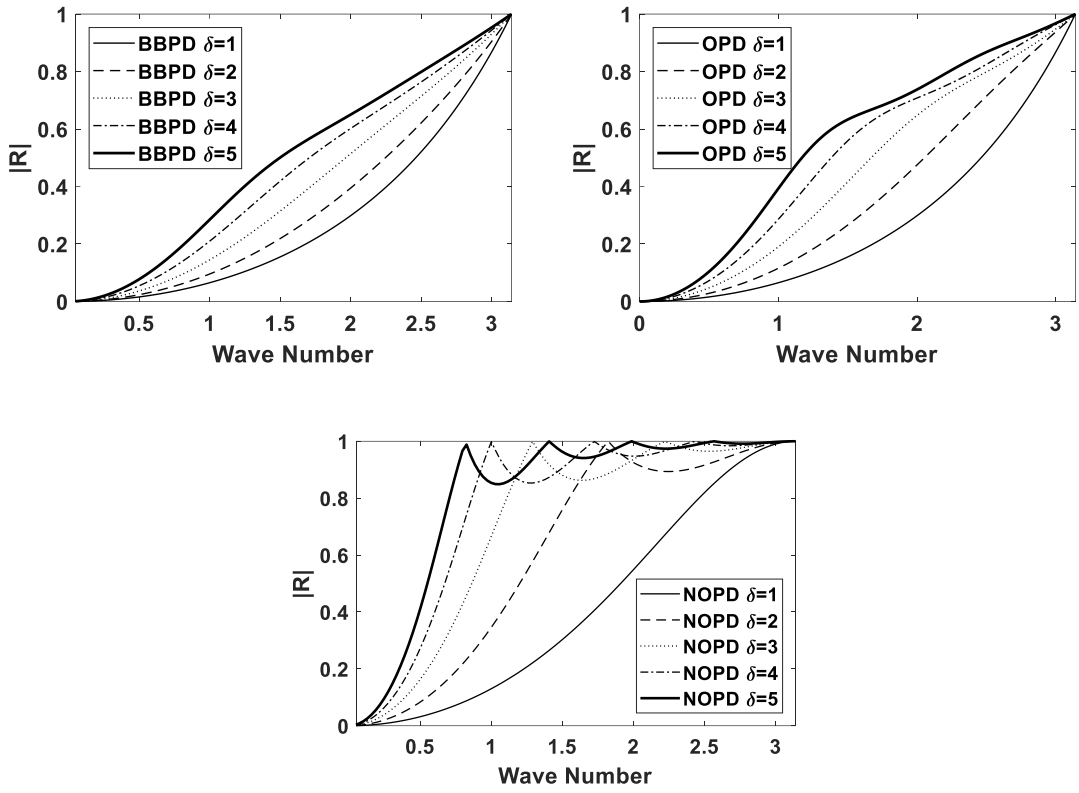

Figure 23: Plots for the reflection coefficients for 1D BBPD, OPD, and NOPD

With the stabilized correspondence material the reflection coefficients can be derived to showcase the necessity for the bounds of G stated earlier. By using the generalized dispersion relation for the stabilized correspondence material in Eq. (66) and the corresponding MBC coefficients the reflection coefficient can be plotted for the NOPD stabilized correspondence material seen in Figure 25.

The SNOPD reflection coefficient represents a clearer picture of the MBC ability to absorb incoming waves. For NMBC1 it can be seen that the reflection coefficient decreases as G is increased up to a point. For $\delta = 1$ it is apparent that increasing the stabilization value too far will begin to result in detrimental effects, in that the absorption of waves approaching the long wave

limit will be reduced which can be seen in Figure 25-a for the G values of 2 and 4. For specific values, it is observed that the reflection coefficient of smaller wave numbers begin to increase near the long wave limit. This same effect can be observed across all neighborhood sizes, though larger neighborhoods have similar reactions over larger ranges of G. Another important aspect of the SNOPD shown in the reflection coefficients in Figure 25 is that, as G values are increased, the peaks that indicate the presence of the zero energy modes drop from a reflection coefficient of 1. This indicates, through another method, that the SNOPD does mitigate the effects of the zero energy modes. In fact, with even minimal values of G the NMBC can begin to effectively absorb wave lengths that are near the wave length of a zero energy mode. This allows for a significant increase in energy absorption as evidenced throughout Chapter 4. As the range of acceptable G values are exceeded it can be seen that the reflection coefficients go above a reflection of 1. This indicates that waves whose length matches that particular wave number will not only be reflected, but amplified by the NMBC. This will lead to an eventual instability of the model as described earlier.

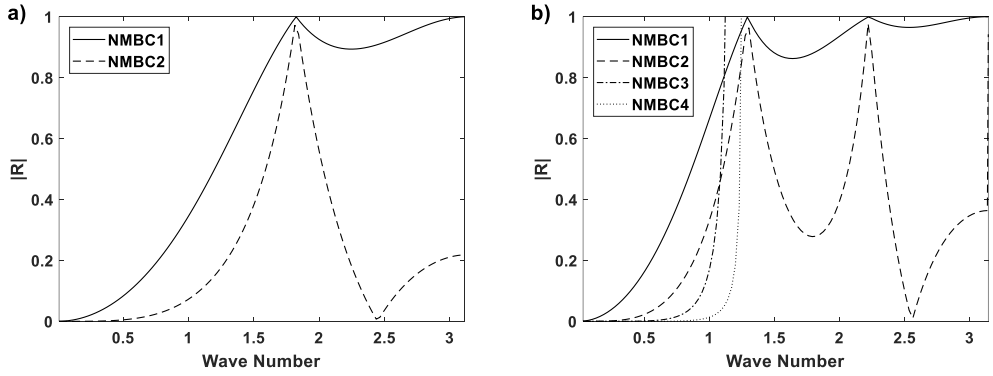

Figure 24: Reflection coefficient for higher order NMBC with NOPD for a horizon radius of a) $\delta = 1\Delta X$ **and b)** $\delta = 2\Delta X$

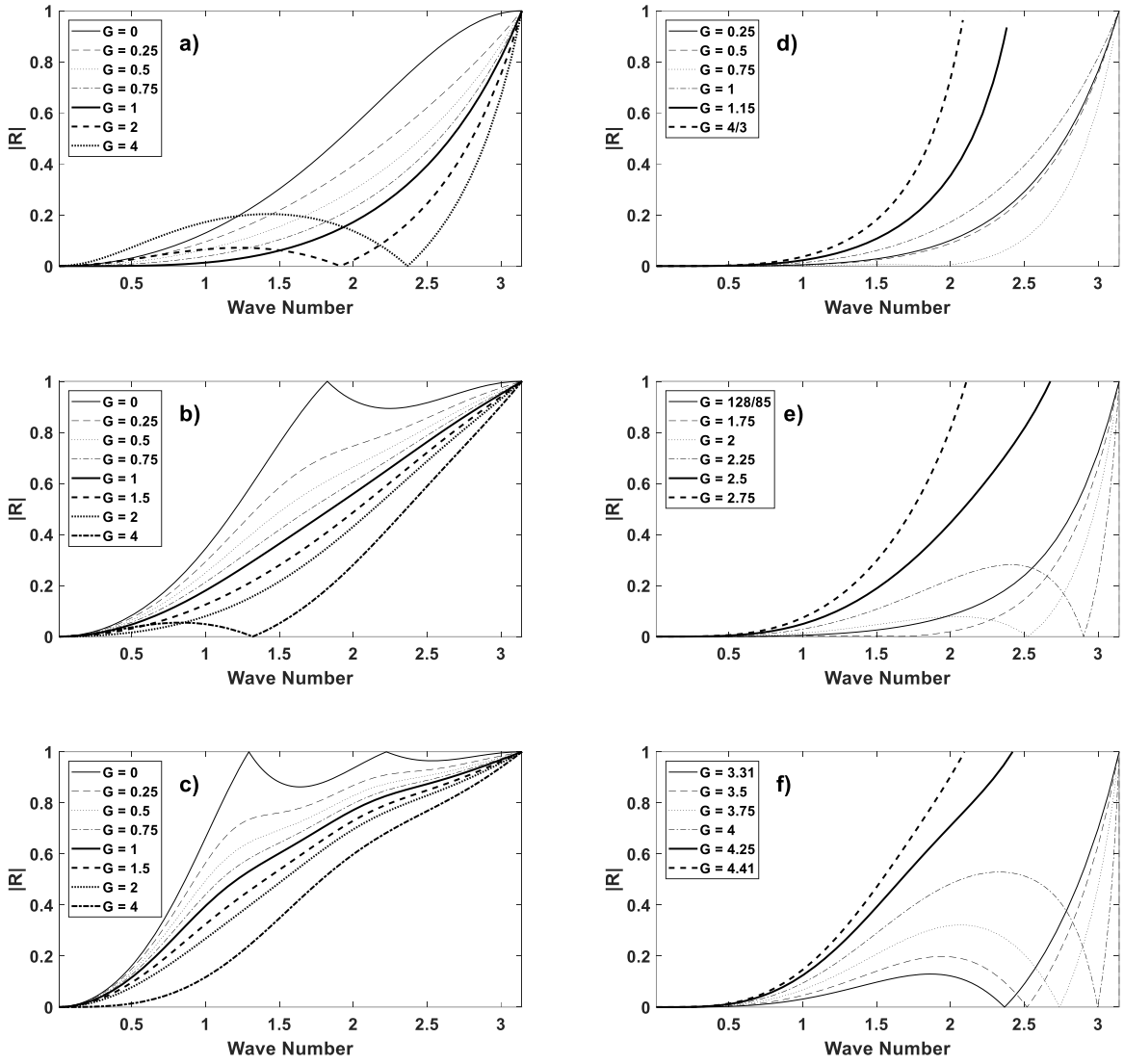

Figure 25: Reflection coefficients for SNOPD for NMBC1 for neighborhoods a) $\delta = 1\Delta X$ **, b)** $\delta = 2\Delta X$ **, and c)** $\delta = 3\Delta X$ **and NMBC2 for neighborhoods d)** $\delta = 1\Delta X$ **, e)** $\delta = 2\Delta X$ **, and d)** $\delta = 3\Delta X$ **with selected G values**

For 2D NOPD look to (80) while noting that the NMBC coefficients for the 2D NOPD dispersion relations are given in (81), (82), and (83). From this the reflection coefficients can be calculated and are given in Figure 26. In 2D as G is increased the same effect is seen as in 1D in that the reflection coefficient drops lower throughout the range of wave numbers between 0 and π

to a certain extent. Too large of G can, again, lead to increased reflections near the long wave limit of 0. This effect is especially pronounced in $\delta = 1\Delta X$.

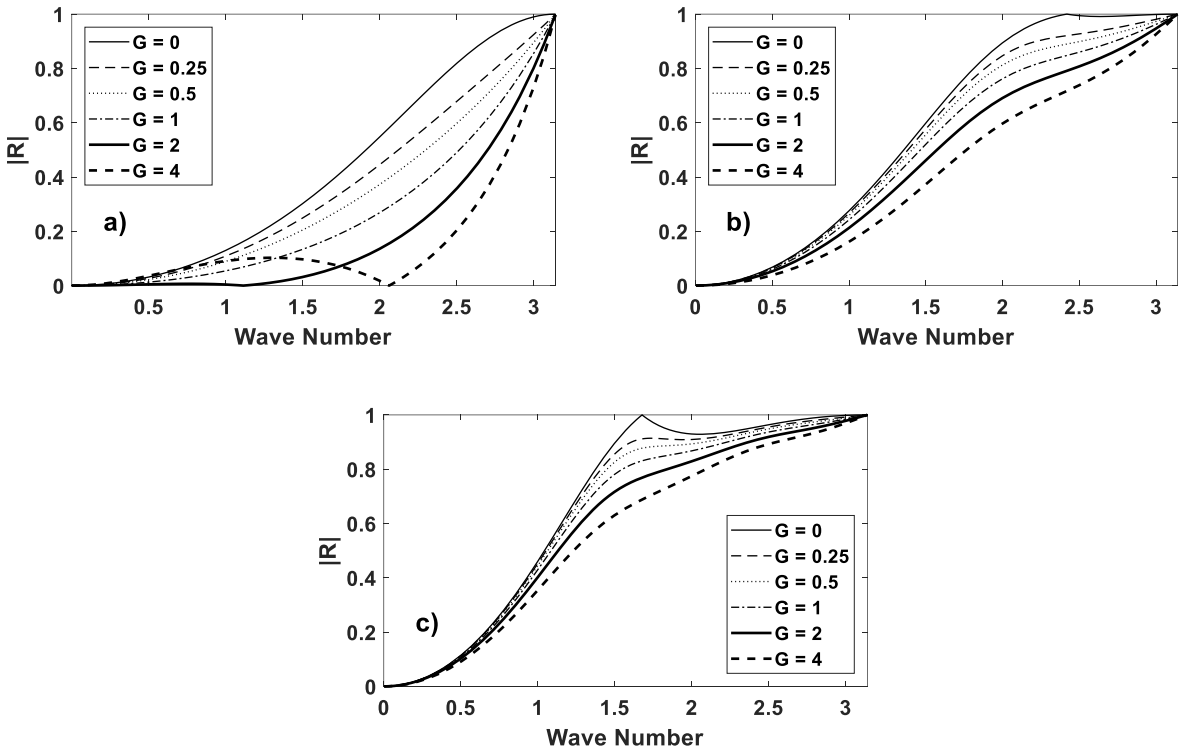

Figure 26: Reflection coefficient for 2D MBC of selected G values for a) $\delta = 1\Delta X$, b) $\delta = 2\Delta X$, and c) $\delta = 3\Delta X$

CHAPTER 5

COUPLING OF FINITE ELEMENT AND PERIDYNAMIC SIMULATIONS

In this chapter, the interfacial boundary condition established from NMBC is incorporated into a concurrent multiscale modeling scheme in which peridynamic simulation is coupled with FEM. The coupling methodology is established for both the cases of unidirectional and multidirectional waves. In addition, a 2-way NMBC is defined and implemented for a case of unidirectional wave propagation.

5.1 General Multiscale Discretization Scheme

The numerical discretization scheme for the proposed concurrent multiscale coupling method is shown in Figure 27. The FEM domain is discretized over the entire computational domain. The PD domain is prescribed over a portion of the FEM domain and therefore the two domains overlap in this coupled region. In this particular example that there are four PD nodes within each finite element.

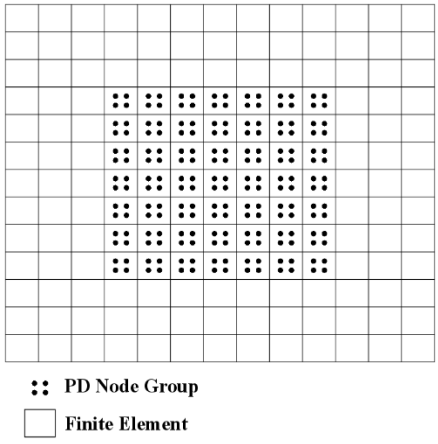

Figure 27: Discretized FEM domain with overlapping PD domain

5.2 Governing Equations

The governing equation for PD has been presented in Chapter 2. Here we briefly review the governing equations for FEM, which are derived from the conservation of linear momentum [29], also known as part of the strong form:

$$\rho\ddot{\mathbf{u}} = \nabla \cdot \boldsymbol{\sigma}(\nabla \mathbf{u}) + \mathbf{f} \tag{129}$$

in which ρ is mass density, $\mathbf{u}$ is displacement where super-imposed dots indicate temporal derivatives, ∇ is the gradient operator, $\mathbf{f}$ are body forces, and $\boldsymbol{\sigma}$ is the stress tensor. This strong form is then converted to its weak form for use in the finite element discretization and is given as

$$0 = \int_{\Omega_{FEM}} \delta\dot{\mathbf{u}}^h \cdot (\rho\ddot{\mathbf{u}} - \mathbf{f})\, d\Omega_{FEM} + \int_{\Omega_{FEM}} \delta(\nabla\dot{\mathbf{u}}^h) \cdot \boldsymbol{\sigma}(\nabla \mathbf{u}^h)\, d\Omega_{FEM} + \int_{\Gamma_t} \delta\dot{\mathbf{u}}^h \cdot \mathbf{t}\, d\Gamma_t \tag{130}$$

where $\delta\mathbf{u}^h$ is the trial function and Γ_t is the traction boundary.

In this dissertation, we used the standard 4 node quadrilateral element (also denoted as Q4 element). The shape functions are chosen such that the field variable $\mathbf{u}(\mathbf{X}, t)$ can be interpolated from the nodal solution $\mathbf{d}$ by

$$\mathbf{u}(\mathbf{X}, t) = \mathbf{N}(\mathbf{X}, t)\mathbf{d} \tag{131}$$

With the shape function defined, the strain can be obtained by computing $\boldsymbol{\varepsilon} = \mathbf{B}\mathbf{d}$ with $\mathbf{B}$ the strain-displacement matrix.

With this the linear elasticity can be solved with

$$\boldsymbol{\sigma} = \mathbf{C} : \boldsymbol{\varepsilon} \tag{132}$$

in which $\mathbf{C}$ is the elasticity tensor.

5.3 Information passage between Finite Element and Peridynamics

5.3.1 From Finite Element to Peridynamics

Since PD is performed over a local domain, its boundary condition is determined based on the finite element interpolation. This approach is also referred to as the "hand-shake" approach. In the multiscale implementation, the information is passed on to the PD region from the finite element through the hand-shake approach and the corresponding displacements of the PD nodes at the interface is generally referred to as $\mathbf{u}^{\mathbf{in}}$. Thus,

$$\mathbf{u}^{\mathbf{in}} = \mathbf{N}\mathbf{d} \tag{133}$$

in which $\mathbf{N}$ is the shape function matrix, and $\mathbf{d}$ is the corresponding nodal degrees of freedom vector.

5.3.2 From Peridynamics to Finite Element

To pass information from the PD domain to the finite element domain, a projection-based approach has been developed based on the prior work on coupled atomistic/continuum simulation [30]. We first define the interpolation from the FEM to PD nodes for the coupled region. Assume FEM nodal values for each element to be $\mathbf{d}_E$, the PD nodes, $\mathbf{q}_E$, is given as

$$\mathbf{q}_E = \mathbf{N}\mathbf{d}_E \tag{134}$$

The matrix $\mathbf{N}$ is consisting of the shape functions for each FEM node such that $\mathbf{N} = \left[N_1, N_2, N_3, N_4\right]$.

It is desirable to take values from the PD nodes and project them onto the FEM nodes. Therefore we need to rework Eq. (134). The projection operator is obtained by minimizing the difference e_E between the peridynamic solution $\mathbf{q}_E$ and the interpolated value $\hat{\mathbf{q}}_E$ in a weighted least-square sense [30]. This error e_E is expressed as

$$e_E = \left(\mathbf{q}_E - \hat{\mathbf{q}}_E\right)^T \mathbf{M}_{PD,E} \left(\mathbf{q}_E - \hat{\mathbf{q}}_E\right) \tag{135}$$

with $\mathbf{M}_{PD,E}$ being a diagonal mass matrix corresponding to the PD nodes within the element E .

Considering the multiscale approximation in (134), the minimization of e yields

$$\hat{\mathbf{N}}\mathbf{d}_E = \hat{\mathbf{N}}\left(\hat{\mathbf{N}}^T\mathbf{M}_{PD,E}\hat{\mathbf{N}}\right)^{-1}\hat{\mathbf{N}}^T\mathbf{M}_{PD,E}\mathbf{q}_E = \mathbf{P}\mathbf{q}_E \tag{136}$$

where $\mathbf{P} = \hat{\mathbf{N}}\left(\hat{\mathbf{N}}^T\mathbf{M}_{PD,E}\hat{\mathbf{N}}\right)^{-1}\hat{\mathbf{N}}^T\mathbf{M}_{PD,E}$ is the projection operator. Equation (136) can be solved further to get

$$\mathbf{d}_E = \left(\hat{\mathbf{N}}^T\mathbf{M}_{PD,E}\hat{\mathbf{N}}\right)^{-1}\hat{\mathbf{N}}^T\mathbf{M}_{PD,E}\mathbf{q}_E \,. \tag{137}$$

The equation given in (137) gives the projection method by which PD values can be projected upon the finite element nodes.

5.4 One-Way Non-Local Matching Boundary Conditions

Based on the above discussions, the steps of the concurrent coupling approach can be summarized as follows:

a. Calculate the PD and FEM forces for the given time step
    i. Solve for NMBC

b. Perform Projection of PD displacement, velocity, and acceleration onto FEM nodes

c. Advance to next time step

Here it is important to note that the projection from PD to FEM does not necessarily need to include the 1-way NMBC region if other parts of the PD domain are coupled to the FEM domain. The projection is the means by which information is fed back to the FEM domain while the NMBC is operating to minimize the wave that is present within the PD domain.

To demonstrate the importance of the interfacial boundary condition, we first consider an example in which NOPD and FEM are coupled but no matching boundary conditions are defined within the PD domain. We denote PD domain as Ω_{PD}, which is situated in the middle of a FEM domain, Ω_{FEM}. The total model size is 1350 by 10. The Ω_{PD}, encompasses the span from 500 to 850 and spans the entire width. Young's Modulus is set at 100, Poisson's ratio is set to be 0.25, and $\rho = 1$ with the nodal spacings of $\Delta X_{PD} = 1$ and $\Delta X_{FEM} = 5$. The wave generated within the PD domain is defined at the locations $675 - 2\delta < Y < 675 + 2\delta$ as

$$v(Y,t) = \frac{\varepsilon_0}{2}\left(\cos\left(\frac{2\left(|t_{\min}| + t\right)\pi}{|t_{\min}|}\right) + 1\right) \quad \text{for } -10 \le t < 0 \tag{138}$$

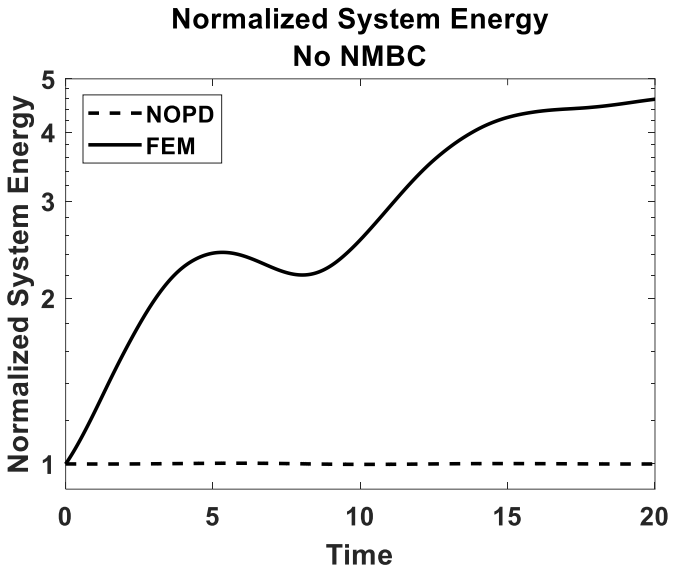

Figure 28: Coupled NOPD/FEM model without interfacial treatment between PD and FEM

Figure 28 provides the history of the system energy for both the NOPD and FEM domains. It can be seen that, without any treatment, the NOPD simulation continues to maintain almost constant energy levels while energy is transmitted into the FEM domain as the simulation progresses. Because of this continual transmission of energy, the FEM domain is seen to have its total system energy increasing to levels that are more than 4.5 times the initial system energy by the end of the simulation, which is not physical. This example demonstrates the importance of the interfacial boundary conditions that provide a seamless connection between the two domains.

5.5 2D Examples

To further highlight the importance, we now look into an example that includes the NMBC proposed in the previous chapter. This unidirectional example consists of a finite element grid with a node spacing of $\Delta X_{FEM} = 5$ that is 360 tall and 10 wide. It can be seen in Figure 29 that there are 25 PD nodes within each finite element. A Peridynamic region is overlaid on the FEM domain

from 90 to 270 with a node spacing of $\Delta X_{PD} = 1$. Young's Modulus is set at 100, Poisson's ratio is set to be 0.25, and $\rho = 1$. The simulation is initially at rest and a wave is created from $180 - 2\delta < Y < 180 + 2\delta$ in the PD domain such that

$$v(Y,t) = \frac{\varepsilon_0}{2}\left(\cos\left(\frac{2\left(|t_{\min}| + t\right)\pi}{|t_{\min}|}\right) + 1\right) \quad \text{for } -10 \le t < 0 \tag{139}$$

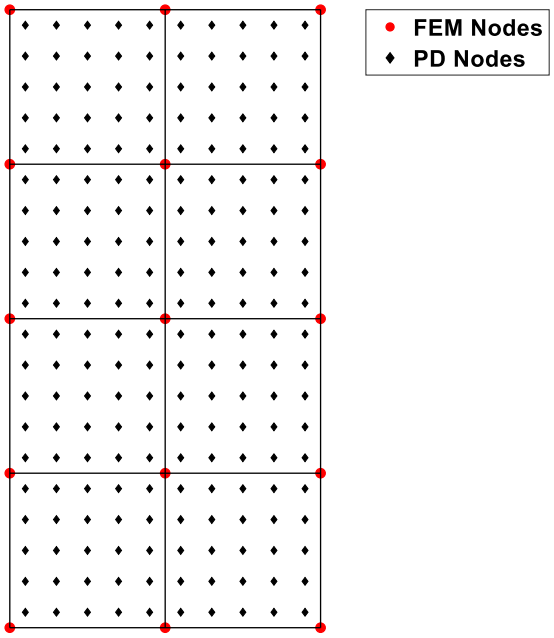

Figure 29: Allocation of PD nodes within the finite elements for the unidirectional simulation

From here, the wave propagates through Ω_{PD} and encounters the NMBC. The projection operation is running in the background to interpolate the PD solutions onto the FEM nodes and as the wave in Ω_{PD} reaches the NMBC the wave is effectively transferred to Ω_{FEM} as the NMBC minimizes any artificial reflection within Ω_{PD}.

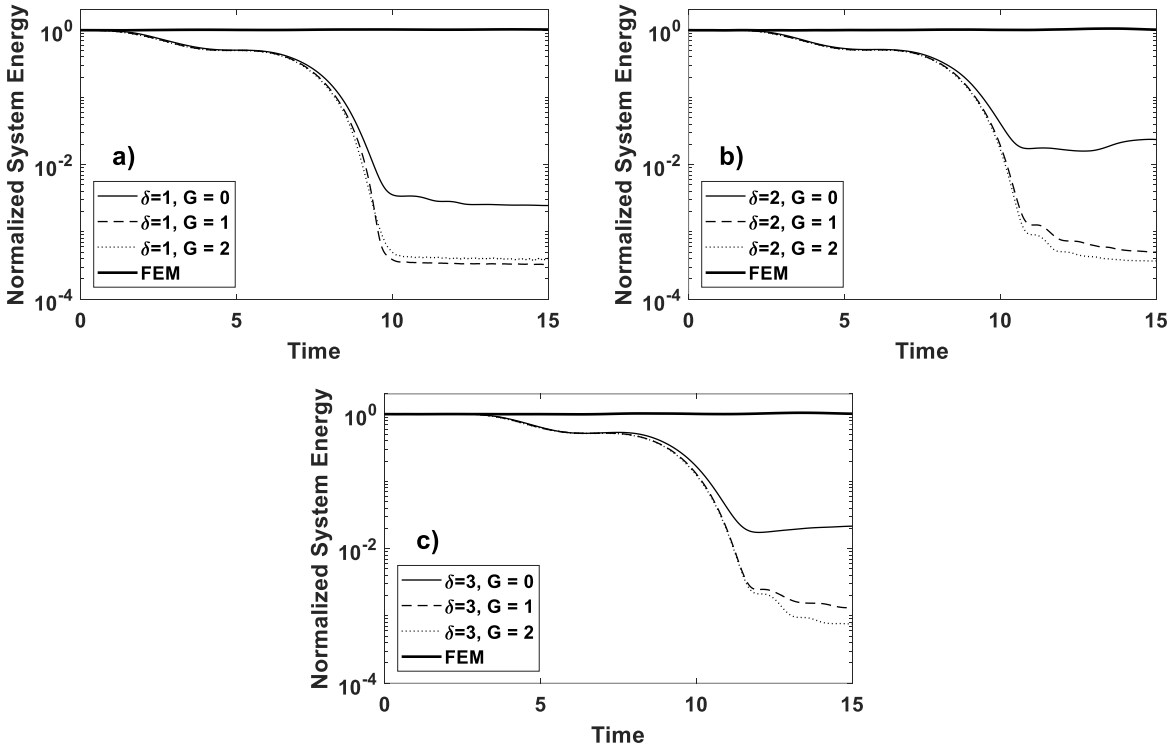

Figure 30: Total system energy of FEM and PD domains within the coupled unidirectional simulations for a) $\delta = 1\Delta X$ **, b)** $\delta = 2\Delta X$ **, and c)** $\delta = 3\Delta X$

As shown in Figure 30 the NMBC performs well in the minimization of total PD energy as the wave approaches and passes through to the FEM domain. Very little energy is left within the PD domain. The stabilization constant can increase the efficiency of the NMBC by reducing the presence of zero energy modes to a certain extent as seen before in Chapter 4.5. The NMBC with the stabilized correspondence material model can perform an order of magnitude better in energy absorption.

In addition to the energy reduction within the PD domain it can also be seen that the energy within the FEM domain remains relatively constant. This reveals that the wave that is generated

within the PD domain is effectively transferred to the FEM domain without diminishing or amplifying the wave as it passes into the FEM domain through the projection.

We further consider the case of a multidirectional wave in the case of 2D. Here a wave originates from a center point and propagates in all directions from that point into the discretized domain as originally discussed in Section 4.6. For this example, an initial displacement is set up with the PD domain. The FEM domain, Ω_{FEM} is 950x1000 nodes in size with the PD domain, Ω_{PD}, is 200x250 nodes large and is overlaid from 375 to 575 in the Y direction and 375 to 625 in the X direction. The constitutive properties are the same as stated in the previous unidirectional example. A new nodal spacing is given as $\Delta X_{FEM} = 10$ and $\Delta X_{PD} = 1$. From Figure 31 it can be seen that there are 100 PD nodes inside each finite element. The initial displacement on the PD domain is given as

$$v(Y, t=0) = \begin{cases} \frac{\varepsilon_0}{2}\left[\sin\left(\frac{\pi r_i}{r_{\max}} + \frac{\pi}{2}\right) + 1\right] & r_i \le r_{\max} \\ 0 & r_i > r_{\max} \end{cases} \tag{140}$$

in which $\varepsilon_0 = 0.1$, $r_i = \sqrt{\left(X_i - \frac{950}{2}\right)^2 + \left(Y_i - \frac{1000}{2}\right)^2}$, $r_{\max} = 78.5$.

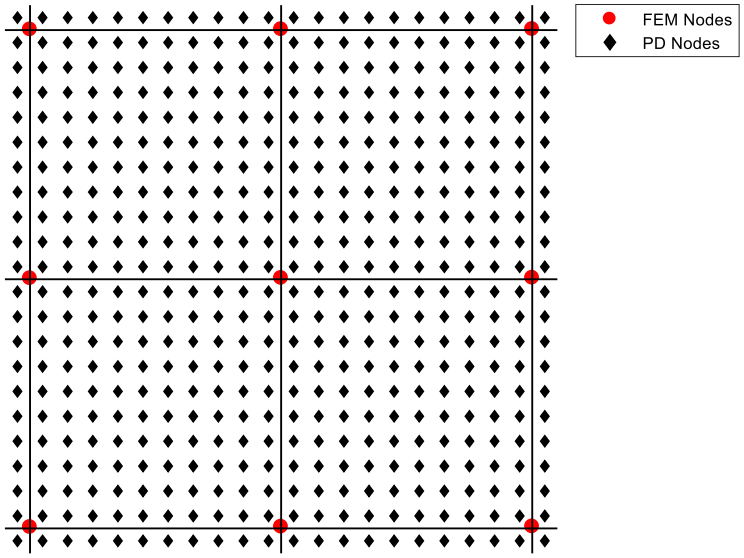

Figure 31: Allocation of PD nodes within the finite elements for the multidirectional wave simulation

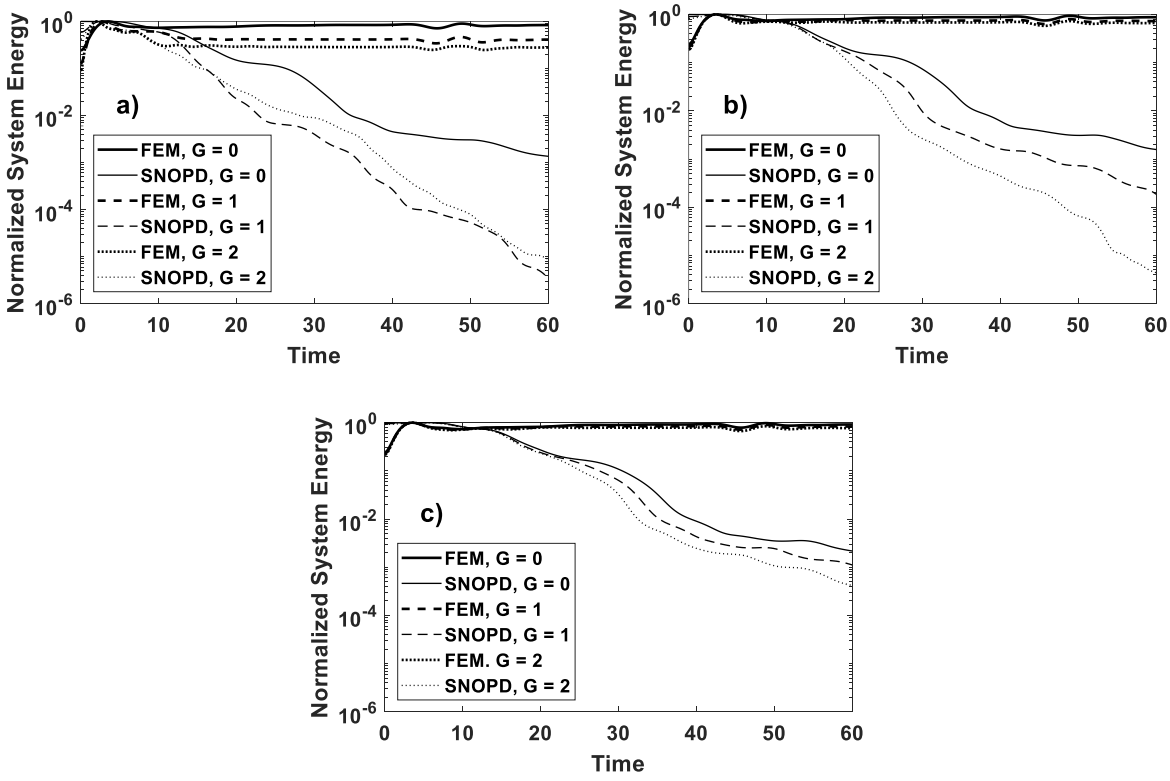

Figure 32: Total system energy of FEM and PD domains within the coupled multidirectional simulations for a) $\delta = 1\Delta X$ **, b)** $\delta = 2\Delta X$ **,c)** $\delta = 3\Delta X$

Figure 32 shows the system energy history for the case of different neighborhood sizes. As can be seen the multidirectional NMBC is also effective in a coupled domain. The final results from the multidirectional example follow the result trend that is given in the unidirectional simulations. With increasing *G* values, it is observed that the NMBC functions more effectively, but with smaller neighborhoods having a visible regression in energy reduction when too high a stabilization value *G* is chosen.

It is also observed that smaller values of G seem to leave the FEM domain with a higher overall energy level than that of the lower G values. This can be attributed to the transfer of the latent energy associated with zero energy modes into the FEM domain via the projection.

5.6 Two-Way Non-Local Matching Boundary Conditions

While the NMBC proposed earlier accomplishes a non-reflective boundary condition for the waves that originate from the PD domain, it is also realized that there is a component of the wave that propagates into the PD domain from the FEM domain through the hand-shake. This motivates the modification of the 1-way NMBC that was proposed earlier into a 2-way information passing scheme as part of the coupling.

This implementation is based on an extension of the work established by Wang, et.al., [2]. We first propose a decomposition of the displacement into incoming and outgoing components:

$$\mathbf{u}_i = \mathbf{u}_i^{\mathrm{In}} + \mathbf{u}_i^{\mathrm{Out}} \tag{141}$$

Recall that the previous definition of the NMBC in (112) was for treating the outgoing waves withihn the PD domain. So we can therefore recast the original NMBC in (112) as

$$\sum_{i=0}^{N} c_i \dot{u}_{i-M}^{\mathbf{Out}} - \sum_{i=0}^{N} b_i u_{i-M}^{\mathbf{Out}} = 0 \tag{142}$$

An NMBC for an incoming wave can be defined in the same manner such that (142) can be manipulated to get

$$\sum_{i=0}^{N} c_i \dot{u}_{i-M}^{\mathbf{Out}} - \sum_{i=0}^{N} b_i u_{i-M}^{\mathbf{Out}} + \left(\sum_{i=0}^{N} c_i \dot{u}_{i-M}^{\mathbf{In}} - \sum_{i=0}^{N} b_i \left(u_{i-M}^{\mathbf{In}} \right) - \sum_{i=0}^{N} c_i \dot{u}_{i-M}^{\mathbf{In}} + \sum_{i=0}^{N} b_i \left(u_{i-M}^{\mathbf{In}} \right) \right) = 0 \tag{143}$$

Equation (143) can then be simplified using (141) to the following boundary equation

$$\dot{u}_{i-M} = \left(\sum_{i=1}^{N} c_i \dot{u}_{i-M} - \sum_{i=0}^{N} b_i u_{i-M} \right) - \left(\sum_{i=0}^{N} c_i \dot{u}_{i-M}^{\mathbf{In}} - \sum_{i=0}^{N} b_i u_{i-M}^{\mathbf{In}} \right) \quad \text{for } M = 0,...,2n-2,2n-1 \tag{144}$$

Equation (144) is still able to account for any incoming wave that may be transferred from the surrounding domain while using the same NMBC coefficients as defined CHAPTER 4. The 2D version can be expressed similarly as

$$\dot{\mathbf{u}}_{i-M,j} = \left(\sum_{i=1}^{N} \mathbf{C}_i^{(M)} \dot{\mathbf{u}}_{i-M,j} - \sum_{i=0}^{N} \mathbf{B}_i^{(M)} \mathbf{u}_{i-M,j} \right) - \left(\sum_{i=0}^{N} \mathbf{C}_i^{(M)} \dot{\mathbf{u}}_{i-M,j}^{\mathbf{In}} - \sum_{i=0}^{N} \mathbf{B}_i^{(M)} \mathbf{u}_{i-M,j}^{\mathbf{In}} \right) \quad \text{for } M = 0,...,2n-2,2n-1 \tag{145}$$

The constants of $\mathbf{C}_i^{(M)}$ and $\mathbf{B}_i^{(M)}$ are the same as defined in (123).

In the case of the 2-Way NMBC, the process by which FEM and PD are coupled needs to be more delicately handled. Specifically, this is because the input side of the 2-way NMBC, which uses information from the finite element domain, has the potential to cause a feedback loop. The NMBC region cannot be included in the projection of information from Ω_{PD} to Ω_{FEM}. For the 2-way NMBC, the information from the Ω_{FEM} that overlaps the NMBC domain has to be interpolated onto the PD nodes. This can be done through any interpolation methodology, but is

done here with a shape function interpolation that is identical to the method used in the finite element domain. The configuration of coupling the 2-way NMBC is shown in Figure 33. It can be seen that the 2-Way NMBC isn't defined over the entire boundary region, but rather, is only defined on nodes that border Ω_{PD} and only as many nodes as are in a single neighborhood. This follows a standard practice in PD in that displacement constraints are defined across an entire neighborhood [20]. Defining the 2-way NMBC larger than a single neighborhood can result in additional reflection at the interface from a wave that is passing from the FEM domain into the PD domain. The total size of the NMBC domain, including the 2-way NMBC nodes, should be no less than 2 times the neighborhood as previously discussed.

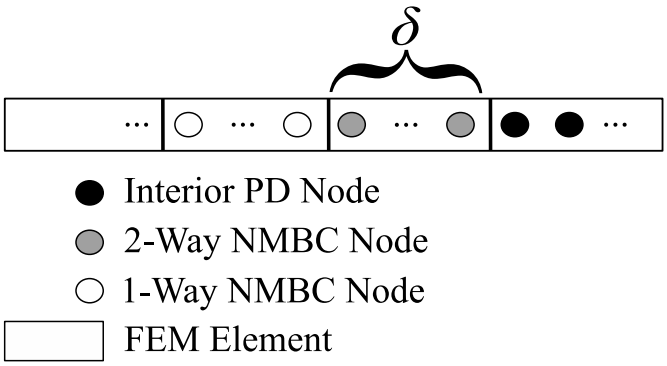

Figure 33: Depiction of the 2-Way NMBC coupling

In order to pass information from the FEM to the PD domain through the 2-Way NMBC, the FEM displacement and velocity are interpolated from Ω_{FEM} to a nodal spacing equal to that of Ω_{PD}. The interpolated FEM displacement and velocity values are stored in $\dot{\mathbf{u}}^{\mathbf{In}}(\mathbf{X},t)$ and $\mathbf{u}^{\mathbf{In}}(\mathbf{X},t)$ and are used in the 2-Way NMBC defined in (144). Displacement, velocity, and acceleration are

projected from Ω_{PD} onto overlapping regions of Ω_{FEM}. Below is the algorithm used for this process.

a) Calculate the PD forces for the given time step

b) Calculate the FEM forces for the given time step

c) Calculate the projection and interpolation of data

   i) Project PD displacements, velocities, and accelerations onto the overlapping FEM domain

   ii) Interpolate FEM values to PD spacing

d) Calculate the NMBC boundary equations using current PD values and current interpolated FEM $\dot{\mathbf{u}}^{In}$ and $\mathbf{u}^{In}$ values.

e) Advance to next time step

With this process, the FEM nodal placement in the PD domain can be determined. Since the NMBC domain is not used in the projection, the problem of a feedback loop is eliminated. With this process we can perform a coupled 2D simulation example with the 2-way NMBC. In this example we set up a configuration that is exactly the same as the one given in Section 4.5 for the unidirectional example but with a time that has been extended to 90 to allow for the wave to pass through the 2-way NMBC multiple times in order to assess the effectiveness of the 2-way NMBC. The figures below show that the 2-Way NMBC functions as expected in that it allows for information to pass out of and into the NMBC domain. We can see the wave within the PD domain

when the normalized energy is at 10^{0}. As the wave leaves the PD domain the energy levels decrease showing the effectiveness of the 2-Way NMBC.

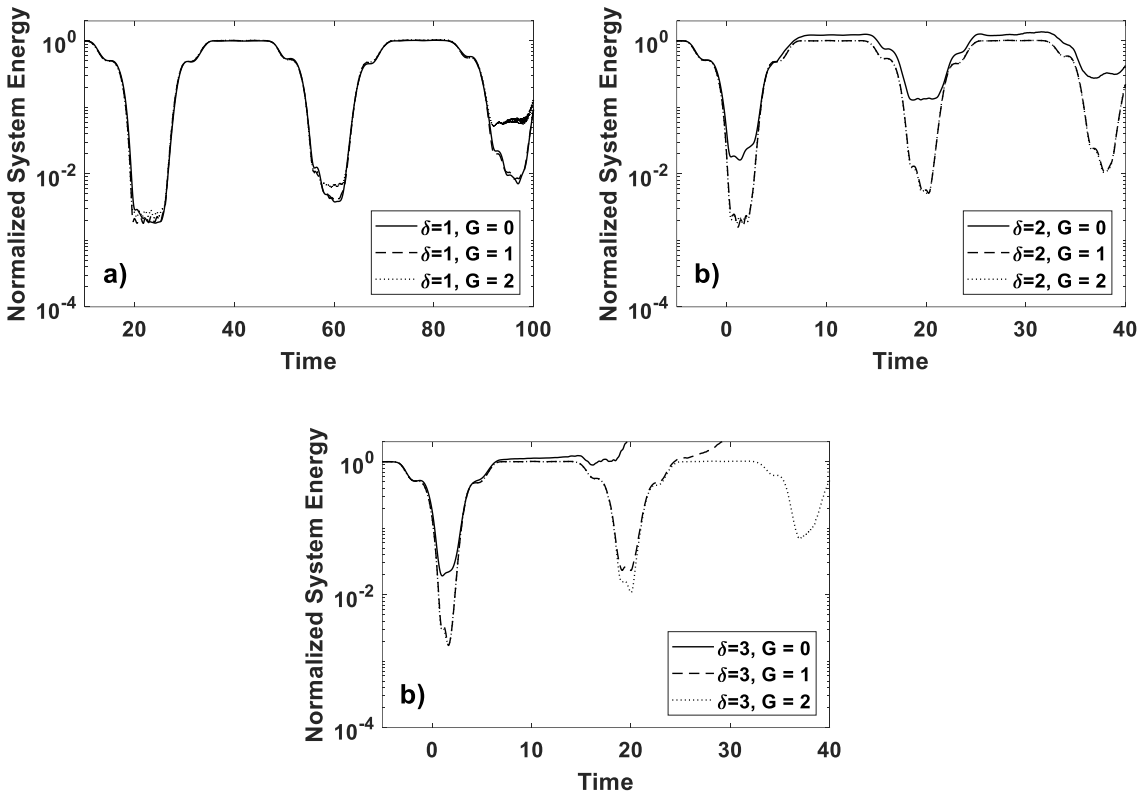

Figure 34: Total system energy for 2-Way NMBC of PD domains within the coupled unidirectional simulations for a) $\delta = 1\Delta X$, b) $\delta = 2\Delta X$,c) $\delta = 3\Delta X$

Although, it is seen from the plots in Figure 34 that the addition of the 2-way ability doesn't come without consequence. While the initial absorption out of the PD domain is still quite effective, subsequent passing of the information brings less effective energy absorption with each pass. This is seen for all of the PD neighborhood sizes in Figure 34 and can be attributed to successive latent energy that is not absorbed by the NMBC remaining in the PD domain. It should also be noted that increased neighborhood sizes bring an additional instability at low stabilization levels. In Figure 34-b it can be seen that the energy in the simulation for $G = 0$ increases through time. This effect

is much more pronounced in Figure 34-c for a neighborhood of $\delta = 3$ where the normalized energy levels increase without bound beyond the initial level. Again, there is a range of G values for which the simulation is stable as was the case for the 1-way NMBC.

5.7 Peridynamic Fracture Initiation within a Coupled PD/FEM Simulation

As a meshfree method, PD has unique advantage in capturing fracture since it does not require tedious remeshing processes as required by most of the FEM approaches. With the demonstration of a successful implementation of a 2-Way NMBC a coupled PD/FEM simulation can be constructed to simulate the initiation and propagation processes of fracture.

Here a simulation configuration similar to the one found in Section 4.5 is constructed. But in this case we have changed the domain size to 50x90 in the x and y coordinates respectively. Two simulations are run and directly compared to the other. One is a simulation whose domain is entirely NOPD with a stabilized correspondence material. The other is a coupled PD/FEM simulation with the PD domain in the center and finite element on the top and bottom. In the coupled domain the PD domain is from $Y = [15, 75]$ across the width, and two separate FEM domains are from $Y = [0, 30]$ and $Y = [60, 90]$ across the width. The domain in the center is only populated by PD in order to allow fracture propagation without complications from a background finite element mesh. The discretization of each domain is $\Delta X_{FEM} = 5$ and $\Delta X_{PD} = 1$ and the neighborhood for the PD domain in both simulations are set to be $\delta = 2\Delta X$. Boundary conditions are placed on the finite element domains such that $\dot{v}(Y = 0) = 0$ and $\dot{v}(Y = 90) = 0.05$. The value of the influence function is set to zero once the stretch, shown in equation (5), reaches a value of 0.05 or greater thus causing a crack of occur. A pre-crack is incorporated into the PD domain at

$Y = 45,\ X = [0,5]$. The resulting simulations is as shown in Figure 35. The number of bonds that are broken through time are tracked and then compared to each other in Figure 36.

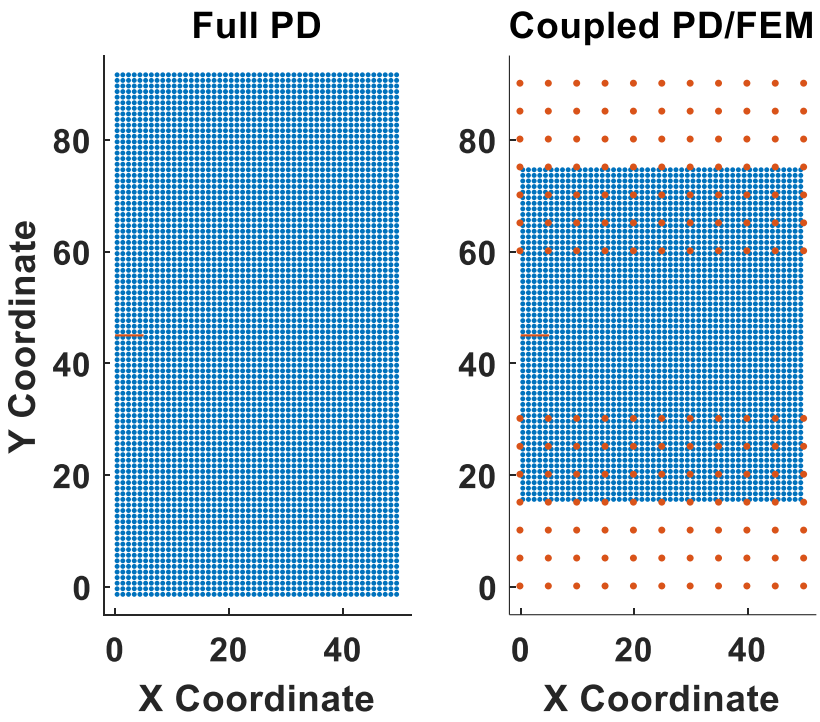

Figure 35: Dual simulations showing the initial setup between a full PD domain and a coupled PD/FEM domain with a pre-crack.

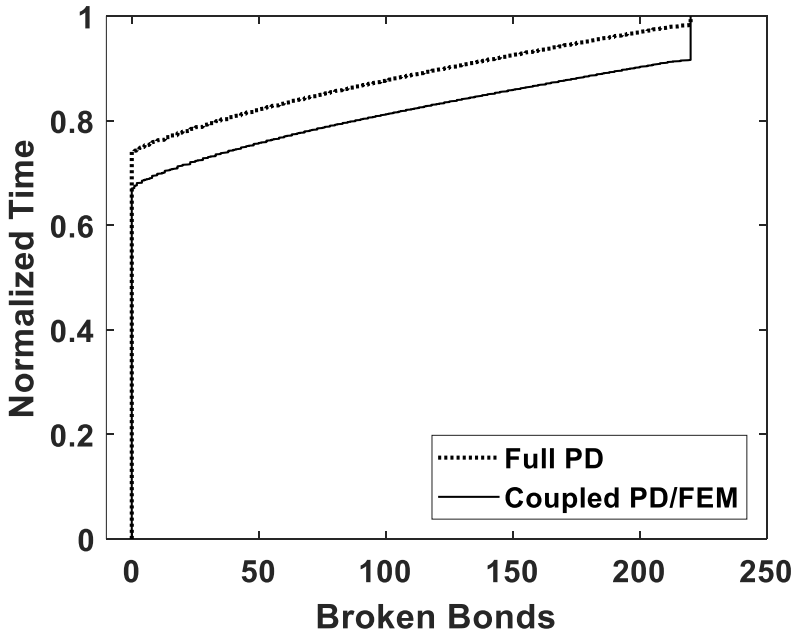

Figure 36: The number of bonds broken in the full PD simulation and the coupled PD/FEM simulation compared against normalized simulation time.

Here it can be seen that although the bonds begin to break at different times, the overall trend of bonds breaking within the simulation remain very similar. This result is not surprising as PD is a much more complex model and involves multiple connections to each node through multiple bonds. The coarser FEM domain is saturated much more quickly from the boundary condition and thus the fracture occurs sooner.

CHAPTER 6

CONCLUSION

In summary, the main contributions of this research are the establishment of the nonlocal matching boundary conditions for the three predominant formulations of peridynamics and incorporation of the MBC into a concurrent multiscale simulation scheme. In the different versions of MBCs for different PD formulations, it was reported that BBPD allows an implementation that is very similar to previous MBC implementations, however the implementation for OPD and NOPD is different and thus labeled NMBC. The required implementation for NMBC, for optimal performance, is that the number of boundary nodes be twice that of the radius of the selected horizon. The introduction of the 2D NOPD NMBC is shown to be effective as well using the NMBC approach.

The rate at which the reflection coefficient increases is subject to the variant of peridynamics utilized and the size of the neighborhood. NOPD is the most different from the others in that it is highly dispersive and can express phase velocities near 0 as the wave number increases from 0. Compounding this issue are that the long wave NMBC used in NOPD are shown to be less effective as the wave number increases from 0. This phenomenon is attributed to the presence of zero energy modes that are perturbed during the creation of the wave. Currently, the presence of the zero energy modes is an intrinsic property of the NOPD correspondence material and cannot be avoided without the use of artificial penalty methods to restrict zero energy mode activation. These zero energy modes can be mitigated with the introduction of the stabilized correspondence material for NOPD. Though, the introduction of SNOPD doesn't remedy the troubles of the zero

energy modes on NMBC completely. Particular selection of G values allow for the higher order NMBC to be performed without instabilities. Reflection coefficients indicate that the SNOPD can increase the energy absorption of the NMBC from the standard NOPD.

After establishing the feasibility of the NMBC, concurrently coupled FEM/PD simulation approach are established using a projection scheme to interpolate PD values onto the overlapping FEM nodes. This allows for waves to be created within the PD domain and propagate into the FEM domain while minimizing waves that would be reflected at the interface boundary. A 2-way NMBC is also evaluated within the 2D coupled FEM/PD simulation and is shown to be effective in transferring information through the FEM/PD interface. Though, numerous transfers between the 2-way interfaces can result in decreased performance of the wave absorption at the NMBC. Overall the NMBC approach has been shown to work effectively in the proposed multiscale simulation approach. This 2-way NMBC is then utilized to showcase the fracture capability of the coupled PD/FEM simulation and is then compared to the results of a full PD simulation. In this comparison it is seen that the results closely resemble each other in the pattern of bond breakage, though the initiation times for that respective fracture initiation occur at different times.

REFERENCES

[1] W. K. Liu, D. Qian, S. Gonella, S. Li, W. Chen, and S. Chirputkar, “Multiscale methods for mechanical science of complex materials: Bridging from quantum to stochastic multiresolution continuum,” *Int. J. Numer. Methods Eng.*, vol. 83, no. 8–9, pp. 1039–1080, Aug. 2010.

[2] L. Wang, Y. Chen, J. Xu, and J. Wang, “Transmitting boundary conditions for 1D peridynamics,” *Int. J. Numer. Methods Eng.*, 2016.

[3] S. A. Silling, “Reformulation of elasticity theory for discontinuities and long-range forces,” *J. Mech. Phys. Solids*, vol. 48, no. 1, pp. 175–209, 2000.

[4] S. A. Silling and E. Askari, “A meshfree method based on the peridynamic model of solid mechanics,” *Comput. Struct.*, vol. 83, no. 17–18, pp. 1526–1535, 2005.

[5] S. A. Silling, M. Epton, O. Weckner, J. Xu, and E. Askari, “Peridynamic states and constitutive modeling,” *J. Elast.*, vol. 88, no. 2, pp. 151–184, 2007.

[6] T. L. Warren, S. A. Silling, A. Askari, O. Weckner, M. A. Epton, and J. Xu, “A non-ordinary state-based peridynamic method to model solid material deformation and fracture,” *Int. J. Solids Struct.*, vol. 46, no. 5, pp. 1186–1195, 2009.

[7] P. Seleson, S. Beneddine, and S. Prudhomme, “A force-based coupling scheme for peridynamics and classical elasticity,” *Comput. Mater. Sci.*, vol. 66, pp. 34–49, 2013.

[8] P. Seleson, Y. D. Ha, and S. Beneddine, “Concurrent coupling of bond-based peridynamics and the Navier equation of classical elasticity by blending,” *J. Multiscale Comput. Eng.*, vol. 13, no. 2, pp. 91–113, 2015.

[9] F. Bobaru, J. T. Foster, P. H. Geubelle, and S. A. Silling, *Handbook of Peridynamic Modeling*. Chapman & Hall, 2014.

[10] P. T. Bauman, H. Ben Dhia, N. Elkhodja, J. T. Oden, and S. Prudhomme, “On the application of the Arlequin method to the coupling of particle and continuum models,” *Comput. Mech.*, vol. 42, no. 4, pp. 511–530, Sep. 2008.

[11] T. Belytschko and S. P. Xiao, “Coupling Methods for Continuum Model with Molecular Model,” *Int. J. Multiscale Comput. Eng.*, vol. 1, no. 1, p. 12, 2003.

[12] H. Ben Dhia, “Further Insights by Theoretical Investigations of the Multiscale Arlequin Method,” *Int. J. Multiscale Comput. Eng.*, vol. 6, no. 3, pp. 215–232, 2008.

[13] H. Ben Dhia and G. Rateau, “The Arlequin method as a flexible engineering design tool,”

Int. J. Numer. Methods Eng., vol. 62, no. 11, pp. 1442–1462, Mar. 2005.

[14] X. Chen and M. Gunzburger, "Continuous and discontinuous finite element methods for a peridynamics model of mechanics," *Comput. Methods Appl. Mech. Eng.*, vol. 200, no. 9, pp. 1237–1250, 2011.

[15] R. W. Macek and S. A. Silling, "Peridynamics via finite element analysis," *Finite Elem. Anal. Des.*, vol. 43, no. 15, pp. 1169–1178, 2007.

[16] R. A. Wildman and G. A. Gazonas, "A perfectly matched layer for peridynamics in two dimensions," *J. Mech. Mater. Struct.*, vol. 7, no. 8–9, pp. 765–781, Dec. 2012.

[17] R. A. Wildman and G. A. Gazonas, "A perfectly matched layer for peridynamics in one dimension," Adelphi, MD, 2011.

[18] Y. Mikata, "Analytical solutions of peristatic and peridynamic problems for a 1D infinite rod," *Int. J. Solids Struct.*, vol. 49, no. 21, pp. 2887–2897, 2012.

[19] Z. P. Bažant, W. Luo, V. T. Chau, and M. A. Bessa, "Wave Dispersion and Basic Concepts of Peridynamics Compared to Classical Nonlocal Damage Models," *J. Appl. Mech.*, vol. 83, no. 11, p. 111004, 2016.

[20] E. Madenci and E. Oterkus, *Peridynamic theory and its applications*, vol. 9781461484. 2014.

[21] W. Gerstle, *Introduction to practical peridynamics : computational solid mechanics without stress and strain*. World Scientific Publishing Co. Pte. Ltd., 2016.

[22] S. A. Silling, "Stability of Peridynamic Correspondence Material Models and Their Particle Discretizations," *Comput. Methods Appl. Mech. Engrg.*, 2017.

[23] M. A. Bessa, J. T. Foster, T. Belytschko, and W. K. Liu, "A meshfree unification: Reproducing kernel peridynamics," *Comput. Mech.*, vol. 53, no. 6, pp. 1251–1264, 2014.

[24] F. Bobaru, M. Yang, L. F. Alves, S. A. Silling, E. Askari, and J. Xu, "Convergence, adaptive refinement, and scaling in 1D peridynamics," *Int. J. Numer. Methods Eng.*, vol. 77, no. 6, pp. 852–877, 2009.

[25] S. Tang, "A finite difference approach with velocity interfacial conditions for multiscale computations of crystalline solids," *J. Comput. Phys.*, vol. 227, no. 8, pp. 4038–4062, 2008.

[26] X. Wang and S. Tang, "Matching boundary conditions for lattice dynamics," *Int. J. Numer. Methods Eng.*, vol. 93, no. 12, pp. 1255–1285, Mar. 2013.

[27] X. Wang and S. Tang, "Matching boundary conditions for diatomic chains," *Comput.*

Mech., vol. 46, no. 6, pp. 813–826, 2010.

[28] M. S. Breitenfeld, P. H. Geubelle, O. Weckner, and S. A. Silling, "Non-ordinary state-based peridynamic analysis of stationary crack problems," *Comput. Methods Appl. Mech. Eng.*, vol. 272, pp. 233–250, 2014.

[29] R. D. Cook, *Concepts and Applications of Finite Element Analysis*, Fourth Edi. Hoboken NJ, 1974.

[30] S. U. Chirputkar and D. Qian, "Coupled atomistic/continuum simulation based on extended space-time finite element method," *C. - Comput. Model. Eng. Sci.*, vol. 24, no. 2–3, pp. 185–202, 2008.

[31] C. T. Wu and B. Ren, "A stabilized non-ordinary state-based peridynamics for the nonlocal ductile material failure analysis in metal machining process," *Comput. Methods Appl. Mech. Eng.*, vol. 291, pp. 197–215, 2015.

[32] S. A. Silling, "Solitary waves in a peridynamic elastic solid," *J. Mech. Phys. Solids*, vol. 96, pp. 121–132, 2016.

[33] J. T. Foster, S. A. Silling, and W. W. Chen, "Viscoplasticity using peridynamics," *Int. J. Numer. Methods Eng.*, vol. 81, no. 10, pp. 1242–1258, 2010.

[34] S. A. Silling, "Linearized theory of peridynamic states," *J. Elast.*, vol. 99, no. 1, pp. 85–111, 2010.

[35] R. B. Lehoucq and S. A. Silling, "Force flux and the peridynamic stress tensor," *J. Mech. Phys. Solids*, vol. 56, no. 4, pp. 1566–1577, 2008.

[36] M. Sadd, *Elasticity: theory, applications, and numerics*. 2009.

[37] T. Belytschko, W. Liu, and B. Moran, *Nonlinear finite elements for continua and structures. 2000*, vol. 16. 2000.

[38] D. J. Littlewood, "Simulation of Dynamic Fracture Using Peridynamics, Finite Element Modeling, and Contact," *ASME 2010 Int. Mech. Eng. Congr. Expo.*, no. June, pp. 1–9, 2010.

[39] E. Askari, F. Bobaru, R. B. Lehoucq, M. L. Parks, S. A. Silling, and O. Weckner, "Peridynamics for multiscale materials modeling," *J. Phys. Conf. Ser.*, vol. 125, 2008.

[40] S. A. Silling, D. J. Littlewood, and P. D. Seleson, "Variable Horizon in a Peridynamic Medium," *Sandia Rep.*, no. October, 2014.

[41] M. L. Parks, "Computational Peridynamics," *Mini-workshopMathematical Anal. Peridynamics*, 2011.

[42] C. T. Wu, “Kinematic constraints in the state-based peridynamics with mixed local/nonlocal gradient approximations,” *Comput. Mech.*, vol. 54, no. 5, pp. 1255–1267, 2014.

[43] W. Liu, “Discretized bond-based peridynamics for solid mechanics,” *ProQuest Diss. Theses*, p. 214, 2012.

[44] J. A. Mitchell, “A Nonlocal , Ordinary , State-Based Plasticity Model for Peridynamics,” *Sandia Rep.*, no. May, pp. 1–34, 2011.

[45] S. and R. L. Silling, “Atoms and Peridynamic Continua Peridynamics background : Alternative to traditional fracture mechanics,” pp. 1–34, 2007.

[46] O. Weckner and R. Abeyaratne, “The effect of long-range forces on the dynamics of a bar,” *J. Mech. Phys. Solids*, vol. 53, no. 3, pp. 705–728, 2005.

[47] R. Becker and R. J. Lucas, “An Assessment of Peridynamics for Pre and Post Failure Deformation,” 2011.

[48] S. A. Silling and R. B. Lehoucq, “Convergence of peridynamics to classical elasticity theory,” *J. Elast.*, vol. 93, no. 1, pp. 13–37, 2008.

[49] S. Li, X. Liu, A. Agrawal, and A. C. To, “Perfectly matched multiscale simulations for discrete lattice systems: Extension to multiple dimensions,” *Phys. Rev. B - Condens. Matter Mater. Phys.*, vol. 74, no. 4, p. 45418, Jul. 2006.

[50] P. Seleson and M. Parks, “On the Role of the Influence Function in the Peridynamic Theory,” *Int. J. Multiscale Comput. Eng.*, vol. 9, no. 6, pp. 689–706, 2011.

[51] L. Brillouin, *Wave propagation in periodic structures; electric filters and crystal lattices*. 1946.

[52] C. Nicely, S. Tang, and D. Qian, "Nonlocal Matching Boundary Conditions for Non-Ordinary Peridynamics with Correspondence Material Model," *Computer Methods in Applied Mechanics and Engineering,* Manuscript submitted for publication, 2018.

[53] C.Nicely and D. Qian, "Projection Coupling of Non-Ordinary Peridynamics with Correspondence Material Model and Finite Element Method," Manuscript in Preparation, 2018

BIOGRAPHICAL SKETCH

Clint Nicely earned his Bachelor of Arts at The College of Wooster in Wooster, Ohio in 2005 with a concentration in Mathematics. He continued on to earn his Master's Degree at The University of Akron in Akron, Ohio with a concentration in Mechanical Engineering. At The University of Akron he focused his Master's Thesis on an analytical model that could be used to investigate multi-walled carbon nanotubes. After graduating in 2008, he moved to Baltimore, Maryland to begin work at the Aberdeen Proving Grounds as a contractor for the Army Research Laboratories, performing research on high velocity kinetic impacts. In 2012, Clint relocated to Dallas, Texas to begin work for Raytheon Space and Airborne Systems as a finite element structural analyst. While at Raytheon, he enrolled in the Advanced Study Program which allowed him to begin study at The University of Texas at Dallas to earn his Ph.D. in Mechanical Engineering which began in 2014. During his studies at UTD, he has presented his work at the United States National Congress on Computational Mechanics (USNCCM) in Montreal, Quebec in 2017 and is preparing a follow up presentation at the sister conference, the World Congress on Computational Mechanics in New York City, New York in 2018.

CURRICULUM VITAE

Clint Nicely

Education

PhD Mechanical Engineering, 2018, The University of Texas at Dallas, Dallas, TX

MS Mechanical Engineering, 2008, The University of Akron, Akron, Ohio

BA Mathematics, 2005, The College of Wooster, Wooster, Ohio

Experience

2008-2012 Senior Scientist, Dynamic Science Inc., Aberdeen, MD

2012-Present Structural Analyst, Raytheon Space and Airborne Systems, Dallas, TX

Publications

S. Graham Kelly and Clint Nicely, “Free Vibrations of a Series of Beams Connected by Viscoelastic Layers,” Advances in Acoustics and Vibration, vol. 2015, Article ID 976841, 8 pages, 2015. doi:10.1155/2015/976841

C. Nicely, S. Tang, and D. Qian, "Nonlocal Matching Boundary Conditions for Non-Ordinary Peridynamics with Correspondence Material Model," *Computer Methods in Applied Mechanics and Engineering,* accepted, April 2018.

C.Nicely and D. Qian, "Projection Coupling of Non-Ordinary Peridynamics with Correspondence Material Model and Finite Element Method," Manuscript in Preparation, 2018

Conference Presentations

Clint Nicely, “Aluminum Alloy Material Models in the ALEGRA Hyrdocode” High Performance Users Group Conference, June 2011

Clint Nicely and Dong Qian, “Matching Boundary Conditions for State-Based and Bond-Based Peridynamics” United States National Congress on Computational Mechanics, June 2017

Clint Nicely, Dong Qian, and Rui Zhang, “Matching Boundary Conditions for Non Ordinary Peridynamics” International Mechanical Engineering Congress & Exposition, November 2017